

**Characterization of Au+Au Collisions at $\sqrt{s_{NN}} = 200$ GeV from STAR:
from Meson Production in Ultra-Peripheral Collisions to High- p_T
Azimuthal Correlations in Central Collisions**

By

Brooke A. Haag
B.A. (Sonoma State University) 2001
M.S. (University of California at Davis) 2003

DISSERTATION

Submitted in partial satisfaction of the requirements for the degree of

Doctor of Philosophy

in

Physics

in the

OFFICE OF GRADUATE STUDIES

of the

UNIVERSITY OF CALIFORNIA
DAVIS

Approved:

Committee in Charge

2009

Abstract

Characterization of Au+Au Collisions at $\sqrt{s_{NN}} = 200$ GeV from STAR: from Meson Production in Ultra-Peripheral Collisions to High- p_T Azimuthal Correlations in Central Collisions

by

Brooke A. Haag

Physicists at the Relativistic Heavy Ion Collider have concluded that in high-energy heavy-ion collisions a strongly coupled medium consisting of deconfined quarks and gluons has been observed [1]. In these collisions, the incoming partons undergo hard scatterings losing energy as they traverse the medium created and fragmenting into back-to-back hadron jets. A main analysis technique used to probe this dijet production has been di-hadron correlations. Measurements have indicated that there is a strong suppression of the away-side high- p_T particle yield providing direct evidence that high- p_T partons lose energy as they traverse the strongly interacting medium. However, since the momentum of the trigger particle is not necessarily a good measure of the jet energy, di-hadron correlations have limited sensitivity to the shape of the fragmentation function. A suppression is seen, but the details are unclear. In this thesis, the possibility to better constrain the initial parton energy by using clusters of multiple high- p_T hadrons in a narrow cone as the ‘trigger particle’ in the azimuthal correlation analysis is presented. Results from this analysis of multi-hadron triggered

correlated yields in Au+Au collisions at $\sqrt{s_{NN}} = 200$ GeV from STAR are presented. The yields presented are comparable to di-hadron correlation yields possibly indicating that both methods select a similar underlying jet energy. Finally, comparisons are made to analogous measurements in PYTHIA p+p simulations with the same trend observed.

Another measurement presented in this thesis is the quantum mechanical interference effect observed in ultra-peripheral collisions (UPCs) where the electromagnetic interactions between ions dominate as opposed to the strong interactions probed in the aforementioned hard scattering processes. This thesis presents a measurement of destructive interference in the cross section of photoproduced ρ^0 mesons in Au+Au UPC collisions at $\sqrt{s_{NN}} = 200$ GeV from STAR. In an ultra-peripheral collision a ρ^0 meson is produced when a photon from one nucleus fluctuates to a $q\bar{q}$ pair and scatters off the second nucleus. Since the photon is as likely to come from one nucleus as the other, the two processes interfere quantum mechanically, and destructive interference in the cross section is observed for low p_T ρ^0 mesons.

For my mother,
who always believed in me
more than I believed in myself.

Contents

List of Figures	vi
List of Tables	xvii
1 Introduction	1
1.1 Heavy-ion Collisions: Mapping the QCD Phase Diagram	4
2 Experimental Facilities	26
2.1 The Relativistic Heavy Ion Collider	29
2.2 The STAR Detector	35
2.3 Trigger Detectors	51
3 Interference in ρ^0 Photoproduction	56
3.1 Introduction	56
3.2 Experimental Measurement	64
4 Multi-hadron Triggered Correlations	80
4.1 Introduction	80
4.2 Analysis Technique	87
5 Conclusion	105
5.1 ρ^0 Photoproduction	105
5.2 Multi-Hadron Triggered Study	106
A Glauber Model	107
B Topology Trigger MC Simulations	109
C Monte Carlo / Data comparisons	116
D Multi-Hadron $\Delta\phi$ Distributions	127
Bibliography	140

List of Figures

1.1	The radial density profile of neutron stars reflecting the hadronic EOS and the general QCD phase diagram [2].	3
1.2	A contemporary view of the QCD phase diagram - a semi-quantitative sketch [3].	4
1.3	Two scenarios for the evolution of the system created in a relativistic nucleus-nucleus collision. The left-hand side shows the evolution for the case of no QGP being created, while the right-hand side shows the expected evolution of the system including QGP formation. Lines of constant temperature indicate hadronization (T_c), chemical freeze-out (T_{ch}), and kinetic freeze-out (T_{fo}) [4].	5
1.4	Two views of a heavy ion collision at a center-of-mass energy of 200 GeV. On the left side of the figure, a side perspective is shown. The ions look like pancakes Lorentz contracted along the direction of travel with an aspect ratio of 100:1 (height to thickness). On the right side of the figure, a perspective along the beam axis is shown with the left nucleus traveling out of the page and the right nucleus traveling into the page. The collision is a peripheral collision with the overlap region indicated in white.	8
1.5	Multiplicity distributions of Au+Au collisions at three energies: 19.6 (dots), 130 (open circles), and 200 GeV (solid line). Dashed vertical lines indicate the centrality cuts used in the 19.6 GeV spectra analysis [6].	18
1.6	Diagram showing the definition of reaction plane as the plane defined by the impact parameter between the two nuclei and the beam axis.	19
1.7	Vector diagram indicating for a particle of momentum \vec{p} with respect to the beam axis defined as the z-axis, the definition of transverse momentum, p_T , and the angle θ	19

1.8	Pseudorapidity density of charged particles emitted in Au+Au collisions at three different values of the nucleon-nucleon center-of-mass energy [9]. Data are shown for a range of centralities, labeled by the fraction of total inelastic cross section in each bin, with smaller numbers being more central. Grey bands shown for selected centrality bins indicate the typical systematic uncertainties (90% C.L.). Statistical errors are smaller than the symbols [11].	20
1.9	The Bjorken energy density, $\epsilon_{Bj} \cdot \tau$, deduced from PHENIX data at three RHIC energies [10].	21
1.10	Ratios of p_T -integrated midrapidity yields for different hadron species measured in STAR for central Au+Au collisions at $\sqrt{s_{NN}} = 200$ GeV. The horizontal bars represent statistical model fits to the measure yield ratios for stable and long-lived hadrons. The fit parameters are $T_{ch} = 163 \pm 4$ MeV, $\mu_B = 24 \pm 4$ MeV, $\gamma_s = 0.99 \pm 0.07$ [12]. The variation of γ_s with centrality is shown in the inset, including the value (leftmost point) from fits to yield ratios measured by STAR for 200 GeV p+p collisions [1].	22
1.11	Hadron spectra measured by the STAR collaboration [20, 21, 22]. The spectra are from Au+Au collisions at $\sqrt{s_{NN}} = 200$ GeV measured at mid-rapidity. In each panel centrality increases from bottom to top. For K^* the lowest points come from p+p collisions at 200 GeV. Dashed curves in (a), (b), and (e) are from minimum-bias collisions [1].	23
1.12	χ^2 contours resulting from simultaneous blast-wave fits to several species of produced hadrons, π , K , and p as well as for the most central data for multi strange hadrons ϕ and Ω [23]. The top axis shows the nine centrality bins applied to the data from Au+Au collisions at $\sqrt{s_{NN}} = 200$ GeV [12]. The bins range from 70-80% to top 5%, left to right. Results from p+p collisions are included as well. The dashed and solid lines are 1σ and 2σ contours, respectively.	24
1.13	$R_{AB}(p_T)$ from Eq. 1.4 for minimum bias and central d+Au collisions, and central Au+Au collisions [18]. The minimum bias d+Au data are displaced 100 MeV/c to the right for clarity. The bands show the normalization uncertainties, which are highly correlated point-to-point and between the two d+Au distributions [63].	25
2.1	The PHENIX event display.	27
2.2	The PHOBOS event display.	28
2.3	The BRAHMS detector.	29
2.4	Facilities of the RHIC complex. Considering the RHIC rings as the face of a clock, the STAR experiment is located at the six o'clock position.	31
2.5	The ZDC layout as shown in [10].	34
2.6	An end view of the STAR detector [33]. Figures are drawn in the picture for scale. The STAR detector is 1200 tons and the size of a house. The magnet and various components are highlighted. A red line is included to indicate the collision axis.	35

2.7	Schematic view of the STAR Time Projection Chamber [31]. Person is drawn in the picture for scale.	36
2.8	Electron drift velocity curves for different mixtures of gasses as a function of E/P . The curve indicated with asterisks is for P10 gas [32].	37
2.9	Typical cross section for the inner field cage (numbers indicate dimensions in mm) [33]. The main difference between the inner and outer field cages is a thicker layer of Nomex honeycomb and a thinner layer of aluminum in the inner field cage.	39
2.10	A cut away view of an outer subsector pad plane. The cut is taken along a radial line from the center of the TPC to the outer field cage so that the center of the detector is to the right. The figure shows the spacing of the anode wires relative to the pad plane, the ground shield grid, and the gated grid. The bubble diagram shows additional detail about the wire spacing. The inner subsector pad plane has the same layout except the spacing around the anode plane is 2 mm instead of the 4 mm shown here. All dimensions are in mm.[33]	40
2.11	Schematic of multi-wire proportional counter chamber and pad readout subsectors [34]. Gating grid and ground plane wires are 1 mm apart. Anode wires are 4 mm apart.	44
2.12	Position resolution across the transverse pad-rows and along the longitudinal z -axis of the TPC. The crossing angle is the angle between the particle momentum and the pad-row direction. The dip angle is the angle between the particle momentum and the drift direction, $\theta = \cos^{-1}(p_z/p)$ [33].	45
2.13	Schematic of endcap sector. The inner subsector has separated rows of narrow pads where the track density is the highest. The outer section has wider and longer pads to maximize signal collection in order to get the best dE/dx measurement.	46
2.14	The energy loss distribution for primary and secondary particles in the STAR TPC as a function of the p_T of the primary particle. The magnetic field was 0.25 T [33].	49
2.15	A cross-section drawing of the magnet steel [30]. The magnet steel serves as the return yolk for the magnetic field as well as the support structure for STAR.	50
2.16	The radial field integral plotted for three different radii in the drift volume at $\phi = 0^\circ$ and $z < 0$. [30].	51
2.17	The CTB barrel is a series of scintillator tiles that sit in aluminum trays around the circumference of the TPC. Each tray holds two radiators, two light guides, and two PMTs.[49]	53
2.18	Close up of ZDC construction.	54
3.1	Feynman diagrams for heavy quark photoproduction from (a) direct and (b)-(d) resolved photons [51].	58

3.2	There are two photoproduction channels for the ρ^0 in this study. In the diagram on the left, a virtual photon from the top gold nucleus fluctuates to a quark-antiquark pair and scatters off a Pomeron in the bottom nucleus to subsequently produce a ρ^0 . In the diagram on the right, the same process occurs as well as the exchange of additional photons which induce mutual Coulomb excitation and subsequent emission of neutrons from each nucleus. The exchange of the three (or more) photons actually occurs as three (or more) independent processes. . .	60
3.3	ρ^0 production cross section as a function of t . The lines indicate a fit to two exponentials corresponding to the coherent and incoherent cross sections at low and high t respectively [45].	61
3.4	Diagram for ρ^0 production from Equation 3.2.	63
3.5	The UPC topology trigger utilized the CTB divided into four quadrants: Top, Bottom, North, and South. The quadrants were established to trigger on back-to-back $\pi^+ \pi^-$ pairs resulting from the decay of a ρ^0 . The trigger required a coincidence between North and South, with Top and Bottom as vetoes to reject most cosmic ray events. . . .	66
3.6	ADC signal in the east ZDC for the minbias dataset. The overlaid curve is a fit with the sum of four gaussians. Four clear peaks from left to right show a signal for one, two, three, and four neutrons respectively. The ratio of the number of candidates in the 1n:2n:3n:4n peaks is 10:5:2.2:1.6:1.	67
3.7	Rapidity (left) and $M_{\pi\pi}$ (right) of the $\pi^+ \pi^-$ distributions for the topology (exclusive ρ^0 , top) and MB (Coulomb breakup, bottom) samples. The points with statistical error bars are the data, and the histograms are the simulations. The notch in the topology data around $y = 0$ is due to the explicit rapidity cut to remove cosmic ray backgrounds [68].	69
3.8	Examples of fitting functions for $R(t)$	74
3.9	(Top) Monte Carlo simulated minbias $t_{\perp} \sim p_T^2$ spectra for ρ^0 sample, $ y < 0.5$. The dotted line histogram is a simulation assuming that there is interference. The overlapping solid histogram is a simulation without interference. (Bottom) Efficiency histograms calculated for ‘interference’ (dotted) and ‘no interference’ (solid) cases.	75
3.10	Efficiency corrected t_{\perp} spectrum for ρ^0 from (top) minimum bias and (bottom) topology data, for midrapidity (left) and larger rapidity (right) samples. The points with error bars are the data, overlaid with the multi-parameter fit (solid line) prescribed in Equation 3.4 [68].	79
4.1	A cartoon with notation corresponding to Equation 4.2, depicting a p+p collision in which hadron jets are produced.	81

4.2	Dijet invariant mass distribution from $p+\bar{p}$ collisions at 1.8 TeV as measured by the CDF collaboration [54]. The dotted line (the very top line underlying the data) is a NLO prediction calculated with the HMRS B structure function. The two solid lines define the envelope of different LO QCD predictions which come from varying the renormalization scale.	82
4.3	(a) Efficiency corrected two-particle azimuthal distributions for minimum bias and central d+Au collisions, and for p+p collisions [60]. Curves are fits detailed in [63]. (b) Comparison of two-particle azimuthal distributions for central d+Au collisions to those seen in p+p and central Au+Au collisions [60]. The respective pedestals have been subtracted.	86
4.4	Cartoon depicting a multi-hadron trigger. A primary seed is selected and secondary seeds within a cone radius, R , are added to give the trigger p_T	88
4.5	Background subtracted azimuthal distributions for dihadron triggers (left) and multi-hadron triggers (right) for $12 < p_T^{trig} < 15$ GeV/ c and 4.0 GeV/ $c < p_T^{assoc} < 5.0$ GeV/ c . A minimum secondary seed of 3.0 GeV/ c is used.	89
4.6	Number of multi-hadron triggers as a function of the number of tracks in a cluster and p_T^{trig} with a minimum secondary seed cut of $p_T > 3.0$ GeV/ c	90
4.7	Number of multi-hadron triggers as a function of the number of tracks in a cluster and p_T^{trig} with a minimum secondary seed cut of $p_T > 4.0$ GeV/ c	90
4.8	Raw azimuthal distribution for multi-hadron triggers with a minimum secondary seed of 3.0 GeV/ c for $12 < p_T^{trig} < 15$ GeV/ c and 4.0 GeV/ $c < p_T^{assoc} < 5.0$ GeV/ c	91
4.9	Background subtracted azimuthal distribution for multi-hadron triggers with a minimum secondary seed of 3.0 GeV/ c for $12 < p_T^{trig} < 15$ GeV/ c and 4.0 GeV/ $c < p_T^{assoc} < 5.0$ GeV/ c . The solid line in the center indicates the division of the regions integrated for near and away-side yields.	92
4.10	Recoil yield per trigger for three p_T bins: $10 < p_T^{trig} < 12$ GeV/ c (circles), $12 < p_T^{trig} < 15$ GeV/ c (squares), and $15 < p_T^{trig} < 18$ GeV/ c (triangles). Data is presented on the left (Au+Au), PYTHIA simulations are presented on the right (p+p). A minimum secondary seed cut of $p_T > 3.0$ GeV/ c is applied.	93
4.11	Recoil yield per trigger for three p_T bins: $10 < p_T^{trig} < 12$ GeV/ c (circles), $12 < p_T^{trig} < 15$ GeV/ c (squares), and $15 < p_T^{trig} < 18$ GeV/ c (triangles). Data is presented on the left (Au+Au), PYTHIA predictions are presented on the right (p+p). A minimum secondary seed cut of $p_T > 4.0$ GeV/ c is applied.	93

4.12	Recoil yield per trigger for three p_T bins: $8 < p_T^{trig} < 10$ GeV/ c (circles), $10 < p_T^{trig} < 12$ GeV/ c (squares), and $12 < p_T^{trig} < 15$ GeV/ c (triangles). Results are presented for dAu data. A minimum secondary seed cut of $p_T > 3.0$ GeV/ c is applied.	95
4.13	$\Delta\phi$ correlations with mixed events. All charge combinations are used between seed tracks and associated tracks. A repetitive peak structure occurs as the effect of the TPC endcap sector boundaries.	96
4.14	$\Delta\phi$ correlations with mixed events. Only positive tracks are used for seed and associated tracks. A repetitive peak structure occurs as the effect of the TPC endcap sector boundaries.	97
4.15	$\Delta\phi$ correlations with mixed events. Only negative tracks are used for seed and associated tracks. A repetitive peak structure occurs as the effect of the TPC endcap sector boundaries.	98
4.16	$\Delta\phi$ correlations with mixed events. Only oppositely charged tracks are used for seed and associated tracks. A repetitive peak structure occurs as the effect of the TPC endcap sector boundaries.	99
4.17	Radial distributions of triggers with associated tracks from the same event (white histogram) and from different events (hatched histogram) with a minimum secondary seed cut of 2.0 GeV/ c . A guideline is drawn at $r = 0.3$ to show where the analysis cut falls on the data.	100
4.18	Radial distributions of triggers with associated tracks from the same event (white histogram) and from different events (hatched histogram) with a minimum secondary seed cut of 3.0 GeV/ c . A guideline is drawn at $r = 0.3$ to show where the analysis cut falls on the data.	101
4.19	Radial distributions of triggers with associated tracks from the same event (white histogram) and from different events (hatched histogram) with a minimum secondary seed cut of 4.0 GeV/ c . A guideline is drawn at $r = 0.3$ to show where the analysis cut falls on the data.	102
4.20	Background subtracted recoil yield per trigger for three p_T bins: $10 < p_T^{trig} < 12$ GeV/ c , $12 < p_T^{trig} < 15$ GeV/ c , and $15 < p_T^{trig} < 18$ GeV/ c . A minimum secondary seed cut of $p_T > 4.0$ GeV/ c is applied.	103
4.21	Comparison of background subtracted (solid triangles) and raw unsubtracted recoil yields per trigger for three p_T bins: $10 < p_T^{trig} < 12$ GeV/ c (upper left), $12 < p_T^{trig} < 15$ GeV/ c (upper right), and $15 < p_T^{trig} < 18$ GeV/ c (lower left). A minimum secondary seed cut of $p_T > 4.0$ GeV/ c is applied.	104

- B.1 The top left plot shows a comparison of the rapidity distributions from the data (points) and MC simulation (histogram). The bottom left plot shows a comparison of the invariant mass distributions from the data (points) and MC simulation (histogram). The top right plot gives the ratio of the rapidity distributions, MC to data. The bottom right plot gives the ratio of the invariant mass distributions, MC to data. The distributions are generated subject to the following trigger requirements: If there are multiple hits per CTB tray, only the last one is stored. No cut is made on the ADC value of the hit. The standard trigger simulation from PeCMaker is employed. 110
- B.2 The top left plot shows a comparison of the rapidity distributions from the data (points) and MC simulation (histogram). The bottom left plot shows a comparison of the invariant mass distributions from the data (points) and MC simulation (histogram). The top right plot gives the ratio of the rapidity distributions, MC to data. The bottom right plot gives the ratio of the invariant mass distributions, MC to data. The distributions are generated subject to the following trigger requirements: If there are multiple hits per CTB tray, the sum of the hits are tabulated as the ADC count of the tray. No cut is made on the ADC value of the hit. The standard trigger simulation from PeCMaker is employed. 111
- B.3 The top left plot shows a comparison of the rapidity distributions from the data (points) and MC simulation (histogram). The bottom left plot shows a comparison of the invariant mass distributions from the data (points) and MC simulation (histogram). The top right plot gives the ratio of the rapidity distributions, MC to data. The bottom right plot gives the ratio of the invariant mass distributions, MC to data. The distributions are generated subject to the following trigger requirements: If there are multiple hits per CTB tray, the sum of the hits are tabulated as the ADC count of the tray. A cut of > 3 ADC counts is required. The standard trigger simulation from PeCMaker is employed. 112
- B.4 The top left plot shows a comparison of the rapidity distributions from the data (points) and MC simulation (histogram). The bottom left plot shows a comparison of the invariant mass distributions from the data (points) and MC simulation (histogram). The top right plot gives the ratio of the rapidity distributions, MC to data. The bottom right plot gives the ratio of the invariant mass distributions, MC to data. The distributions are generated subject to the following trigger requirements: If there are multiple hits per CTB tray, only the last one is stored as the ADC count of the tray. No cut is made on the ADC value of the hit. No lookup tables are used for the trigger simulation. 113

- B.5 The top left plot shows a comparison of the rapidity distributions from the data (points) and MC simulation (histogram). The bottom left plot shows a comparison of the invariant mass distributions from the data (points) and MC simulation (histogram). The top right plot gives the ratio of the rapidity distributions, MC to data. The bottom right plot gives the ratio of the invariant mass distributions, MC to data. The distributions are generated subject to the following trigger requirements: If there are multiple hits per CTB tray, the sum of the hits are tabulated as the ADC count of the tray. No cut is made on the ADC value of the hit. No lookup tables are used for the trigger simulation. 114
- B.6 The top left plot shows a comparison of the rapidity distributions from the data (points) and MC simulation (histogram). The bottom left plot shows a comparison of the invariant mass distributions from the data (points) and MC simulation (histogram). The top right plot gives the ratio of the rapidity distributions, MC to data. The bottom right plot gives the ratio of the invariant mass distributions, MC to data. The distributions are generated subject to the following trigger requirements: If there are multiple hits per CTB tray, the sum of the hits are tabulated as the ADC count of the tray. A cut of > 3 ADC counts is required. No lookup tables are used for the trigger simulation. 115
- C.1 The upper left histogram compares the data with loose cuts (top, blue), tight cuts (middle, red) and background (bottom black histogram at the zero level). A peak is visible at $M_{\pi\pi} = M(K_s)$. This may be due to photoproduction of the ϕ , followed by $\phi \rightarrow K_s K_L$. Because the Q value of the ϕ decay is so low, most of the K_s still make the p_T cut; the K_L usually vanishes without decaying. The upper right plot compares the data and the Monte Carlo; except for the K_s , the agreement is excellent. The lower left plot shows the efficiency; for $M_{\pi\pi} > 550$ MeV/c, the efficiency is flat. The last plot shows the $M_{\pi\pi}$ resolution of about 8.3 MeV [73]. 117

- C.2 The upper left histogram compares the p_T spectra with loose (blue) and tight (red) cuts. Events with $p_T > 120$ MeV/ c appear consistent with incoherent ρ^0 production, $\gamma p \rightarrow \rho^0 p$. The upper right plot compares the 'Int' (blue) and 'Noint' (green) p_T spectra, after simulation and reconstruction. The middle left histogram compares the 'Int' (blue) and 'Noint' (green) p_T spectra directly from STARlight, with no detector effects. The middle right histogram shows the p_T resolution is centered at 0, with $\sigma=7.5$ MeV. The lower left histogram shows that the reconstruction efficiency is independent of p_T , except for the lowest bin, which is somewhat higher. This is probably due to p_T smearing. With the 'Int' spectrum (used here, since it matches the data better), the first bin has many fewer events than the next bin, so that there is smearing from bin 2 \rightarrow bin 1, but very little in the other direction. The lower right plot compares the p_T spectra of data (red), 'Int' (blue) and 'Noint' (green). [73] 118
- C.3 The upper left histogram compares the data with loose cuts (blue), tight cuts (red), and background (with loose cuts). The loose cut plot shows an enhancement for $|y| < 0.1$. This is likely due to cosmic rays, which are reconstructed as pairs with $y = 0$, $p_T=0$. The upper right histogram compares the data (red) and Monte Carlo (blue), while the lower left histogram shows the rapidity resolution, 0.01. This is very adequate for the analysis. The lower right histogram shows the efficiency as a function of rapidity. It is not flat, since the probability of a daughter pion being outside the TPC acceptance rises as rapidity rises, but since the data and MC agree well, this is no cause for concern. [73] 119
- C.4 The left plot shows the data with loose cuts (blue), tight cuts (red), and the background (black). With the loose cuts, a small rise is visible at $r \sim 3$ cm. This disappears once tighter cuts are imposed. The background rate is so high here because there is no cut on z . The plot on the right compares the data (red) and the Monte Carlo (blue). The agreement is good. [73] 120
- C.5 The upper left histogram compares the data with loose cuts (blue) and tight cuts (red), and the background (black). The upper right histogram compares the (red) data and Monte Carlo (blue). The lower right is the resolution estimated with the Monte Carlo ($zVertex-zMC$); the resolution is 2 cm. The lower left shows the efficiency as a function of $zVertex$. It is approximately flat within the ± 50 cm cut range. [73] 121

- C.6 The upper left histogram compares the data with loose cuts (top, blue), tight cuts (middle, red) and background (bottom black histogram at the zero level). A peak is visible at $M_{\pi\pi} = M(K_s)$. This may be due to photoproduction of the ϕ , followed by $\phi \rightarrow K_s K_L$. Because the Q value of the ϕ decay is so low, most of the K_s still make the p_T cut; the K_L usually vanishes without decaying. The upper right plot compares the data and the Monte Carlo; except for the K_s , the agreement is excellent. The lower left plot shows the efficiency; for $M_{\pi\pi} > 550$ MeV/c, the efficiency is flat. The last plot shows the $M_{\pi\pi}$ resolution of about 8.3 MeV. [73] 122
- C.7 The upper left histogram compares the p_T spectra with loose (blue) and tight (red) cuts. Events with $p_T > 120$ MeV/c appear consistent with incoherent ρ^0 production, $\gamma p \rightarrow \rho p$. The upper right plot compares the 'Int' (blue) and 'Noint' (green) p_T spectra, after simulation and reconstruction. The middle left histogram compares the 'Int' (blue) and 'Noint' (green) p_T spectra directly from STARlight, with no detector effects. The middle right histogram shows the p_T resolution is centered at 0, with $\sigma = 7.5$ MeV. The lower left histogram shows that the reconstruction efficiency is independent of p_T , except for the lowest bin, which is somewhat higher. This is probably due to p_T smearing. With the 'Int' spectrum (used here, since it matches the data better), the first bin has many fewer events than the next bin, so that there is smearing from bin 2 \rightarrow bin 1, but very little in the other direction. The lower right plot compares the p_T spectra of data (red), 'Int' (blue) and 'Noint' (green). [73] 123
- C.8 The upper left histogram compares the data with loose cuts (blue), tight cuts (red), and background (with loose cuts). The loose cut plot shows an enhancement for $|y| < 0.1$. This is likely due to cosmic rays, which are reconstructed as pairs with $y = 0$, $p_T = 0$. The upper right histogram compares the data (red) and Monte Carlo (blue), while the lower left histogram shows the rapidity resolution, 0.01. This is very adequate for the analysis. The lower right histogram shows the efficiency as a function of rapidity. It is not flat, since the probability of a daughter pion being outside the TPC acceptance rises as rapidity rises, but since the data and MC agree well, this is no cause for concern. [73] 124
- C.9 The left plot shows the data with loose cuts (blue), tight cuts (red), and the background (black). With the loose cuts, a small rise is visible at $R \sim 3$ cm. This disappears once tighter cuts are imposed. The background rate is so high here because there is no cut on z. The plot on the right compares the data (red) and the Monte Carlo (blue). The agreement is good. [73] 125

C.10	The upper left histogram compares the data with loose cuts (blue) and tight cuts (red), and the background (black). The upper right histogram compares the (red) data and Monte Carlo (blue). The lower right is the resolution estimated with the Monte Carlo (<i>zVertex-zMC</i>); the resolution is 2 cm. The lower left shows the efficiency as a function of <i>zVertex</i> . It is approximately flat within the ± 50 cm cut range. [73]	126
D.1	Background subtracted azimuthal distributions per trigger for multi-hadron triggers with a minimum secondary seed of 2.0 GeV/c for $8 < p_T^{trig} < 10$ GeV/c and successive slices of p_T^{assoc} as indicated on the plots.	128
D.2	Background subtracted azimuthal distributions per trigger for multi-hadron triggers with a minimum secondary seed of 2.0 GeV/c for $10 < p_T^{trig} < 12$ GeV/c and successive slices of p_T^{assoc} as indicated on the plots.	129
D.3	Background subtracted azimuthal distributions per trigger for multi-hadron triggers with a minimum secondary seed of 2.0 GeV/c for $12 < p_T^{trig} < 15$ GeV/c and successive slices of p_T^{assoc} as indicated on the plots.	130
D.4	Background subtracted azimuthal distributions per trigger for multi-hadron triggers with a minimum secondary seed of 2.0 GeV/c for $15 < p_T^{trig} < 18$ GeV/c and successive slices of p_T^{assoc} as indicated on the plots.	131
D.5	Background subtracted azimuthal distributions per trigger for multi-hadron triggers with a minimum secondary seed of 3.0 GeV/c for $8 < p_T^{trig} < 10$ GeV/c and successive slices of p_T^{assoc} as indicated on the plots.	132
D.6	Background subtracted azimuthal distributions per trigger for multi-hadron triggers with a minimum secondary seed of 3.0 GeV/c for $10 < p_T^{trig} < 12$ GeV/c and successive slices of p_T^{assoc} as indicated on the plots.	133
D.7	Background subtracted azimuthal distributions per trigger for multi-hadron triggers with a minimum secondary seed of 3.0 GeV/c for $12 < p_T^{trig} < 15$ GeV/c and successive slices of p_T^{assoc} as indicated on the plots.	134
D.8	Background subtracted azimuthal distributions per trigger for multi-hadron triggers with a minimum secondary seed of 3.0 GeV/c for $15 < p_T^{trig} < 18$ GeV/c and successive slices of p_T^{assoc} as indicated on the plots.	135
D.9	Background subtracted azimuthal distributions per trigger for multi-hadron triggers with a minimum secondary seed of 4.0 GeV/c for $8 < p_T^{trig} < 10$ GeV/c and successive slices of p_T^{assoc} as indicated on the plots.	136
D.10	Background subtracted azimuthal distributions per trigger for multi-hadron triggers with a minimum secondary seed of 4.0 GeV/c for $10 < p_T^{trig} < 12$ GeV/c and successive slices of p_T^{assoc} as indicated on the plots.	137
D.11	Background subtracted azimuthal distributions per trigger for multi-hadron triggers with a minimum secondary seed of 4.0 GeV/c for $12 < p_T^{trig} < 15$ GeV/c and successive slices of p_T^{assoc} as indicated on the plots.	138
D.12	Background subtracted azimuthal distributions per trigger for multi-hadron triggers with a minimum secondary seed of 4.0 GeV/c for $15 < p_T^{trig} < 18$ GeV/c and successive slices of p_T^{assoc} as indicated on the plots.	139

List of Tables

2.1	Summary of RHIC runs.	32
3.1	Coherent ρ^0 production cross section measured by STAR at $\sqrt{s_{NN}} = 200$ GeV accompanied by nuclear breakup and without breakup compared with previous STAR measurements at $\sqrt{s_{NN}} = 130$ GeV [46].	62
3.2	Quality cuts for identification of ρ^0 candidates in data.	70
3.3	Fitting Summary for different $R(t)$ fits.	76
3.4	Fits to the two upc data sets: topology and minbias.	78
4.1	Detector thresholds for the 2004 Au + Au Central trigger (Trigger Word = 15105). Values in the table are quoted in ADC counts unless otherwise specified.	87
4.2	Quality cuts invoked on tracks before including them in the multi-hadron trigger algorithm.	88

Chapter 1

Introduction

The field of relativistic heavy ion physics was born of experiments first attempted in the late 70's when physicists replaced the typical projectiles, protons, in particle physics accelerators with heavy ions. The intention of these early experiments was to understand compressed nuclear matter. Two fixed target facilities, the Bevalac¹, and the Synchrophasotron², pioneered the effort. The Bevalac accelerated varied species of nuclei up to center of mass energies of 2.32 GeV.

As technology improved, the field grew and by the mid 80's heavy ions were running at even higher energies at facilities like the AGS³ and the SPS⁴, both fixed target facilities. The top center of mass energies at the AGS and the SPS were 4.86 GeV and 17.3 GeV for Au+Au and p+p collisions, respectively. Both facilities could achieve even higher energies for lighter collision systems. The AGS reached the

¹the Billions of eV Synchrotron injected by the superHilac at Lawrence Berkeley National Laboratory

²at the Joint Institute for Nuclear Research in Dubna

³Alternating Gradient Synchrotron at Brookhaven National Laboratory

⁴Super Proton Synchrotron at CERN, the European Organization for Nuclear Research

threshold for strange quark production while the SPS reached the threshold for charm quark production. By the 90's plans for RHIC⁵, the first heavy ion collider, were being finalized (RHIC is discussed at length in Chapter 2). Since coming online in 2000, it has so far achieved Cu+Cu and Au+Au collisions at center of mass energies of 22.4, 62.4, and 200 GeV. Also, RHIC has successfully achieved d+Au collisions at 200 GeV and polarized p+p collisions at 200 and 500 GeV. Currently, an even higher energy collider experiment at the LHC⁶ is slated to begin in 2009 with Pb+Pb collisions at a center of mass energy of 10 TeV. In 2010, LHC will reach the design energy of 14 TeV for proton collisions and will start the 5.5 TeV Pb+Pb program.

Though the field of heavy ion physics has undergone a great evolution from the 70's to now, it began simply enough with the general idea of sorting out the properties of nuclear matter, where the collisional compression raises the density of the hot, dense interaction zone to a few times the density of normal nuclear matter⁷. At the time astrophysicists had posited that understanding neutron stars, the highly compressed remnants of supernovae, necessitated understanding the equation of state of very dense hadronic matter [2], specifically the isothermal compressibility.

A proposed radial density profile of a neutron star, circa the mid 70's, is shown in Figure 1.1 including a mention of quark matter at the very dense core. This quark matter prediction, which was a de-confined state of quarks and gluons postulated by QCD⁸, preceded what would become the main goal of heavy ion physics, to map the entire QCD phase diagram. The quark matter at the center of a neutron star was

⁵the Relativistic Heavy Ion Collider at Brookhaven National Lab

⁶Large Hadron Collider

⁷density of normal nuclear matter: $\rho^0 = 0.15$ baryons/ $f m^3$

⁸Quantum Chromodynamics

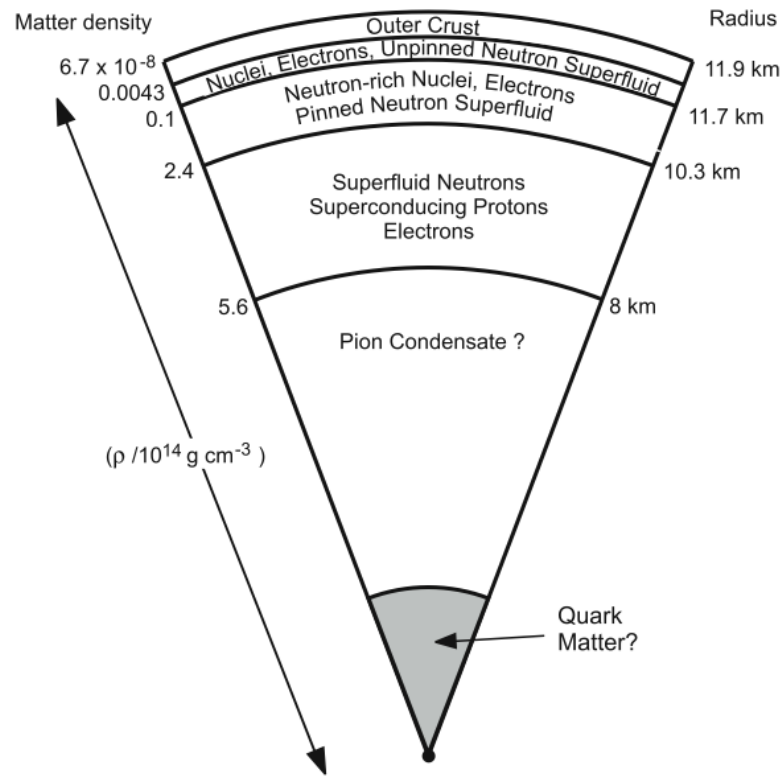


Figure 1.1. The radial density profile of neutron stars reflecting the hadronic EOS and the general QCD phase diagram [2].

just one point on the diagram. Figure 1.2 shows a semi-quantitative sketch of the QCD phase diagram. Neutron stars occupy a small corner of the diagram occurring at very low temperature but very high baryon density. The other extreme occurs at very high temperature and low baryon density, the regime of the early universe and current heavy ion colliders.

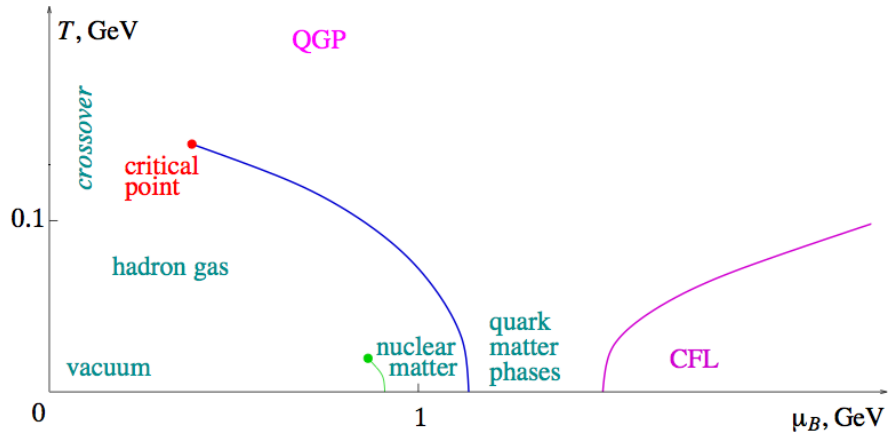


Figure 1.2. A contemporary view of the QCD phase diagram - a semi-quantitative sketch [3].

1.1 Heavy-ion Collisions: Mapping the QCD Phase Diagram

The way heavy ion colliders achieve quark matter, or the QGP⁹ as it is known in the vernacular of heavy ion physics, is to use the large number of inelastic nucleon-nucleon collisions in the event of two nuclei colliding to deposit a significant amount of energy in a very tiny amount of space. To illustrate, the order of magnitude of the energy density in RHIC collisions is estimated to be $\sim 1 \text{ GeV}/\text{fm}^3$ [10].

In Figure 1.3, the space-time evolution of a heavy ion collision is diagrammed. The incoming nuclei, each labeled A , collide to set off a series of steps which are illustrated along the vertical time axis. The figure is divided into two halves depending on the subsequent energy density in the collision region. If the energy density is not

⁹Quark Gluon Plasma

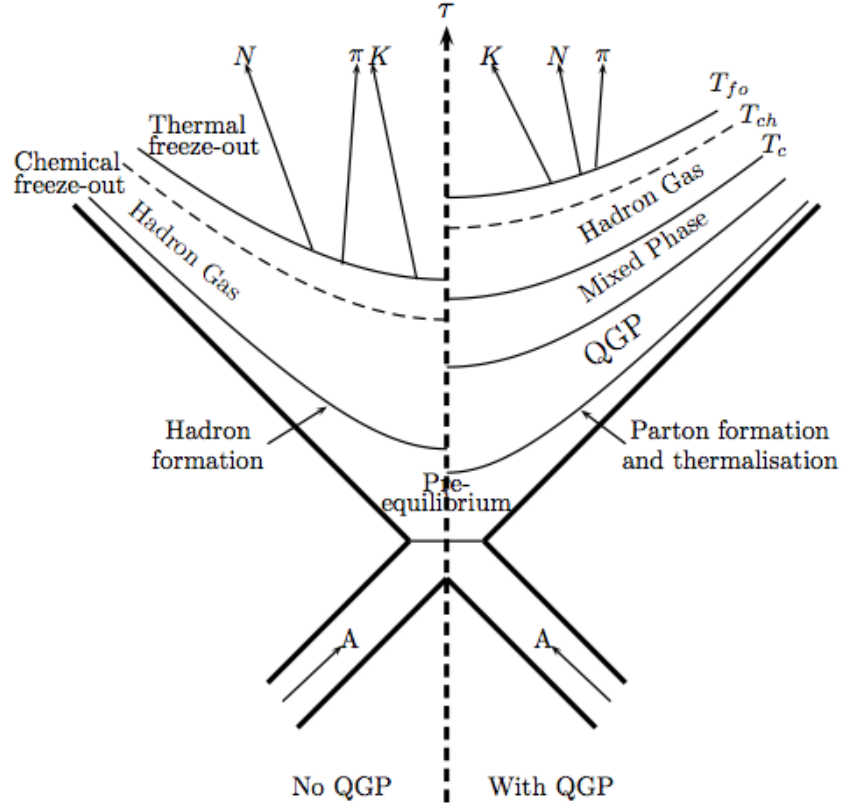


Figure 1.3. Two scenarios for the evolution of the system created in a relativistic nucleus-nucleus collision. The left-hand side shows the evolution for the case of no QGP being created, while the right-hand side shows the expected evolution of the system including QGP formation. Lines of constant temperature indicate hadronization (T_c), chemical freeze-out (T_{ch}), and kinetic freeze-out (T_{fo}) [4].

high enough, the left side of the figure shows the evolution of the system without QGP formation. In the case that the threshold energy density is reached, the right side shows the evolution with QGP formation. Hyperbolic lines on the diagram are isochrons, indicating a constant proper time.

In the scenario without QGP formation, hadrons form around $1 \text{ fm}/c$. The gas of hadrons is still hot enough for there to be inelastic collisions and the particle species

distribution is not fixed until about 3 fm/ c . The point at which the species yields are fixed is called chemical freeze-out. The gas of hadrons continues to interact through elastic collisions as it further expands and cools until the point where relative distance between particle exceeds the range of the strong force. This point is called kinetic freeze-out. The particles continue to move outward in all directions until they decay or are stopped by the material of the detector of the experimental hall.

At extremely high collision energies, nucleon-nucleon collisions occur, but the nucleons do not stop in the collision zone. Instead, participating nucleons leave energy behind in the collision zone. What remains after the collision is a nearly baryon-free vacuum with a very high energy density. In this scenario, the highly Lorentz contracted nuclei, as shown in Figure 1.4, are “transparent” to each other, since the individual nucleons continue with almost all of their original beam momentum. It is as if the nuclei pass through each other. In these high energy collisions, the QGP forms. The energy density is high enough to disassociate nucleons into their constituent quarks. The phase transition stabilized the plasma and allows for an extended lifetime. Then hadronization occurs from distillation of a QGP rather than particle production in nucleon-nucleon collisions.

The QGP is short-lived, however, as quarks have a strong affinity for their bound states. Hadronization occurs at the critical temperature, T_c , as the system of unbound quarks and gluons begins to expand and cool. There is a mixed phase temporarily as all the quarks finish hadronizing, where hadrons co-exist with free quarks and gluons. Next chemical freeze-out sets in at T_{ch} when the hadrons cease inelastic collisions. Finally, the particles are measured after the kinetic freeze-out, at T_{fo} when hadrons

stop colliding elastically.

If the QGP is indeed a phase of matter with an equation of state then it should be quantified. Clearly it cannot be quantified in the same ways that physicists probe other forms of matter. However, there are experimental observables which come from measuring the final-state particles and extrapolating back to the initial-state QGP.

1.1.1 Introduction to Geometrical and Kinematic Variables

Discussing signatures of the QGP warrants an introduction to the features of a heavy ion collisions, from geometry to kinematic variables.

As shown in Figure 1.4, the basic picture of a collision involving two nuclei at a center of mass energy of 200 GeV is that of two Lorentz contracted pancakes made of nucleons passing through each other. These circular pancakes can collide in one of three scenarios classified in terms of the impact parameter \vec{b} , a variable defined as the vector quantity directed from the center of one nucleus to the other. The three scenarios are as follows:

- a central collision, top 10% of the total hadronic cross section ($|\vec{b}| < R_A/3$)
- a semi-central to peripheral collision ($R_A/3 < |\vec{b}| < 2R_A$)
- an ultra-peripheral collision ($|\vec{b}| > 2R_A$)

It is important to quantify the centrality of a given collision experimentally. To this end the Glauber model is used to predict the number of nucleons that actually participate in a heavy ion collision and the total number of nucleon-nucleon collisions

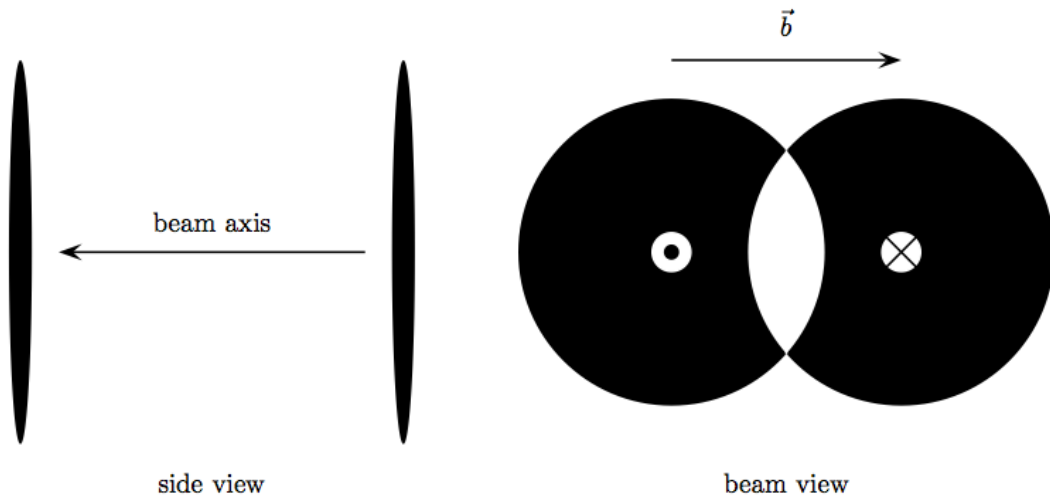


Figure 1.4. Two views of a heavy ion collision at a center-of-mass energy of 200 GeV. On the left side of the figure, a side perspective is shown. The ions look like pancakes Lorentz contracted along the direction of travel with an aspect ratio of 100:1 (height to thickness). On the right side of the figure, a perspective along the beam axis is shown with the left nucleus traveling out of the page and the right nucleus traveling into the page. The collision is a peripheral collision with the overlap region indicated in white.

for a given impact parameter b . Further details of the Glauber model are provided in Appendix A.

The importance of understanding how many nucleons participate and the number of nucleon-nucleon collisions is that experimental observables scale with N_{part} or N_{coll} . For example, both transverse energy and particle multiplicity scale with N_{part} while hard, perturbative processes scale with N_{coll} as indicated by perturbative Quantum Chromodynamics[5].

Figure 1.5 includes multiplicity distributions of Au+Au collisions at three values of $\sqrt{s_{NN}}$: 19.6, 130, and 200 GeV. Since N_{part} and N_{coll} cannot be measured directly, variables such as particle multiplicity, which is directly correlated to N_{part} , are used in conjunction with the Glauber model to parse the data into centrality bins. The centrality bins in Figure 1.5 are shown in terms of percentages of the total cross section.

Another important definition to make with respect to the geometry of heavy ion collisions is that of the “reaction plane” of the event. The reaction plane is defined by the impact parameter and beam axis as shown in Figure 1.6. Particle emission with respect to the reaction plane is an important measurement which is discussed in section 1.1.2.

Variables typically used to describe an outgoing particle of mass m , with measured quantities of momentum \vec{p} , and emission angle with respect to the beam axis, θ , are as follows:

- polar angle, $\theta = \arctan(p_T/p_z)$

- azimuthal angle, $\phi = \arctan(p_x/p_y)$
- transverse momentum, $p_T = |\vec{p}| \sin \theta = \sqrt{p_x^2 + p_y^2}$
- transverse mass $m_T = \sqrt{E^2 - p_T^2}$
- rapidity, $y = \frac{1}{2} \ln(E + p_z)(E - p_z)$ ($E = m_T \cosh y$, $p_T = m_T \sinh y$)

In dealing with relativistic velocities, rapidity is particularly useful as it is additive under Lorentz boosts, whereas velocity is not.

- pseudorapidity, $\eta = -\ln(\tan(\theta/2))$

Pseudorapidity is a useful quantity experimentally in that it can be calculated for unidentified particles with just a measured angle without knowing the mass or momentum of a particle. Furthermore, $\eta \approx y$ when $p \gg m$.

1.1.2 Initial-State Energy Deposition

The initial energy density in the wake of a heavy ion collision can indicate favorable conditions for the formation of a QGP. Bjorken postulated that the rapidity density distributions of produced particles could indicate the initial energy density [8]. He assumed particle production was Lorentz-boost invariant near midrapidity. Therefore the particles measured near mid-rapidity would be evenly distributed with respect to rapidity. He assumed “transparency” of the initial colliding nuclei, therefore, the net baryon density at midrapidity post-collision is assumed to be zero. The rapidity density distribution should have a central plateau flanked by edges augmented by the projectile and target nucleons which retain most of their initial rapidity. As seen in

Figure 1.8, the Phobos experiment has published results on charged particle yields over a large range of pseudo-rapidity [9]. There is a broad plateau around mid-rapidity the width of which increases with increasing collision energy.

By solving hydrodynamic equations with the initial condition that the rapidity distribution has a central plateau at sufficiently high energy, Bjorken derived a quantitative prediction for the initial energy density [8]:

$$\epsilon_{Bj} = \frac{1}{A_{\perp}\tau} \frac{dE_T}{dy}. \quad (1.1)$$

Here the variables A_{\perp} and τ are taken to be the transverse overlap area of the nuclei and the formation time of the QGP, respectively.

In Figure 1.9, the PHENIX collaboration has presented results on $\epsilon_{Bj} \cdot \tau$ (assuming a formation time of $\tau = 1 \text{ fm}/c$) as a function of centrality and for different Au+Au collision energies. Predictably, the energy density increases with collision energy and centrality (N_p). PHENIX concludes that at $\sqrt{s_{NN}} = 200 \text{ GeV}$, for the most central collisions, $\epsilon_{Bj} \cdot \tau = 5.4 \text{ GeV}/\text{fm}^2 \cdot c$, which, assuming $\tau = 1 \text{ fm}/c$, is beyond the nominal value of $\sim 1 \text{ GeV}/\text{fm}^3$ necessary for the QGP [10].

1.1.3 Chemical and Kinetic Freeze-Out

The second law of thermodynamics states that the entropy of an isolated system will tend to increase over time toward thermodynamic equilibrium. As the QGP hadronizes and evolves there is indeed evidence of thermalization.

Chemical freeze-out occurs when the energy density of the medium drops to the point that relative hadron species abundances are fixed. These hadrons will still in-

teract through elastic collisions until kinetic freeze-out when the system is sufficiently diffuse such that all elastic collisions cease.

Since chemical freezeout is defined as the point at which the quantities of particle species are fixed, studying the relative yields in the final state can give information about chemical freeze-out. Statistical models are used to extract the chemical freeze-out temperature as well as chemical potentials. Particle ratios are studied because systematic effects can be divided out without the need for corrections.

The statistical ensemble employed to describe the particles produced by the QGP is the grand canonical ensemble. The main feature of the grand canonical ensemble is that both the energy and number of particles is assumed to fluctuate between the equilibrated fireball and a surrounding ‘reservoir’. The partition function for a grand canonical ensemble is:

$$Z = \sum_i \exp\left(\frac{-E_i - \mu N_i}{T}\right) \quad (1.2)$$

where E_i and N_i are the energy and number of particles of the i^{th} particle species with the chemical potential μ .

Taking this generic partition function, the density of particles of a certain species i can be derived [24]:

$$n_i = \frac{g_i}{2\pi^2} \int_0^\infty \frac{p^2 dp}{\gamma_s \exp[(E_i(p) - \mu_i)/T] \pm 1} \quad (1.3)$$

here g_i indicates spin degeneracy, p_i is the particle momentum, E_i is its total energy, and μ_i its chemical potential. In addition, the chemical potential term is actually

comprised of three terms:

$$\mu_i = \mu_B B_i - \mu_S S_i - \mu_{I_B} I_i^3$$

B_i , S_i , and I_i^3 are taken as the baryon, strangeness, and third-component of the isospin quantum numbers for the i^{th} particle species.

With μ , γ_s and T as the free model parameters, particle ratio data can be fit so that the free parameters are optimized to deliver the most accurate predictions. The strangeness suppression factor, γ_s , is defined as [25] :

$$\gamma_s \equiv \frac{\text{strangeness density}}{\text{equilibrium density}}$$

The strangeness suppression factor parameterizes how far the population of strange hadrons deviates from chemical equilibrium. Very good agreement is achieved between model and data as seen in Figure 1.10.

The circular markers in Figure 1.10 indicate particle yield ratios extracted by the STAR collaboration for Au+Au collisions at $\sqrt{s_{NN}} = 200$ GeV. The overlapping horizontal lines are the statistical model fits with the following parameters [12]:

- $T_{ch} = 163 \pm 4$ MeV
- $\mu_B = 24 \pm 4$ MeV
- $\gamma_s = 0.99 \pm 0.07$

The values are consistent with values obtained using similar models to fit other RHIC data [24, 26]. The inset plot shows the measured strangeness suppression factor, γ_s , as a function of centrality. That the value obtained for the most central collisions

is consistent with unity is a significant indication that the system created in central collisions achieves chemical equilibrium.

Furthermore, the good agreement between the models and data indicates that for the lightest quark flavors, up, down, and strange, chemical equilibrium is reached at the temperature extracted, $T_{ch} = 163$ MeV [1, 28].

The point at which the hadrons resulting from the initial QGP no longer have elastic collisions, i.e. that the mean free path is approximately the same as the system size, is called kinetic freeze-out [27]. The particles will free stream from this point until they interact with the detector medium. The parameters of kinetic freeze-out, radial flow velocity, β_T , and temperature, T_{fo} , can be inferred from spectral shapes of the transverse mass or transverse momentum distributions as shown in Figure 1.11.

As opposed to a scenario where there is emission from a static source and thermalization is purely due to random motion, the initial conditions of a heavy ion collision, namely a source which detonates, leads to a radial “flow” of the produced particles. This means the produced particles behave collectively. In fact, collective flow is unique to heavy ion collisions (as opposed to p+p collisions) and subsequently is an interesting signature to study and quantify the QGP.

The blast-wave model is a hydrodynamically-inspired model used to fit the shapes of spectra measured in heavy ion collisions [13]. It was derived from fits to data collected by the NA35 experiment from fixed-target collisions with a sulfur projectile at 200 AGeV. It assumes an expanding thermal source with Bjorken’s assumption of longitudinally invariant particle production [8] and a transverse flow velocity profile where the velocity depends on the proximity to the center of the fireball created in

the heavy ion collision. Particles further out move faster than those closer to the center. The expression for the transverse velocity, β_T , is [13]:

$$\beta_T(r) = \beta_s \left(\frac{r}{R} \right)^n;$$

this equation is applied in a region $0 \leq r \leq R$ where β_s is the surface velocity and n is a parameter used to vary the steepness of the profile.

The full parameterization of the transverse mass spectrum goes as [13]:

$$\frac{dN}{m_T dm_T} \propto \int_0^R r dr m_T I_o \left(\frac{p_T \sinh \rho(r)}{T_{\text{kin}}} \right) K_1 \left(\frac{m_T \cosh \rho(r)}{T_{\text{kin}}} \right)$$

I_o and K_o are modified Bessel functions and the transverse rapidity is defined as $\rho(r) \equiv \tanh \beta_T(r)$.

Results from applying a blast-wave fit to STAR data from Au+Au collisions at $\sqrt{s_{NN}} = 200$ GeV are shown in Figure 1.12. Various abundantly-produced hadron species, (pions, kaons, and protons) were simultaneously fit for different centrality slices. In addition, data for two rarer strange hadrons, the ϕ and Ω were also analyzed. The results are plotted with χ^2 contours as a function of freeze-out temperature, T_{fo} , and transverse flow velocity, $\langle \beta_T \rangle$. The collective velocity increases with increasing centrality, while the kinetic freeze-out temperature decreases with increasing centrality. The implication is that the medium created in more central collisions expands faster and cools more extensively before freeze-out than the medium created in more peripheral collisions.

1.1.4 Hard Probes

Another important feature of heavy ion collisions is the production of high momentum particles which probe the QGP produced in the collisions. High momentum, “hard” partons originate from hard scatterings between nucleons in the initial collision between nuclei. As the partons traverse the medium they lose energy in colored interactions via elastic scatterings and gluon radiation [14, 15, 16].

There are two main experimental results which support parton energy loss, also known as jet quenching. Both the nuclear modification factor and correlated di-hadron distributions provide support for jet quenching in the QGP.

In the absence of nuclear effects including shadowing [5] and the Cronin effect [17], or gluon saturation [51], hard processes should scale with the number of binary collisions. The nuclear modification factor was devised to test this expectation. It is defined as:

$$R_{AB} = \frac{d^2 N_{AB}/dp_T dy}{\langle N_{coll}^{AB} \rangle d^2 N_{pp}/dp_T dy} \quad (1.4)$$

here $\langle N_{coll}^{AB} \rangle$ ($= \langle T_{AB} \rangle \sigma_{pp}$), is the average number of incoherent binary collisions in a collision of two nuclei of species A and B . In Appendix A, $\langle T_{AB} \rangle$ is the nuclear overlap function dependent on the geometry of an event. Moreover, σ_{pp} is the experimental cross section for inelastic p+p collisions. By definition then, an R_{AB} of 1 would indicate that nuclear collisions are simply the superposition of p+p collisions scaled by the number of binary collisions.

In Figure 1.13, R_{AB} is shown for two data sets, d+Au and Au+Au both at $\sqrt{s_{NN}} = 200$ GeV. The filled circles and triangles are d+Au data points. These measurements

provide a reference for studying nuclear effects like shadowing and the Cronin effect [19]. The filled stars from central Au+Au data. The data points clearly fall below the value of 1, indicating suppression of hadron production, especially at higher values of transverse momentum. By definition, the suppression of high- p_T hadrons is an experimental signature of jet quenching as high- p_T hadrons come from hard partons. A lack of high- p_T hadrons indicates that hard partons have lost energy traversing the QGP.

Discussion of the second signature mentioned, correlated di-hadron distributions, will be delayed until Chapter 4.

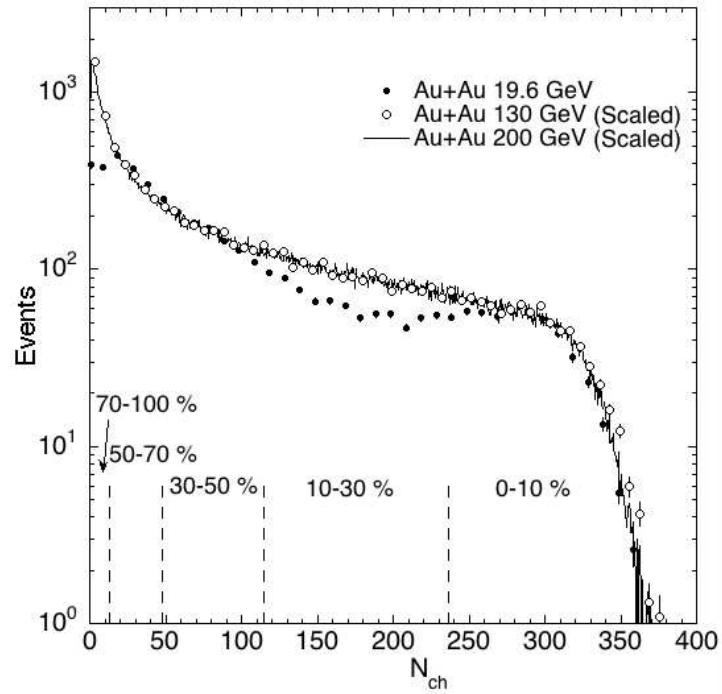


Figure 1.5. Multiplicity distributions of Au+Au collisions at three energies: 19.6 (dots), 130 (open circles), and 200 GeV (solid line). Dashed vertical lines indicate the centrality cuts used in the 19.6 GeV spectra analysis [6].

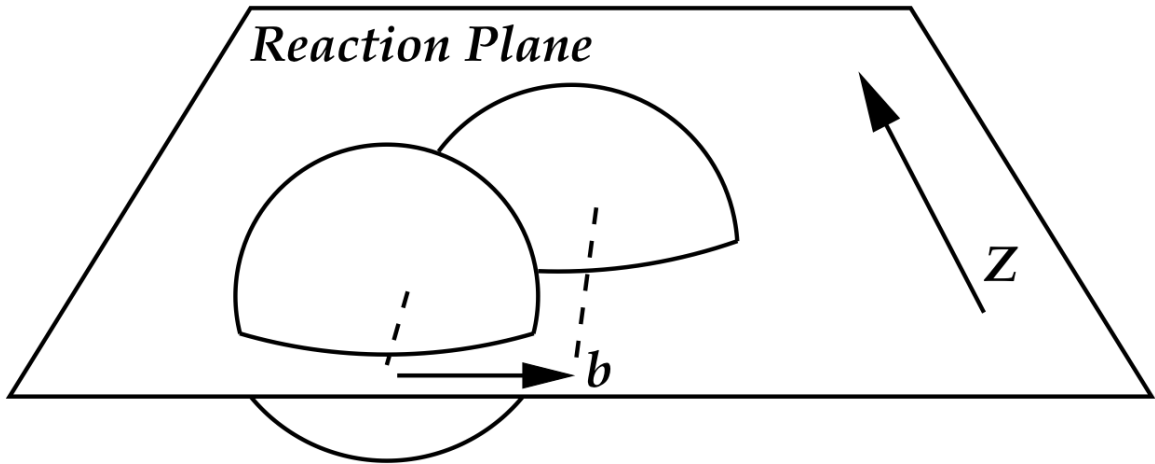


Figure 1.6. Diagram showing the definition of reaction plane as the plane defined by the impact parameter between the two nuclei and the beam axis.

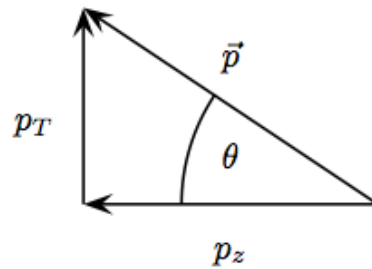


Figure 1.7. Vector diagram indicating for a particle of momentum \vec{p} with respect to the beam axis defined as the z-axis, the definition of transverse momentum, p_T , and the angle θ .

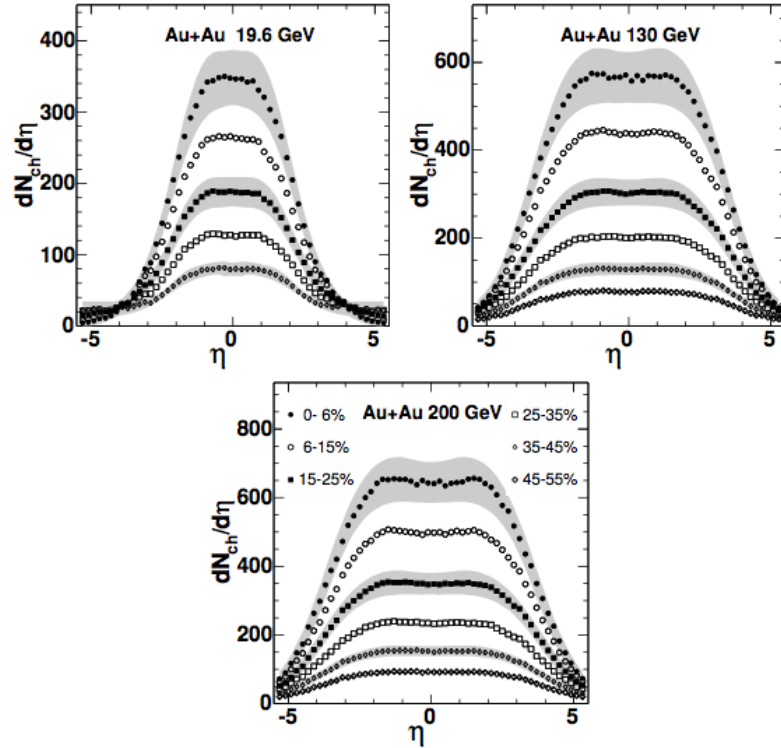


Figure 1.8. Pseudorapidity density of charged particles emitted in Au+Au collisions at three different values of the nucleon-nucleon center-of-mass energy [9]. Data are shown for a range of centralities, labeled by the fraction of total inelastic cross section in each bin, with smaller numbers being more central. Grey bands shown for selected centrality bins indicate the typical systematic uncertainties (90% C.L.). Statistical errors are smaller than the symbols [11].

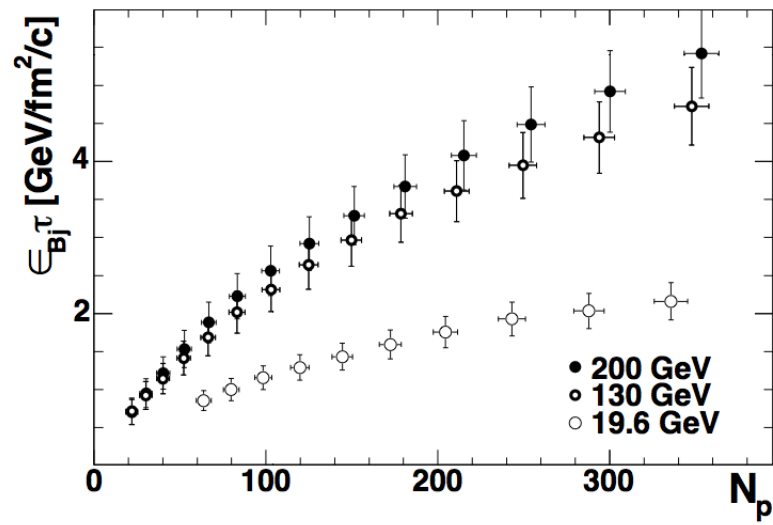


Figure 1.9. The Bjorken energy density, $\epsilon_{Bj} \cdot \tau$, deduced from PHENIX data at three RHIC energies [10].

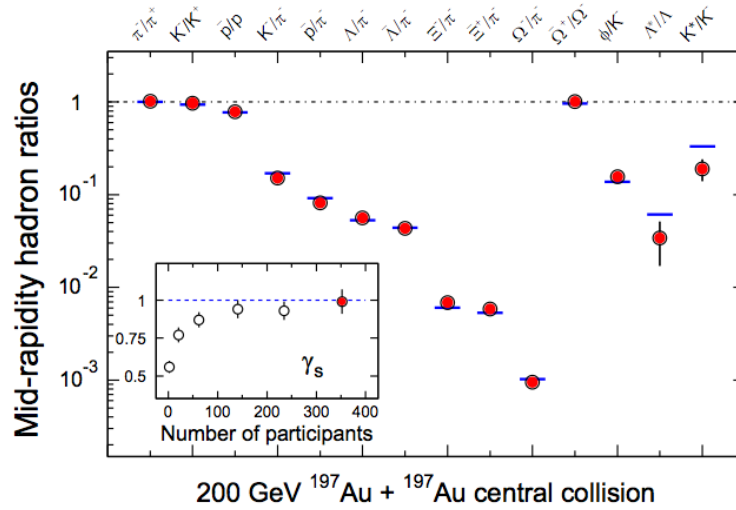


Figure 1.10. Ratios of p_T -integrated midrapidity yields for different hadron species measured in STAR for central Au+Au collisions at $\sqrt{s_{NN}} = 200$ GeV. The horizontal bars represent statistical model fits to the measure yield ratios for stable and long-lived hadrons. The fit parameters are $T_{ch} = 163 \pm 4$ MeV, $\mu_B = 24 \pm 4$ MeV, $\gamma_s = 0.99 \pm 0.07$ [12]. The variation of γ_s with centrality is shown in the inset, including the value (leftmost point) from fits to yield ratios measured by STAR for 200 GeV p+p collisions [1].

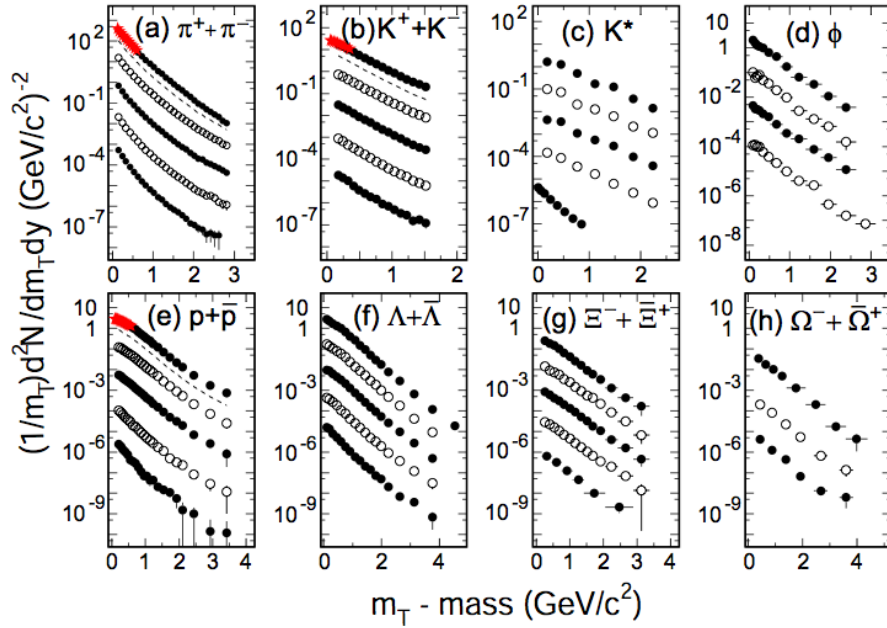


Figure 1.11. Hadron spectra measured by the STAR collaboration [20, 21, 22]. The spectra are from Au+Au collisions at $\sqrt{s_{NN}} = 200$ GeV measured at mid-rapidity. In each panel centrality increases from bottom to top. For K^* the lowest points come from p+p collisions at 200 GeV. Dashed curves in (a), (b), and (e) are from minimum-bias collisions [1].

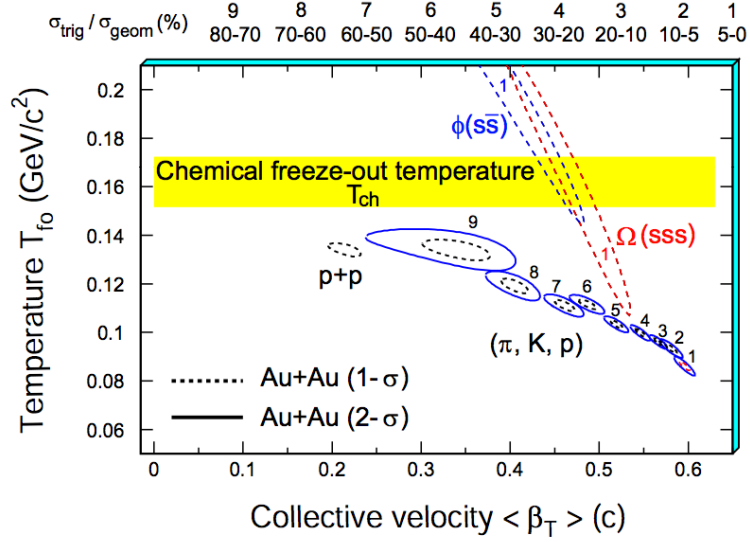


Figure 1.12. χ^2 contours resulting from simultaneous blast-wave fits to several species of produced hadrons, π , K , and p as well as for the most central data for multi strange hadrons ϕ and Ω [23]. The top axis shows the nine centrality bins applied to the data from Au+Au collisions at $\sqrt{s_{NN}} = 200$ GeV [12]. The bins range from 70-80% to top 5%, left to right. Results from p+p collisions are included as well. The dashed and solid lines are 1σ and 2σ contours, respectively.

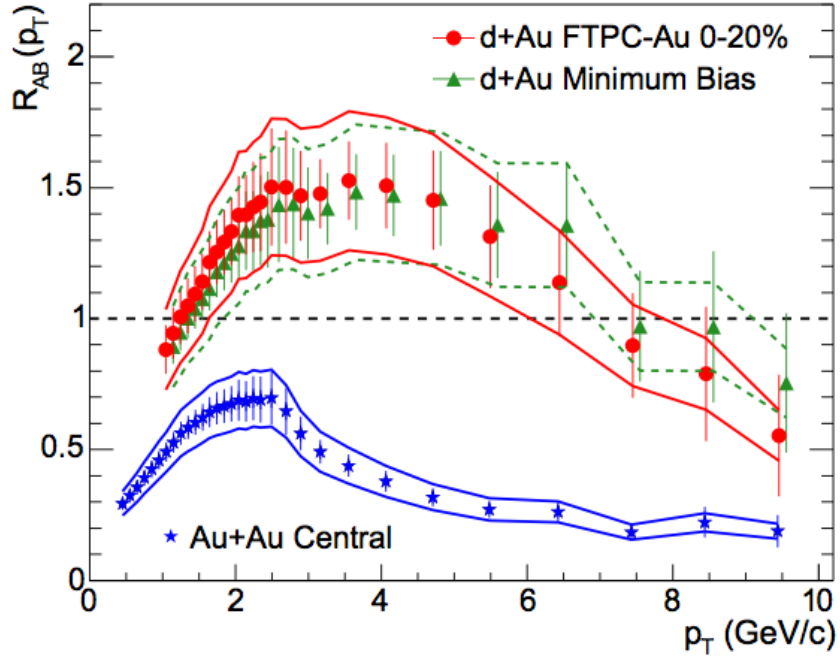


Figure 1.13. $R_{AB}(p_T)$ from Eq. 1.4 for minimum bias and central d+Au collisions, and central Au+Au collisions [18]. The minimum bias d+Au data are displaced 100 MeV/c to the right for clarity. The bands show the normalization uncertainties, which are highly correlated point-to-point and between the two d+Au distributions [63].

Chapter 2

Experimental Facilities

The STAR¹ experiment is the detector facility at which the data for this thesis were collected. The experiment began taking data in the year 2000 after over a decade of careful design, planning, and assembly. It resides at BNL², one of ten national laboratories funded by the US Department of Energy. Originally, the STAR experiment was one of four experiments at RHIC³ : STAR, PHENIX⁴, PHOBOS⁵, and BRAHMS⁶. STAR and PHENIX, the two larger experiments, are still actively taking data as of the writing of this thesis.

STAR will be discussed at great length in this thesis, but a brief description of the other experiments will be given here.

¹Solenoidal Tracker at RHIC

²Brookhaven National Laboratory

³Relativistic Heavy Ion Collider

⁴Pioneering High Energy Nuclear Interaction eXperiment

⁵named for one of the moons of Mars

⁶Broad Range Hadron Magnetic Spectrometers Experiment at RHIC

PHENIX, the other large experiment at RHIC, was designed with a smaller acceptance than the STAR experiment, but faster detectors with the intention of triggering on rare probes with good particle identification and discrimination of hadrons, leptons, and photons. Four spectrometer arms are the major design elements of the experiment. The geometrical acceptance of each spectrometer is ~ 1 steradian. The two forward muon

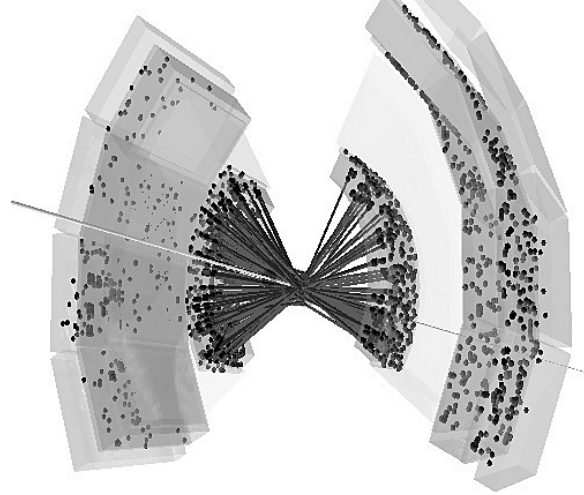


Figure 2.1. The PHENIX event display.

spectrometers cover a pseudo-rapidity range of $1.1 < |\eta| < 2.4$ and full azimuth. The two central spectrometer arms are positioned north and south with pseudorapidity coverage of $|\eta| < 0.35$ and are used for the detection of electrons, hadrons, and photons. Tracking sub-systems in the central arms have an azimuthal acceptance of $\frac{\pi}{2} \times 2$ radians, as seen in Figure 2.1.

PHOBOS was one of the two smaller and more specialized experiments at RHIC. The smaller experiments were intended to be complementary to the larger experiments, as well as being easily replaced or reconfigured if deemed necessary.

PHOBOS' main elements were a series of ring multiplicity detectors surrounding the beampipe with nearly 4π steradians of coverage and two small acceptance spectrometer arms. It also had TOF⁷ screens for particle identification. Its main

⁷Time of Flight

strengths were particle identification at midrapidity and multiplicity measurements across a broad range of pseudo-rapidity and transverse momentum.

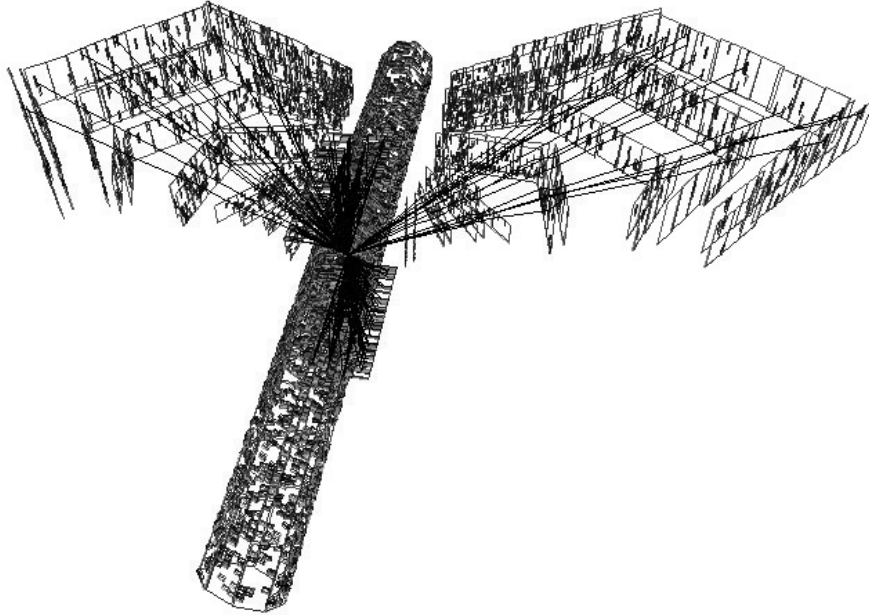


Figure 2.2. The PHOBOS event display.

BRAHMS was the other of the two smaller RHIC experiments. It utilized two small solid-angle spectrometers with coverage of only a few milliradians, as seen in Figure 2.3. The unique capability of the spectrometers was their ability to rotate horizontally about the collision point to measure hadron production over four units of rapidity. One pointed in the forward direction for high momentum particles and the other, at the opposite side of the collision region, covered the midrapidity region. Ultimately, the experiment provided detailed particle yield measurements over a large range of rapidity and transverse momentum.

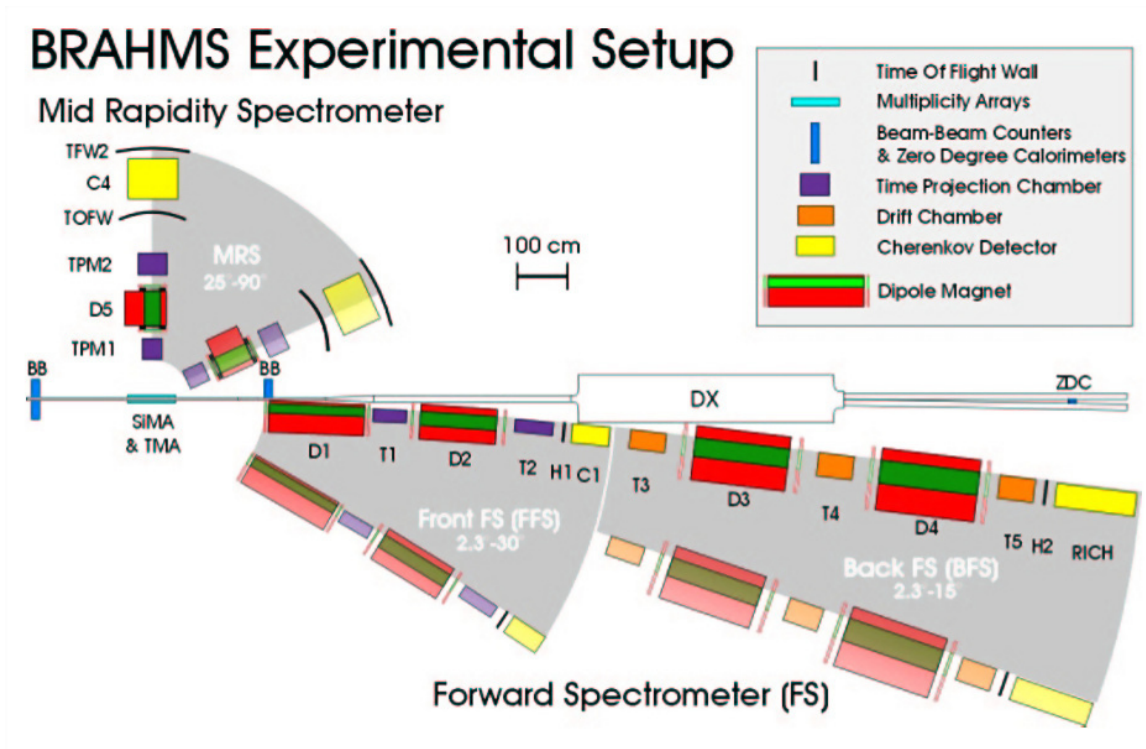


Figure 2.3. The BRAHMS detector.

2.1 The Relativistic Heavy Ion Collider

The RHIC facility is the first accelerator in the world to collide heavy ions. In a collider, the projectile and target move toward each other, whereas only the projectile moves in a fixed-target experiment. Because of this, a collider can provide an extended energy reach beyond that which can be obtained with a fixed-target setup. This is because with a fixed-target, the amount of beam energy available to go into particle production is limited by the fact that one needs to account for the kinetic energy associated with boosting the interaction zone to the center of mass rapidity. In a collider, with both beams moving with similar momentum in opposite directions, the rapidity of the interaction zone is zero, and all the energy brought into the

collision by the beams is, in principle, available for particle production. The center of mass energy for each setup is expressed in equations 2.1 and 2.2 where E is the beam energy, and m is the mass of the particles involved. In the case of the fixed target the subscripts 1 and 2 represent the projectile and the target, respectively.

$$E_{\text{cm}}^{\text{fixed}} = \sqrt{m_1^2 + m_2^2 + 2E_1m_2} \quad (2.1)$$

$$E_{\text{cm}}^{\text{collider}} = \sqrt{m_1^2 + m_2^2 + 2E_1E_2 - 2\vec{p}_1 \cdot \vec{p}_2} \quad (2.2)$$

As a synchrotron, RHIC utilizes varying electric and magnetic fields to guide bunches of ions in opposite directions around a quasi-circular path roughly 3.8 km long. Twelve feet underground, the clockwise (blue) and counter-clockwise (yellow) rings are buried. Large pipes house two smaller beam pipes only a few inches across surrounded by RHIC's 1,740 superconducting magnets. These magnets, which operate at a temperature of 4.5 K, are mounted to produce the magnetic fields which guide and collimate ion or proton bunches around the rings.

As seen in Figure 2.4 there are six crossing points around the RHIC rings. In one of these crossing points (4 o'clock), there is an RF ⁸ cavity system which provides the electric field energy kick the beams receive as they traverse their interlaced orbits. Though the RHIC RF cavity system does most of the work to accelerate gold ions up to their top energy of 100 GeV, there are several acceleration steps that occur before

⁸Radio Frequency

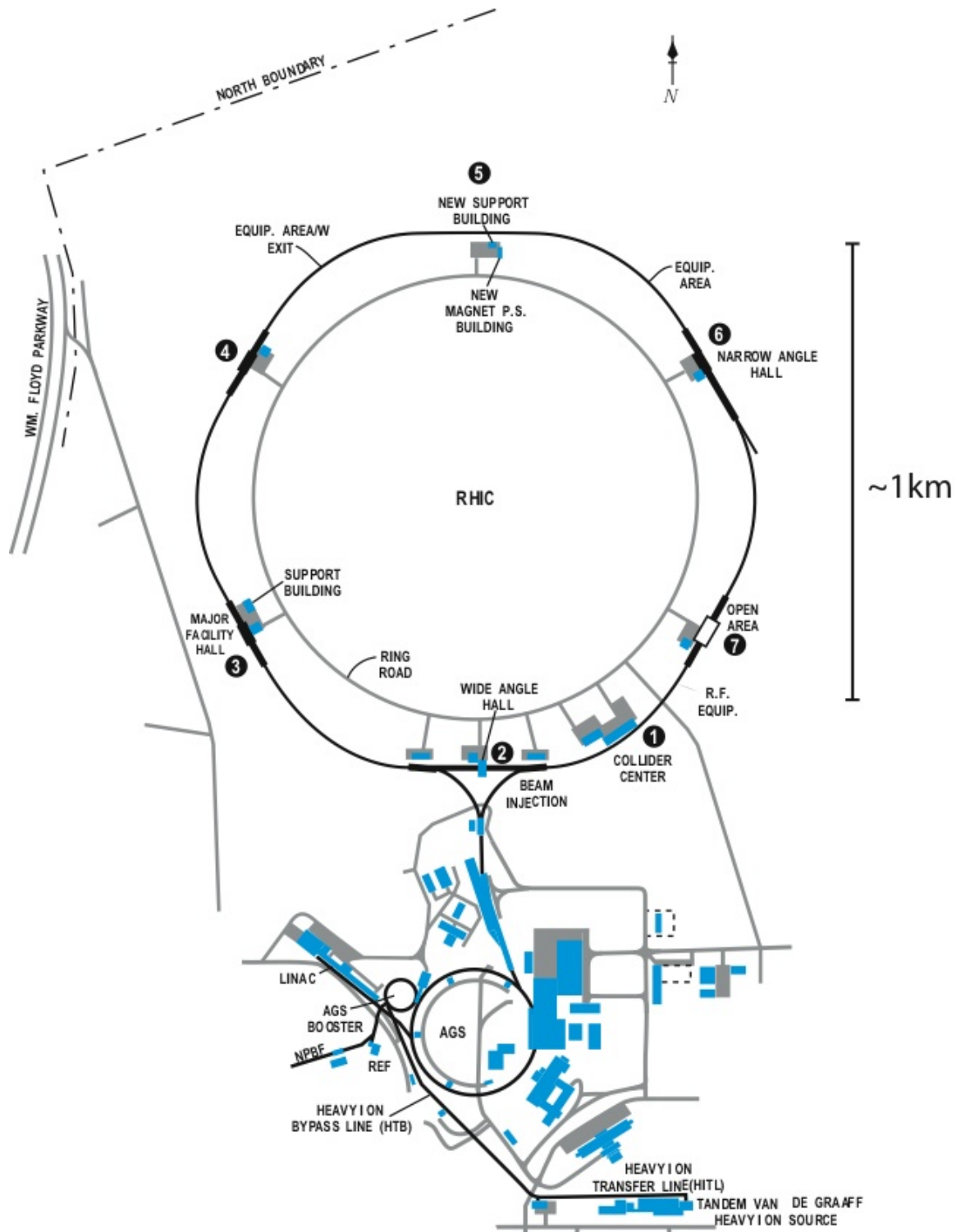


Figure 2.4. Facilities of the RHIC complex. Considering the RHIC rings as the face of a clock, the STAR experiment is located at the six o'clock position.

Table 2.1. Summary of RHIC runs.

Year	Run	Species	$\sqrt{s_{NN}}$ [GeV]
2000	I	Au+Au	130
2001	II	Au+Au	19.6, 200
		p+p	200
2002	III	d+Au	200
		p+p	200
2003	IV	Au+Au	200
		p+p	200
2004	V	Cu+Cu	22.4, 62.4, 200
		p+p	200
2005	VI	p+p	200
2006	VII	Au+Au	200
2007	VIII	d+Au	200
		p+p	200
2008	IX	p+p	200
		p+p	500

the bunches are dumped into the RHIC rings, beginning with the Tandem Van de Graaff facility.

Gold ions begin from a cesium ion sputter source. Two Tandem Van de Graaff electrostatic accelerators pull the ions with an initial electric charge of -1 through a potential difference of 14 mega-Volts. They then pass through a carbon foil which strips 13 electrons off each ion. As the ions leave, they take another 182 MeV with them giving the gold ion a total of 1.0 MeV/u. Another 20 electrons are stripped, and the ions travel the ~ 850 m long Tandem to Booster tunnel to the Booster synchrotron. All but two of the remaining electrons are removed as the Booster accelerates the ions to 95 MeV/u. From there the ions are injected into the AGS⁹.

Though the AGS is employed as an injector for RHIC, it is an impressive facility

⁹Alternating Gradient Synchrotron

on its own. It is named for the way it utilizes 240 magnets in alternating gradient focusing. The gradients are alternated inward and outward in the interest of strong focusing, simultaneously focusing in the horizontal and vertical planes. Three Nobel prizes have been awarded based on work done at the AGS¹⁰.

The AGS takes ions from the Booster and accelerates them to ~ 9 GeV/u. The remaining two electrons are stripped so that the gold atoms are finally completely ionized Au^{+79} . Once the beam is at its top energy, it is guided into the ATR¹¹ transfer line. There is a switching magnet which is used to guide ion bunches down one of two RHIC beam lines. Finally, the bunches are brought to a top energy of 100 GeV/u after circulating in the RHIC rings.

The RHIC rings contain bending and focusing magnets to keep the beams circulating properly while radio frequency cavities kick the beams up to the desired energy. The bending magnets are superconducting electromagnets cryogenically cooled to less than 5 K, with a maximum field of ~ 4 T. In total, there are six sections that make up the rings and six crossing points where collisions could occur.

At each crossing point in the RHIC rings, kicker magnets are employed as shown in Figure 2.5. The beams are steered out of the two main rings into a common beam pipe with the DX magnets which operate at 4.3 T. They are situated on either side of the interaction region so that the beams can be diverted both into and out of the common beam pipe. At STAR, the center 1.5 m section of the beam pipe is beryllium

¹⁰In 1976, Samuel Ting won the Nobel Prize for his discovery of the J particle which he shared with a group at the Stanford Linear Accelerator for discovering the same particle they named ψ . It subsequently became the J/ψ particle. In 1980, Cronin and Fitch won for experimentally verifying CP violation. In 1988, Lederman, Schwartz, and Steinberger won for their discovery of the muon-neutrino.

¹¹AGS to RHIC

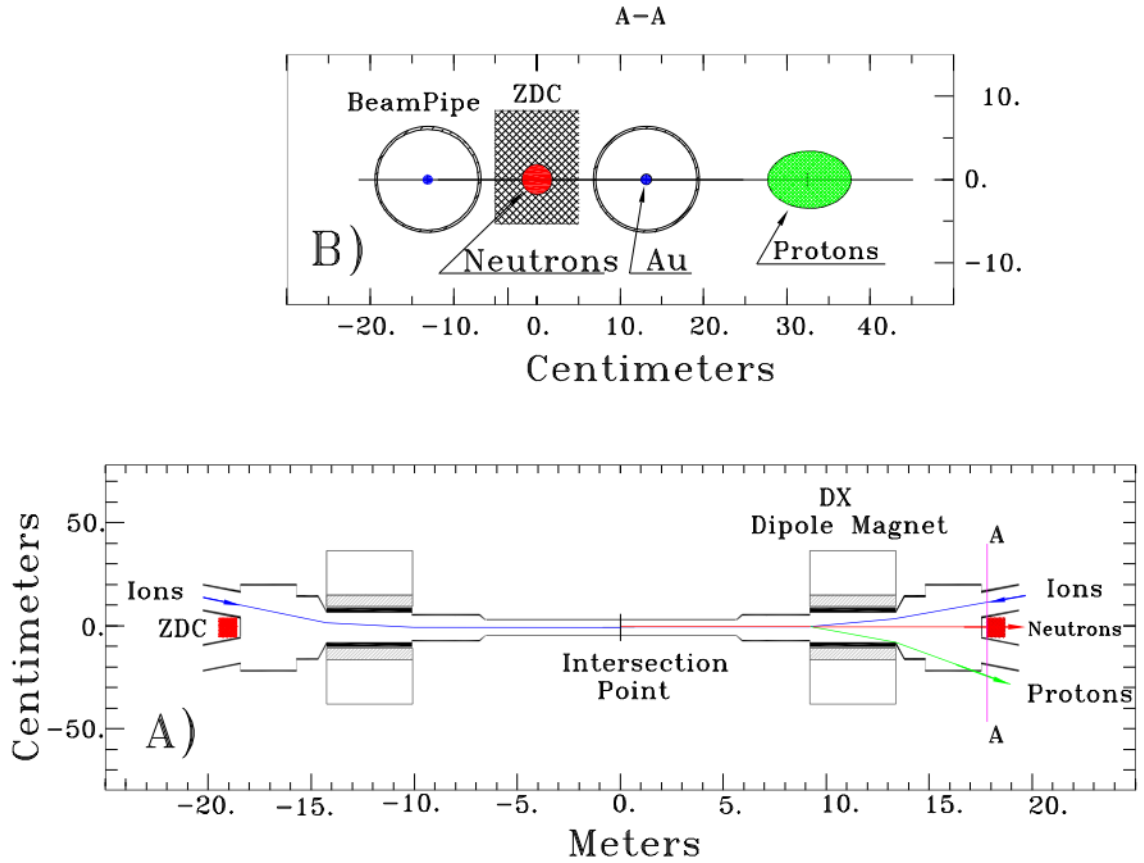


Figure 2.5. The ZDC layout as shown in [10].

to reduce multiple scattering.

As shown in Table 1.1, RHIC has been run in Au+Au, p+p, Cu+Cu, and d+Au configurations. The choice of d+Au instead of p+Au is because the charge to mass ratio, in conjunction with the magnetic field, dictates the radius of curvature of the beam path. Trying to use the same magnetic field for gold and protons would not work because the radius of curvature is too small for the protons with the magnetic field for the gold ions. The charge to mass ratio for deuterium is such that the same magnetic field can be used in the kicker magnets to steer both deuterium and gold

into and out of the same beam pipe.

2.2 The STAR Detector

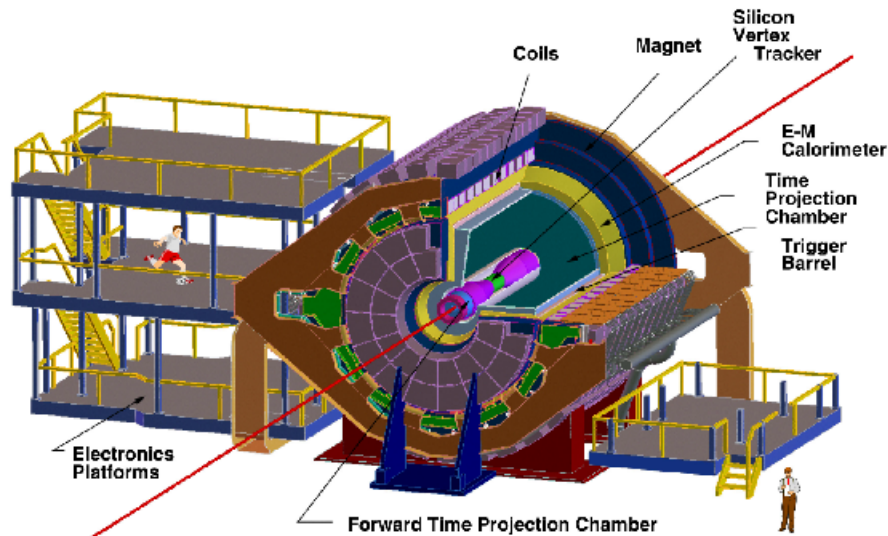


Figure 2.6. An end view of the STAR detector [33]. Figures are drawn in the picture for scale. The STAR detector is 1200 tons and the size of a house. The magnet and various components are highlighted. A red line is included to indicate the collision axis.

Two main research goals drove the design of STAR [29]. The first was to examine the behavior of the matter produced at very large energy densities in heavy ion collisions. The other related goal was to search for signatures of the QGP. These goals led to the design of a collection of detectors featuring high precision tracking over a large solid angle.

To examine the behavior of the strongly-interacting matter created in heavy ion collisions requires measurements of global event observables like the reaction plane,

centrality, and mean energy. Thus, the components of the STAR detector are arranged cylindrically, as shown in Figure 2.6, to provide a large acceptance ($0 \leq \varphi \leq 2\pi$ and $|\eta| < 3.8$).

2.2.1 Time Projection Chamber

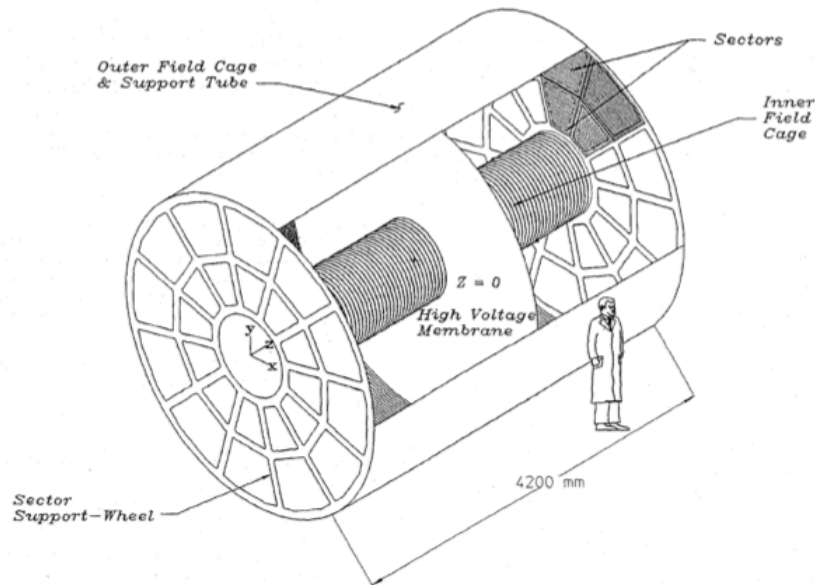


Figure 2.7. Schematic view of the STAR Time Projection Chamber [31]. Person is drawn in the picture for scale.

Of the collection of detector components that STAR employs, the Time Projection Chamber (TPC), is probably the most important. As the primary tracking detector, it is tasked with reconstructing events which produce thousands of tracks.

The TPC is a type of drift chamber outfitted with readout detectors on either side of its cylindrical drift volume as shown in Figure 2.7. The chamber is 4.2 m in length and 4 m in diameter with 50 m^3 of volume.

The cylindrical volume is filled with P10 drift gas which is a nonflammable mixture of 10% CH_4 (Methane) mixed in Ar (Argon). The gas pressure is kept about 2 mbar above atmospheric pressure in an effort to avoid air leaking into the drift volume. This is important as oxygen is an electron-attaching contaminant and subsequently a source of ionization charge loss. Another important feature of P10 gas is that it satisfies the requirement that a reasonably constant drift velocity can be maintained for small variations in conditions like pressure and electric field, as shown in Figure 2.8, from Ref. [32].

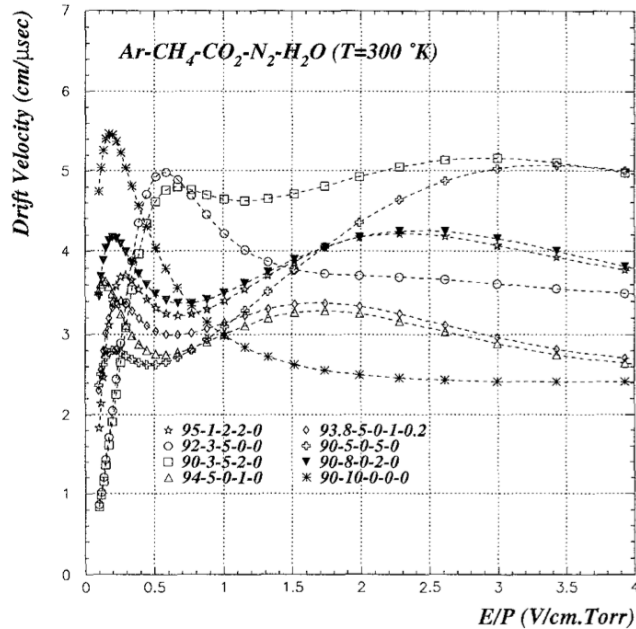


Figure 2.8. Electron drift velocity curves for different mixtures of gases as a function of E/P . The curve indicated with asterisks is for P10 gas [32].

The drift gas is a key factor in the function of a TPC. As charged particles traverse the gas, argon atoms are ionized in collisions with the charged particles. The ionization electrons then drift under the influence of a uniform electric field to

the end caps where the position in the r - ϕ plane is recorded, as is the mean drift time. The z position is determined by the mean drift time of the ionized electrons and drift velocity of the gas. The methane atoms serve to keep the drift velocity of the gas relatively constant. As an ionization electron accelerates in the electric field toward the endcaps, it collides inelastically with the methane atoms, dissipating energy by exciting vibrational and rotational modes, and subsequently keeping a relatively constant drift velocity of $5.6 \text{ cm}/\mu\text{s}$.

The drift chamber is divided into two halves by a high voltage membrane made of carbon loaded Kapton $70 \mu\text{m}$ thick [31]. The membrane is tightly stretched flat over a hoop and attached to an outer field cage. There is an inner field cage beginning radially at 0.5 m from the beam and an outer field cage ending at 2 m . As shown in Figure 2.9, the field cages are constructed from Nomex honeycomb sandwiched between two sheets of aluminum-coated Kapton [33]. The materials were chosen to maximize the strength of the construction while using the least amount of mass possible. The field cages are very important as they define the uniform electric field of STAR which is parallel to the beam direction (z -axis). For safety reasons, the central membrane carries a potential of -31 kV and decreases through a resistor chain attached to a series of equipotential rings etched on both field cages to 0 Volts on the ground wires which reside at each end of the TPC drift volume.

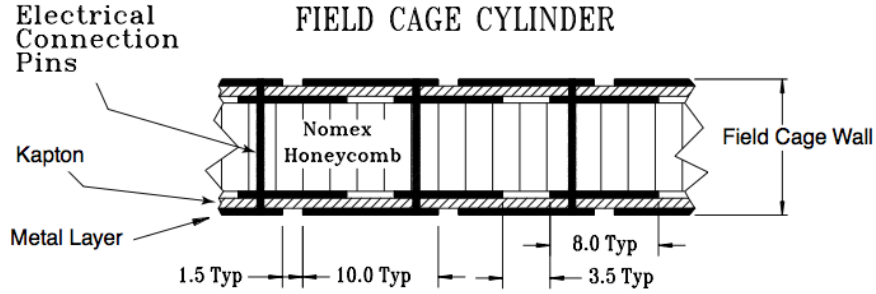


Figure 2.9. Typical cross section for the inner field cage (numbers indicate dimensions in mm) [33]. The main difference between the inner and outer field cages is a thicker layer of Nomex honeycomb and a thinner layer of aluminum in the inner field cage.

Multi-Wire Proportional Chamber

Though STAR's endcap readout design closely matches previous designs of TPC experiments from PEP4 to NA49, it does have modifications for the sake of improving reliability and simplifying construction as well as accommodating a high track density [33]. One notable design feature is the segmentation of the MWPC¹² chambers into twelve reasonably-sized modular sectors at each end of the TPC for a total of 24 sectors. Although the modular design is non-hermetic, it is a reasonable compromise considering the needs of STAR.

A readout pad plane and three wire planes constitute the MWPC sectors which reside at each endcap. The construction is shown in Figure 2.10. The overall purpose of the MWPCs is to provide noiseless gas amplification of the ionization signal to allow the measurement of the location and arrival times of the secondary electrons created as charged particles traverse the drift gas in the TPC drift chamber. Each

¹²Multi-Wire Proportional Counter

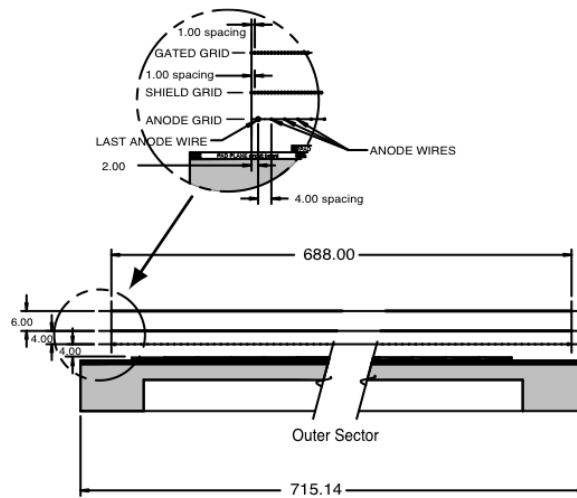


Figure 2.10. A cut away view of an outer subsector pad plane. The cut is taken along a radial line from the center of the TPC to the outer field cage so that the center of the detector is to the right. The figure shows the spacing of the anode wires relative to the pad plane, the ground shield grid, and the gated grid. The bubble diagram shows additional detail about the wire spacing. The inner subsector pad plane has the same layout except the spacing around the anode plane is 2 mm instead of the 4 mm shown here. All dimensions are in mm.[33]

wire plane is tasked with a different purpose. The first plane is a gating grid. It has two main functions. First, it keeps electrons from getting into the MWPC volume when an event is not being recorded. In addition, after an event has been recorded, it keeps positive ions from leaving the MWPC region to prevent distortion of the uniform drift field in the TPC. The last two planes, the anode and ground grids, work together to amplify the signal from the ionization charge clouds.

As shown in Figures 2.10 and 2.11, the anode grid sits closest to the pad plane. It is a series of wires $20\ \mu\text{m}$ in diameter spaced $2\ \mu\text{m}$ apart above the inner subsector pad plane and $4\ \mu\text{m}$ apart above the outer subsector pad plane [33]. Though an anode wire plane is typical of TPC designs, one aspect unique to STAR is that the anode wire grid is standalone. It has no intervening field wires. Rather than use field wires, the high tension anode wires are operated at a higher voltage to compensate. Subsequently, the MWPC chambers can function at a lower gas gain since this design affords the advantage that the readout pads can collect more of the total avalanche signal.

The anode wires are oriented approximately perpendicularly to tracks with the highest transverse momentum which are basically directed radially outward from the interaction point. Since position resolution is best along the direction of the anode wire, the strategy is to optimize the transverse momentum measurement of the highest momentum tracks.

The ground grid wires are $75\ \mu\text{m}$ in diameter with a wire-to-wire separation of 1 mm. The main purposes of the ground grid are to define the end of the drift region and to define a terminus for the electric field of the anode grid in the avalanche

region. Though this is its most important feature, it also provides RF shielding for the readout pads and is pulsed to calibrate the pad electronics.

As the name would imply, the gating grid determines whether ionization can enter or exit the MWPC region. It sits 6 mm from the ground grid. It is ‘open’ when an event is being recorded. In this mode, all the wires are set to the same voltage, typically 110 V, and electrons can drift past the wires. At all other times, it operates in a ‘closed’ mode. The wires are set to alternate above and below the nominal voltage, ± 75 V. When the gate is in its closed mode, the drift electric field terminates on the gating grid wires, so that ionization electrons cannot pass. When trigger conditions are met and it is opened, electrons pass through to the amplification region near the the anode wires. The strong $1/r$ field around the anode wires accelerates the electrons such that they gain sufficient energy between collisions to ionize the gas molecules in each successive collision, creating an avalanche of even more electrons to be collected on the anode wires. Ions created in the avalanche induce an image charge on the readout pads underneath them which collect the signal. The gas gain is ~ 1100 in the outer sectors and ~ 3000 in the inner sectors (a higher gain is needed in the inner sectors because they have smaller readout pads). These values are chosen to maintain a signal-to-noise ratio of 20:1 for a minimum ionizing particle. This gain is large enough that the signal from adjacent pads can also be used, allowing position determination through Gaussian fitting. This ensures that the signal represents the energy loss dE/dx .

The pad dimensions were constrained to optimize the probability that a hit be shared over three pads. This way a gaussian fit can be performed and the signal

extracted accurately. Moreover, on the inner sectors there are fewer pads spaced farther apart to compensate for the higher hit density.

As previously mentioned, ions created in the gas amplification process induce image charges on the readout pads. The readout pads digitize this signal which is sampled and stored. For a drift distance of 210 cm, from the center of the TPC to the MWPCs, the transverse and longitudinal diffusion lengths of an electron cloud through P10 gas are ~ 3 mm ~ 5 mm respectively [33]. Figure 2.12 shows the longitudinal and transverse position resolution in Au+Au collisions for full and half field configurations.

The twelve pad plane readout sectors are arranged circularly on each end of the TPC. Each of the sectors has an inner and outer subsector as shown in Figure 2.13. There are 3942 rectangular pads (6.2 mm x 9.5 mm) on each outer sector and 1750 pads on each inner sector (2.85 mm x 11.5 mm).

Track Reconstruction and Particle Identification

A series of steps are required for event reconstruction to sort tracks out of the ionization clusters detected by the MWPCs. First, tracking detectors provide the initial raw data from clusters to be assigned to a 3D hit position. Then hits are grouped by the likelihood that they belong to a common track. The presumed tracks are next fit by a track model. The tracks that come from the interaction region are sorted from those that do not. Those that come from the interaction region are called primary tracks with reference to the primary vertex and those that do not are called

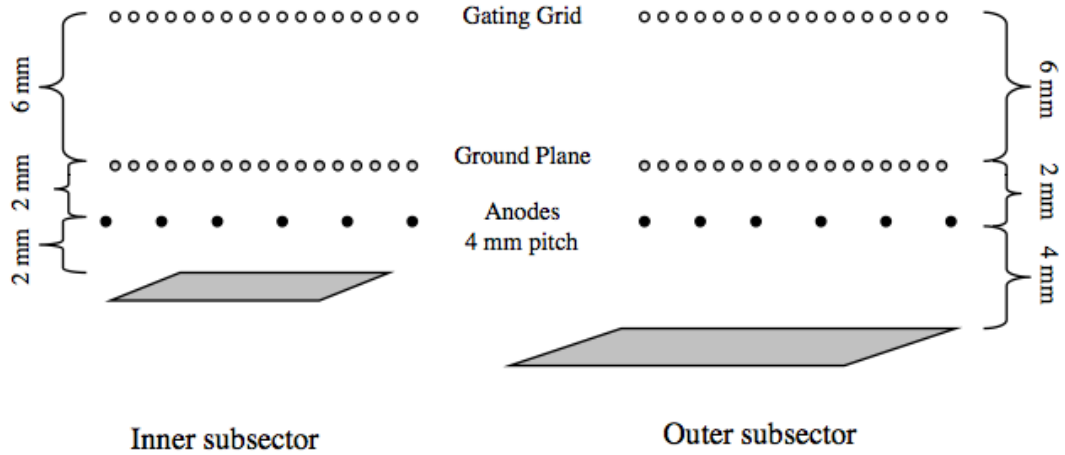


Figure 2.11. Schematic of multi-wire proportional counter chamber and pad readout subsectors [34]. Gating grid and ground plane wires are 1 mm apart. Anode wires are 4 mm apart.

secondary tracks as they are assumed to come from secondary vertices. The final step is that primary tracks are re-fit for better precision, assuming a well-constrained primary vertex.

A sophisticated software algorithm is used to complete the steps of event reconstruction. Assuming the simplest scenario of a cluster signal spread over three adjacent pads, the total ionization of the cluster is obtained by summing the charge from the pads which is then translated to energy. The r and ϕ position of the cluster is found by fitting a Gaussian to the signal spread over the three pads (the local $r\phi$ -coordinate being measured along the pad-row direction). The drift time is determined in a similar manner, fitting a Gaussian to the signal, spread over multiple time buckets. The z -coordinate is determined by multiplying the drift velocity by the drift

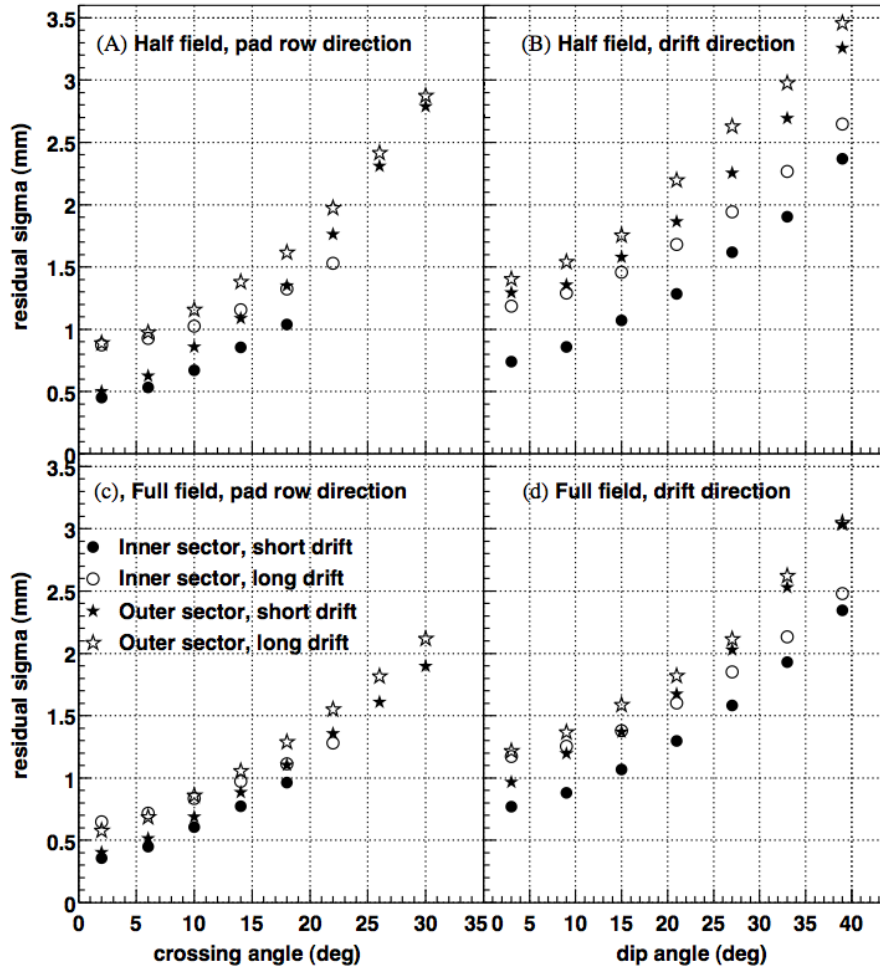


Figure 2.12. Position resolution across the transverse pad-rows and along the longitudinal z -axis of the TPC. The crossing angle is the angle between the particle momentum and the pad-row direction. The dip angle is the angle between the particle momentum and the drift direction, $\theta = \cos^{-1}(p_z/p)$ [33].

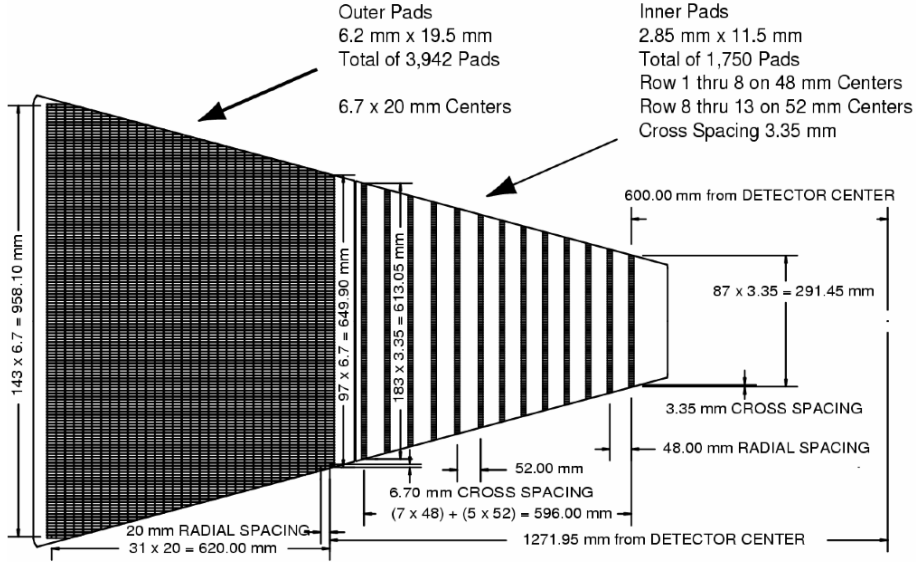


Figure 2.13. Schematic of endcap sector. The inner subsector has separated rows of narrow pads where the track density is the highest. The outer section has width and longer pads to maximize signal collection in order to get the best dE/dx measurement. The r -coordinate is defined to be the center of the pad-row and the $r - \phi$ of the hit. The z -coordinate is determined using the drift velocity in addition to the drift time from the origin of the cluster to the endcap. The accuracy of the drift velocity is ensured by regular measurements of the drift velocity with well-calibrated lasers as well as by keeping the TPC electric field at a value corresponding to the stable peak in the drift velocity curve. The local r , $r - \phi$, and z coordinates are transformed to global x , y , and z values for tracking.

With the x , y , and z coordinates of clusters determined, the tracking software makes associations between the points to form tracks. The tracks are assumed to be helical with some modifications due to energy loss and multiple Coulomb scattering.

To best approximate the modified track helices, an iterative algorithm with a

Kalman filter is employed [35]. First, permutations of the hits on the outermost three pad-rows are constructed. When the likeliest candidates are found, the algorithm moves back row-by-row adding hits within an acceptable tolerance. In this way, track segments grow row-by-row. After the possibility of track merging is investigated, with tracks defined, track fitting can occur. A track is assumed to be helical such that its $x - y$ projection is fit with a circle. A straight line is used for the projection in the $s - z$ plane (s is the path length along the helix). The results of the first order track fitting are passed through a Kalman filter to account for the effects of multiple Coulomb scattering. Once a final set of global tracks is determined for an event, the subset of global tracks which are within 3 cm of the interaction point are extrapolated to give an initial event vertex. With this initial vertex conjecture and three iterations with successively tighter track cuts, a robustly-determined primary vertex position is determined. With a primary vertex position, global tracks which have a DCA¹³ of less than 3 cm are re-fit and extrapolated through the vertex to obtain new track parameters. If the fit does not converge, it remains just a global track. Secondary tracks are determined by fitting the track points without including the primary vertex as a point.

The transverse momentum of the tracks, p_T , can be determined by fitting the $x - y$ projection of the track and its vertex with a circle. The total momentum can be calculated from the transverse momentum and the angle between the track and the beam axis.

In addition to momentum, energy loss of the particles can be measured and used

¹³Distance of Closest Approach

for some particle identification. The clusters measured by the readout pads give an indication of the energy lost by the particle that created them (dE). From this point, knowing the distance over which clusters were measured (dx), pad length modulo crossing and dip angles, which is the distance between pads where clusters are detected, gives the full dE/dx measurement. Unfortunately, because this distance is so small, the measurement is unreliable. Though the assumption that particles lose energy a few tens of eV per collision is mainly true, there are some collisions where hundreds of eV are exchanged producing so-called δ -ray electrons. This effect cannot be averaged out as the distance over which the measurement is made is too small. So, instead of the average energy loss, the most probable energy loss is obtained. This is done by removing something on the order of 30% of the highest clusters and then finding dE/dx .

2.2.2 STAR Magnet

One very important feature of STAR's design is a uniform magnetic field. The STAR magnetic field is used to bend the paths of charged particles traversing the TPC into helices. The momentum of these particles can then be measured through the radius of curvature of their paths. If the magnetic field is too large, low momentum particles bend in helices too tight to measure. By contrast, if it is not large enough, high momentum particles do not bend enough in the field to measure an accurate radius of curvature. Taking both the kinematic acceptance for low momentum particles and the momentum resolution for high momentum particles into account, a

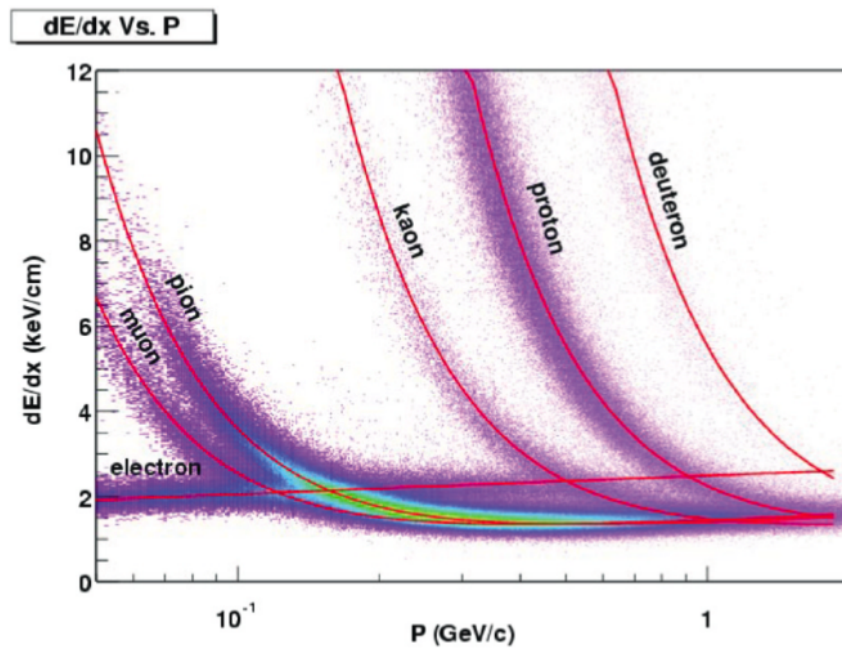


Figure 2.14. The energy loss distribution for primary and secondary particles in the STAR TPC as a function of the p_T of the primary particle. The magnetic field was 0.25 T [33].

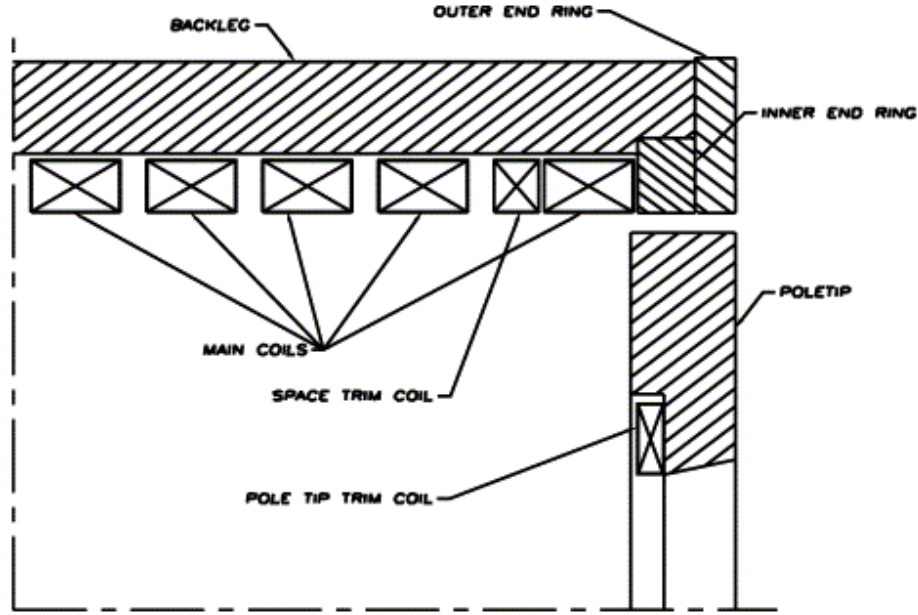


Figure 2.15. A cross-section drawing of the magnet steel [30]. The magnet steel serves as the return yolk for the magnetic field as well as the support structure for STAR.

room temperature solenoidal magnet was designed.

At full field, the STAR magnet provides a 0.5 T magnetic field. The direction of the field is parallel to the central cylindrical axis of STAR (B_z). The magnet can also be run in half-field (0.25 T) and reversed-field configurations.

As the magnetic field is crucial to determining the momentum of particles traversing the TPC, it was important to understand irregularities in the field. Before the installation of the TPC, the field was mapped for all permutations of full, half, forward, and reversed field configurations. Upper bounds on field distortions are expressed by the field integral relations:

$$|\mathfrak{S}_r| \equiv \left| \int_{z'}^z (B_r/B_{z'}) dz' \right| \leq 7.0 \text{ mm} \quad (2.3)$$

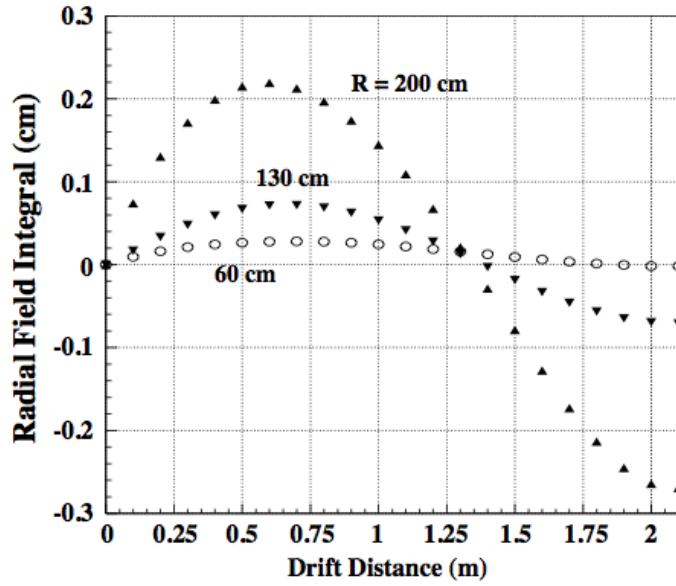


Figure 2.16. The radial field integral plotted for three different radii in the drift volume at $\phi = 0^\circ$ and $z < 0$. [30].

$$|\mathfrak{S}_\phi| \equiv \left| \int_{z'}^z (B_\phi/B_{z'}) dz' \right| \leq 2.5 \text{ mm} \quad (2.4)$$

As shown in Figure 2.16, after mapping, the maximum variation of the radial field integral, \mathfrak{S}_r , was less than 0.30 cm. The maximum variation of the azimuthal field integral, \mathfrak{S}_ϕ , was found to be less than 0.035 cm. These ranges are well within the homogeneity specifications in equations 2.3 and 2.4.

2.3 Trigger Detectors

Triggering is a fundamental step in the process of data collection. It has to do with the decision of whether an event in your detector is interesting and subsequently vetoed or kept for recording and later analysis. The data used in this thesis relied on

two trigger detector systems, the two ZDCs¹⁴ and the CTB¹⁵, for event selection.

Central Trigger Barrel

The CTB is built from 240 plastic scintillating tiles set around the circumference of the TPC. The purpose of the CTB is to measure charged particle multiplicity. It is meant to be a fast (~ 260 ns) detector operating within the $1.5 \mu\text{s}$ Level 0 trigger window allotted for the decision of whether or not to record an event.

The setup of the CTB is illustrated in Figure 2.17. The CTB barrel consists of 4 m long aluminum trays which each hold two radiators, two light guides, and two PMTs¹⁶. It provides full azimuthal coverage and pseudorapidity coverage of $|\eta| < 1$. When a collision occurs, charged particles interact electromagnetically with the scintillator tiles to produce light which is collected by a PMT. The number of charged particles crossing a given slat can then be deduced from the PMT signal.

Zero Degree Calorimeters

The most basic triggering scheme in a collider experiment is to determine whether or not a collision has occurred. This is referred to as a minimum bias trigger. The ZDC detectors are used, two per RHIC experiment, to help collect minbias triggers. They are hadronic calorimeters which reside 18 m upstream and downstream from an interaction point. They are situated at 0° with respect to the beam axis, subtending an angle of 2.5 mrad. The purpose of positioning hadronic calorimeters this way is

¹⁴Zero Degree Calorimeters

¹⁵Central Trigger Barrel

¹⁶Photomultiplier Tubes

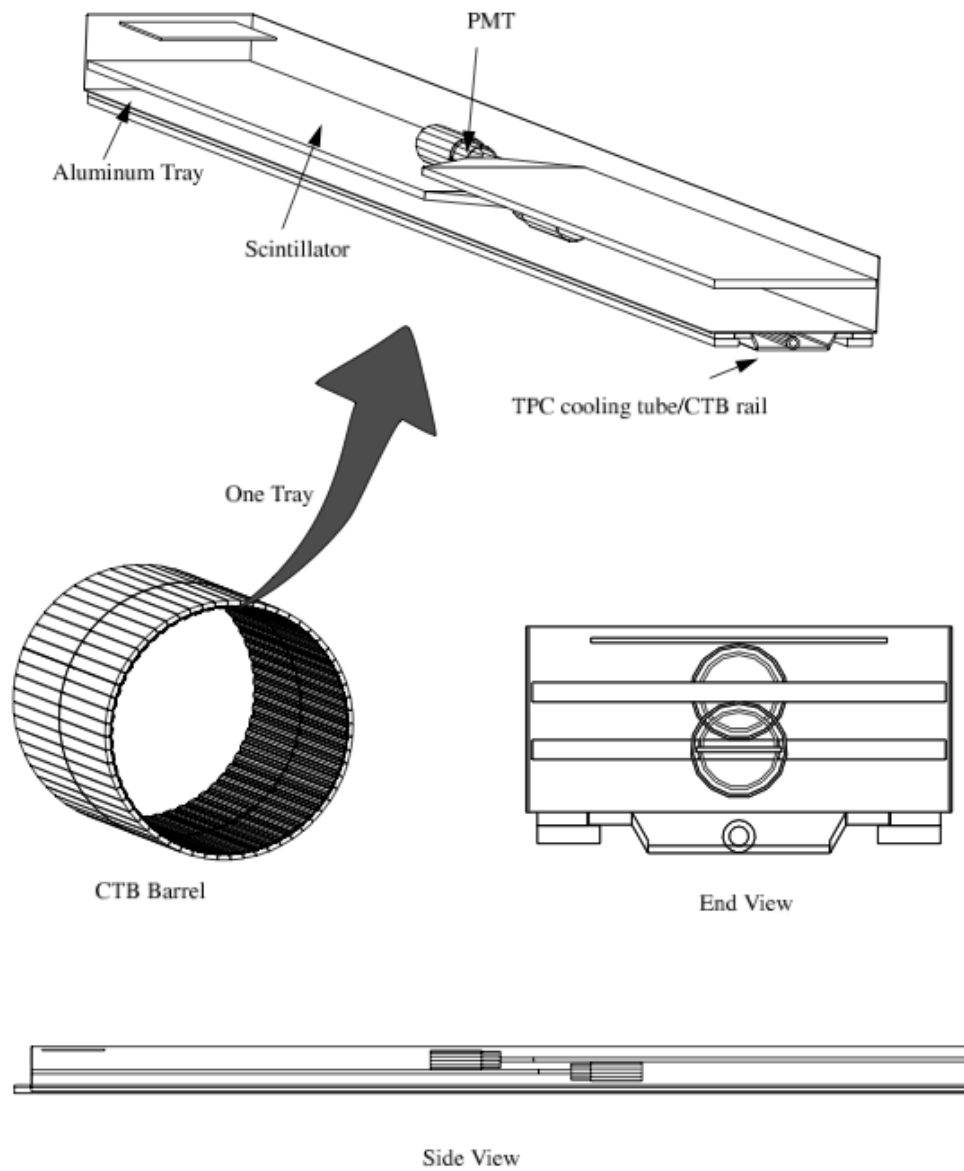


Figure 2.17. The CTB barrel is a series of scintillator tiles that sit in aluminum trays around the circumference of the TPC. Each tray holds two radiators, two light guides, and two PMTs.[49]

to collect neutrons from the inelastic collisions of nuclei. Any charged fragments are swept away by the DX magnets, as shown in Figure 2.5, while spectator neutrons continue on with nearly all of their original beam momentum.

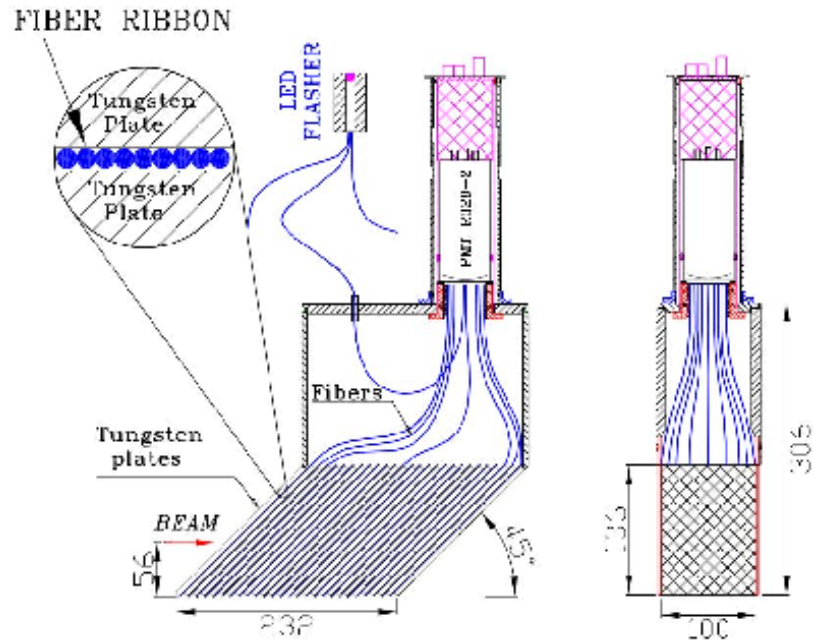


Figure 2.18. Close up of ZDC construction.

The ZDCs are constructed with tungsten plates and Cherenkov fibers as shown in Figure 2.18. Since tungsten is a high density material, it is used to initiate particle showers. The Cherenkov fibers sample the energy of the showers. Light in the fibers is relayed to three photomultiplier tubes which generate the signal from the ZDC. STAR uses a hadronic minimum bias trigger in Au + Au collisions which requires a signal in each ZDC equivalent to at least 40% of a neutron, as well as a “Blue Yellow sync”, verification that each ring has a bunch crossing at the same time at the interaction point, and a minimum multiplicity in the CTB. A minimum bias

trigger for UPCs¹⁷ was implemented with the same requirements but for a smaller occupancy in the CTB.

¹⁷Ultra Peripheral Collisions

Chapter 3

Interference in ρ^0 Photoproduction

3.1 Introduction

Though a primary goal of studying heavy ion collisions is to quantify the matter produced in hadronic collisions, events where the two nuclei “miss” (i.e. there is no hadronic collision) also yield interesting physics. In these *ultraperipheral collisions*, or UPCs, electromagnetic interactions dominate since the electromagnetic force is long range as opposed to the limited range of the strong force. We have considered two main channels for studying the electromagnetic interaction: photoproduction and photoproduction with mutual Coulomb excitation of the spectator nuclei. Photoproduction consists of a photon from one nucleus interacting with a quark or gluon from the opposite nucleus. In two-photon processes, photons from each nucleus mutually interact.

There are two kinds of photoproduction: direct and resolved. In direct photoproduction, a photon and parton from each of the participating nuclei fuse. In Figure

3.1 the Feynman diagram labeled (a) shows photon-gluon fusion resulting in heavy quark ($Q\bar{Q}$) production, though light quarks can result from the reaction as well. One reason this process of interest is that it provides a direct method of probing the nuclear gluon distribution.

As opposed to direct photoproduction, resolved photoproduction occurs when a photon fluctuates to $q\bar{q}$ pairs and gluons of zero flavor and zero baryon number. A $q\bar{q}$ pair or gluon from the original photon then interacts with a parton of the opposite nucleus [50]. Figure 3.1 parts (b)-(d) show Feynman diagrams for resolved production. The direct and resolved components make up the total photoproduction cross section.

In heavy ion collisions, processes involving photons have a large cross section since fast-moving ions carry large electric fields with them. The Weiszacker-Williams method can be used to calculate the photon flux [51]:

$$\frac{d^3 N}{dkd^2 b} = \frac{Z^2 \alpha \omega^2}{\pi^2 k b^2} [K_1^2(\omega) + \frac{1}{\gamma_L^2} K_0^2(\omega)] \quad (3.1)$$

The flux is calculated with respect to a distance b from the nucleus with k as photon energy, γ_L as the Lorentz boost in the cm frame, $K_0(\omega)$, $K_1(\omega)$ are modified Bessel functions and $\omega = \frac{kb}{\gamma_L}$. As the flux is directly proportional to the charge squared (Z^2), it can immediately be seen that heavy ions (like gold, $Z = 79$) have large photon fields associated with them.

One focus of the analysis presented in this thesis is ρ^0 photoproduction in ultra-peripheral collisions. The ρ^0 is a vector meson, which means it has negative parity and a spin of 1. It has a mass of 768.5 ± 1.1 MeV and a width of 150.7 ± 2.9 MeV [40]. Its main decay channel is to a $\pi^+\pi^-$ pair with a branching ratio of nearly 100%.

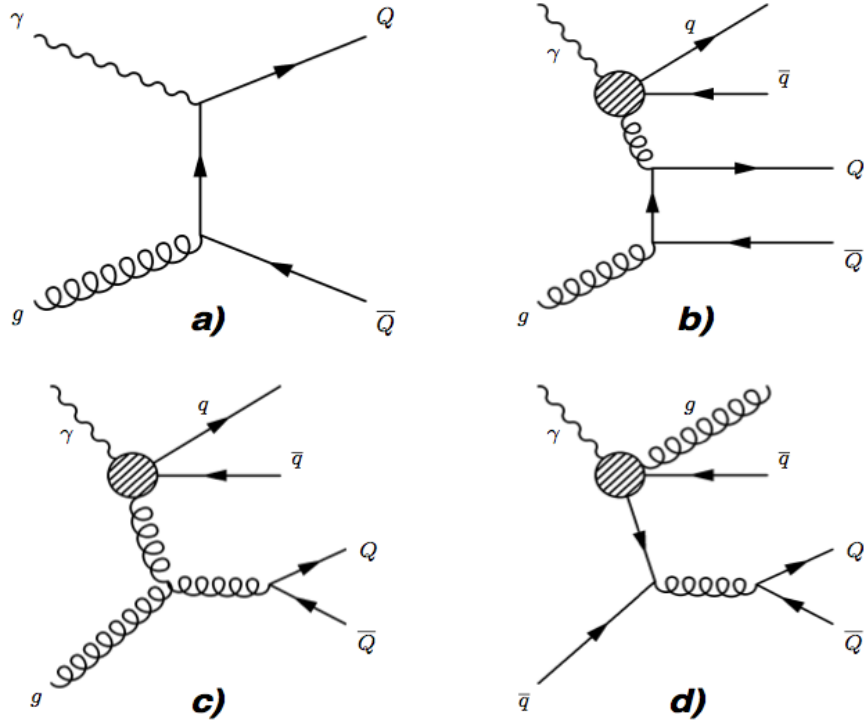


Figure 3.1. Feynman diagrams for heavy quark photoproduction from (a) direct and (b)-(d) resolved photons [51].

The photoproduction of ρ^0 mesons has been studied extensively. Measurements have been made at fixed-target experiments with relatively low energies for over thirty years [39, 41, 43, 44]. More recently, the STAR collaboration has made measurements of ρ^0 photoproduction [45, 46] in addition to the PHENIX collaboration's J/ψ photoproduction measurements [47].

In this analysis, there are two main production channels for the ρ^0 . They are shown in Figure 3.2. The left-hand side of the figure shows a virtual photon from one gold nucleus scattering off a Pomeron in the other nucleus. The right-hand side of the diagram shows the same process with the further exchange of photons leading to Coulomb excitation and neutron emission from each nucleus. The exchange of the

three (or more) photons actually occurs as three (or more) independent processes.

The ρ^0 is photoproduced by a resolved process. A photon from one nucleus fluctuates to a $q\bar{q}$ pair and scatters from the opposite nucleus. The ρ^0 results from this scattering, attributed to Pomeron exchange [52]. Moreover, the Pomeron dictates where the ρ^0 is produced. The production occurs within 1 fm of the “target” nucleus¹ because the range of the strong force is short compared to the range of the electromagnetic field of the photon. First suggested in 1961, the Pomeron was conceived a particle exchanged in a strong interaction, explaining particle production in high energy hadron-hadron reactions [53]. It is colorless and has the same quantum numbers as the vacuum.

3.1.1 Coherent and Incoherent ρ^0 Photoproduction in Ultra-Peripheral Au+Au Collisions

There are cross sections for both coherent and incoherent ρ^0 production. When the transverse momentum of the photon is small, $p_T < \hbar/R_A$, the subsequent $q\bar{q}$ pair couples to the entire nucleus and the resulting ρ^0 is coherently produced. At large transverse momentum, when the $q\bar{q}$ couples to an individual nucleon, it is incoherently produced. Coherent vector meson production has a cross section equivalent to about 8-10% of the total hadronic cross section for Au+Au collisions at $\sqrt{s_{NN}} = 200$ GeV [37, 46, 45, 69, 70].

Coherent and incoherent cross sections have been measured by STAR in Au+Au collisions at $\sqrt{s_{NN}} = 200$ GeV, as shown in Figure 3.3. Table 3.1 gives the measured

¹the one which contributes the Pomeron to the interaction

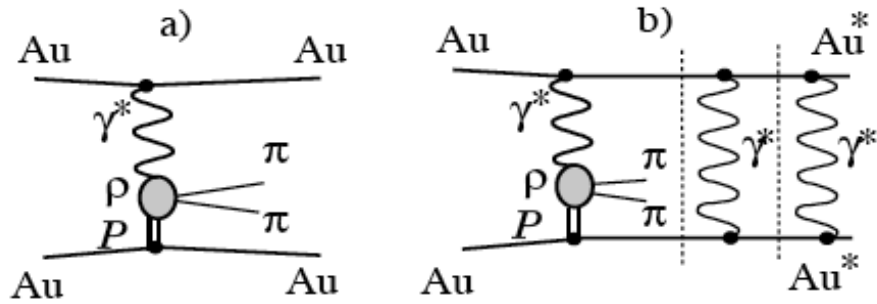


Figure 3.2. There are two photoproduction channels for the ρ^0 in this study. In the diagram on the left, a virtual photon from the top gold nucleus fluctuates to a quark-antiquark pair and scatters off a Pomeron in the bottom nucleus to subsequently produce a ρ^0 . In the diagram on the right, the same process occurs as well as the exchange of additional photons which induce mutual Coulomb excitation and subsequent emission of neutrons from each nucleus. The exchange of the three (or more) photons actually occurs as three (or more) independent processes.

cross sections for coherent and incoherent ρ^0 photoproduction with and without nuclear excitation.

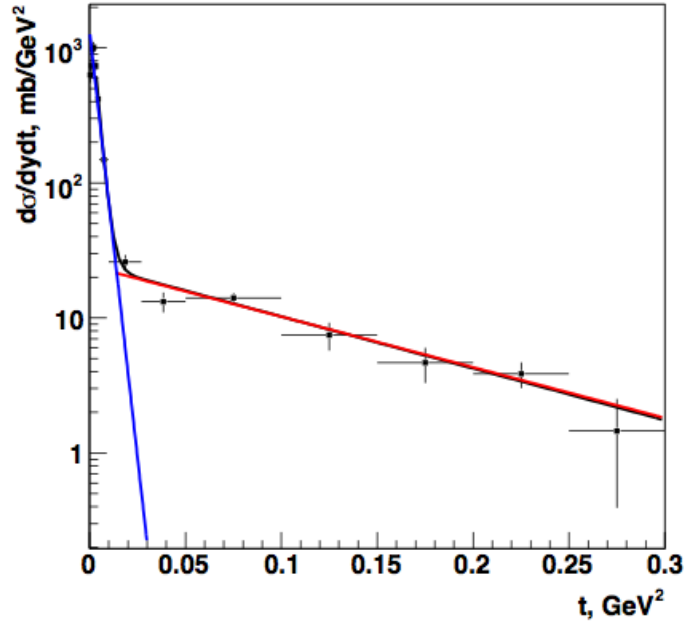


Figure 3.3. ρ^0 production cross section as a function of t . The lines indicate a fit to two exponentials corresponding to the coherent and incoherent cross sections at low and high t respectively [45].

3.1.2 Interference in ρ^0 Photoproduction in Ultra-Peripheral Heavy Ion Collisions

In an effect akin to double-slit interference, there is interference in the ρ^0 photoproduction cross section in ultraperipheral $A+A$ collisions. Since either nucleus can be the source of the photon which scatters to produce a ρ^0 , the two possibilities for production are quantum-mechanically indistinguishable. Subsequently the wave func-

Parameter	STAR at	STAR at	STAR at
	$\sqrt{s_{NN}} = 200$ GeV	$\sqrt{s_{NN}} = 200$ GeV	$\sqrt{s_{NN}} = 130$ GeV
	coherent	coherent + incoherent	coherent
$\sigma_{XnXn}^{\rho^0}$ (mb)	$31.9 \pm 1.5 \pm 4.8$	$41.4 \pm 2.9 \pm 5.1$	$28.3 \pm 2.0 \pm 6.3$
$\sigma_{0nXn}^{\rho^0}$ (mb)	$105 \pm 5 \pm 16$	$145 \pm 7 \pm 28$	$95 \pm 60 \pm 25$
$\sigma_{1n1n}^{\rho^0}$ (mb)	$2.4 \pm 0.2 \pm 0.2$	$2.8 \pm 0.3 \pm 0.2$	$2.8 \pm 0.5 \pm 0.7$
$\sigma_{0n0n}^{\rho^0}$ (mb)	$380 \pm 18 \pm 58$	$494 \pm 23 \pm 59$	$370 \pm 170 \pm 80$
$\sigma_{\text{total}}^{\rho^0}$ (mb)	$517 \pm 19 \pm 108$	$680 \pm 24 \pm 144$	$460 \pm 220 \pm 110$

Table 3.1. Coherent ρ^0 production cross section measured by STAR at $\sqrt{s_{NN}} = 200$ GeV accompanied by nuclear breakup and without breakup compared with previous STAR measurements at $\sqrt{s_{NN}} = 130$ GeV [46].

tions for the decay products intertwine, leading to an interference pattern in the ρ^0 emission distribution which is most clearly seen as a suppression of the cross section at low momentum [36].

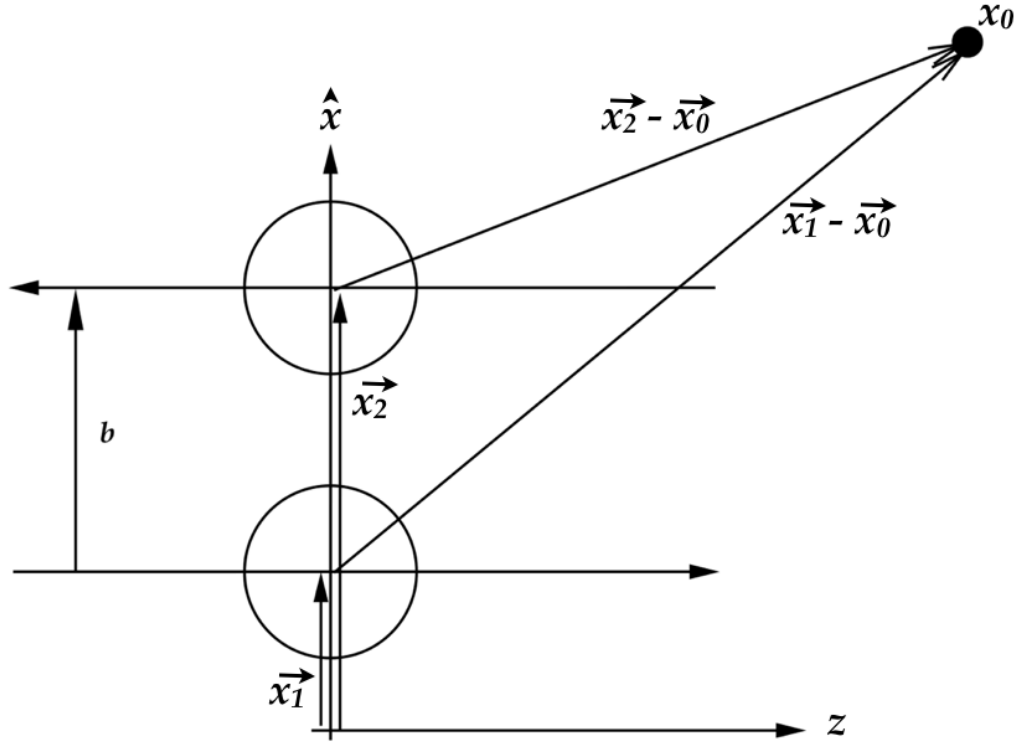
Representing the ρ^0 s as plane waves and taking two nuclei at points \vec{x}_1 and \vec{x}_2 , the amplitude A_0 for observing a vector meson at point x_0 is [36]:

$$A_0(x_0, \vec{p}, b) = A(p_T, y, b)e^{i[\phi(y) + \vec{p} \cdot (\vec{x}_1 - \vec{x}_0)]} - A(p_T, -y, b)e^{i[\phi(-y) + \vec{p} \cdot (\vec{x}_2 - \vec{x}_0)]} \quad (3.2)$$

where \vec{p} (p_T), is the momentum (transverse momentum) of the ρ^0 , b is the impact parameter between the two nuclei, and $\phi(y)$ is an empirically determined phase factor. Because the ρ^0 meson has negative parity, the amplitudes for the outgoing waves subtract. The cross section comes from the square of the combined amplitudes.

$$\begin{aligned} \sigma(p_T, y, b) &= A^2(p_T, y, b) + A^2(p_T, -y, b) \\ &\quad - 2A(p_T, -y, b)A(p_T, y, b) \times \cos[(\phi(y) - \phi(-y) + \vec{p} \cdot \vec{b})] \end{aligned}$$

Away from midrapidity, $A(p_T, b, y) \neq A(b, -y)$ and the interference effect is diminished.

Figure 3.4. Diagram for ρ^0 production from Equation 3.2.

At midrapidity, the cross section simplifies:

$$\sigma(p_T, y = 0, b) = 2A^2(p_T, y = 0, b)(1 - \cos[\vec{p} \cdot \vec{b}]) = 2A^2(1 - \cos(p_T b))$$

Thus the interference causes the cross section to go to zero at midrapidity

as $p_T \rightarrow 0$.

3.2 Experimental Measurement

3.2.1 Trigger Setup

In 2001, the data for this analysis were collected with the TPC², CTB³, and ZDC's⁴. The TPC tracked the charged pion pairs which decayed from the parent ρ^0 mesons for $|\eta| < 1$. The remaining detectors, the CTB and ZDC's, were used as trigger detectors. Approximately 4M events were collected by two trigger algorithms: the UPC topology trigger with 1.5M events and the UPC minbias trigger with 2.5M events.

Two algorithms were used to trigger on events of interest, which were candidates for coherent ρ^0 photoproduction. A UPC topology trigger collected exclusive ρ^0 events, i.e. those without nuclear Coulomb excitation. In the trigger algorithm, the CTB was utilized to detect near back-to-back $\pi^+ \pi^-$ pairs which resulted from the ρ^0 decays. The bulk of the measured ρ^0 photoproduction cross section is from coherent production, see Table 3.1 and Figure 3.3, which results in very little p_T for the ρ^0 . Therefore the daughter pions will get very little focusing and will appear nearly back-to-back in the lab frame. The 240 scintillator slats of the CTB were divided into four quadrants, as shown in Figure 3.5. The trigger required a coincidence between the North and South quadrants in time with the blue-yellow sync. The ZDCs were required to have no signals, as exclusive photoproduction does not leave the respective nuclei excited. The Top and Bottom quadrants were used as vetos for cosmic rays.

²Time Projection Chamber

³Central Trigger Barrel

⁴Zero Degree Calorimeters

The cosmic ray flux is headed downward towards the surface of the earth. Showers from cosmic rays or their products lead to energetic charged particles (mostly muons) traversing the CTB and TPC. A single muon, headed straight through the top of the detector could be reconstructed as two back-to-back tracks at midrapidity with no net charge or momentum, mimicking a ρ^0 decaying at rest in the detector (see Figure 3.5). The Top/Bottom veto reduced this background.

The second trigger algorithm, the UPC minimum bias trigger, collected events where ρ^0 photoproduction was accompanied by mutual Coulomb nuclear excitation. The trigger required the coincidence between the East and West ZDCs (ZDC threshold set to accept one or more neutrons in each of the ZDCs), the CTB sum signal (with threshold set to accept 2 mips) and the blue-yellow sync. Figure 3.6 shows the ADC counts in the east ZDC for the UPC minbias dataset. It is overlaid with a fit incorporating the sum of four Gaussians to highlight 1,2, 3, and 4 neutron peaks from left to right, respectively. Each successive peak gets smaller as the probability for the emission of neutrons decreases with increased number of neutrons. The ratio of the number of candidates in the $1n:2n:3n:4n$ peaks is 10:5:2.2:1.6:1. The cross section for ρ^0 production accompanied by Coulomb excitation is

$$\sigma(\text{Au} + \text{Au} \rightarrow \text{Au}^* + \text{Au}^* + \rho^0) = \int d^2b \ P_{\rho^0}(b) P_{X_n X_n}(b) \quad (3.3)$$

The probability for Coulomb excitation is independent of the probability for ρ^0 production, and can be expressed as:

$$P_{\chi_{1n} \chi_{2n}}(b) = \prod_{i=1}^{\chi_1} P_{i_n}(b) \prod_{j=1}^{\chi_2} P_{j_n}(b) \quad (\text{probability for an } n \text{ neutron reaction})$$

The main mechanism for neutron emission is photon exchange between the nuclei, exciting a giant dipole resonance. To satisfy the trigger requirement, a photon is required to excite each nucleus and an additional photon is required to scatter and produce a ρ^0 .

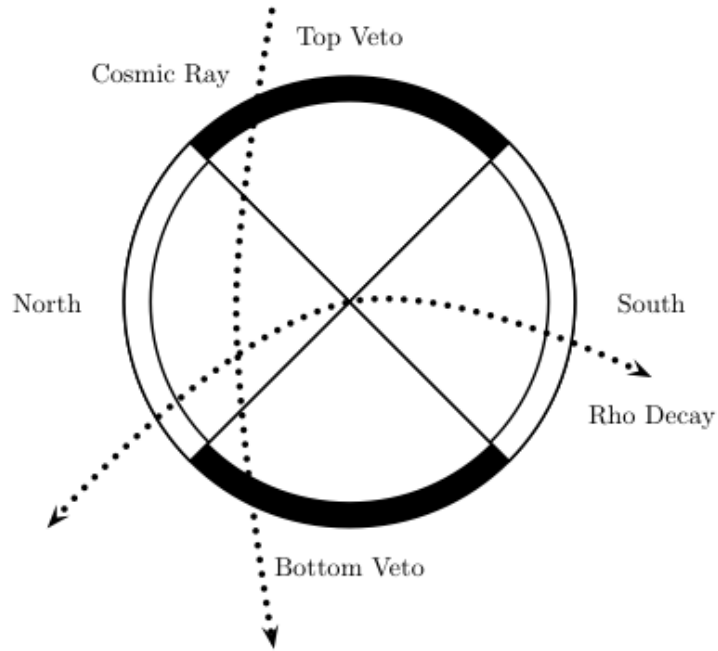


Figure 3.5. The UPC topology trigger utilized the CTB divided into four quadrants: Top, Bottom, North, and South. The quadrants were established to trigger on back-to-back $\pi^+ \pi^-$ pairs resulting from the decay of a ρ^0 . The trigger required a coincidence between North and South, with Top and Bottom as vetoes to reject most cosmic ray events.

3.2.2 Event Selection

A clean set of ρ^0 photoproduction candidates was selected from all UPC-triggered events by imposing quality cuts as shown in Table 3.2.

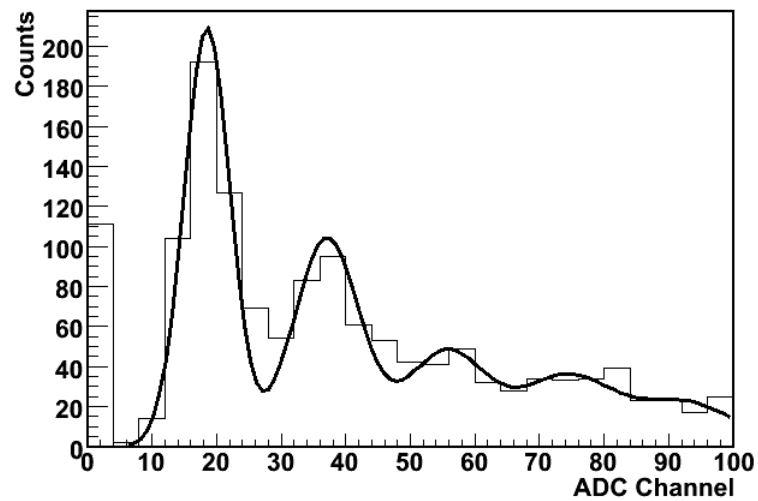


Figure 3.6. ADC signal in the east ZDC for the minbias dataset. The overlaid curve is a fit with the sum of four Gaussians. Four clear peaks from left to right show a signal for one, two, three, and four neutrons respectively. The ratio of the number of candidates in the 1n:2n:3n:4n peaks is 10:5:2.2:1.6:1.

The cut on the $zVertex$ variable is different for the two triggered data sets. This is due to the fact that there are different $zVertex$ distributions generated by each trigger. As the UPC minbias trigger relies on the ZDCs, the timing cuts on the ZDCs result in a $zVertex$ distribution with a sigma of 30 cm. As the topology trigger does not include the ZDC requirement, it has a distribution with a sigma of 80 cm because it depends on the distribution of the beam.

The rapidity cut is different for both data sets as well, due to cosmic ray contamination which is not completely eliminated by the topology trigger. Since the cosmics are reconstructed as two tracks at midrapidity, the way to cut out all contamination is to cut out all ρ^0 candidates in the topology sample with $y = 0$. In the minbias sample, the ZDC requirements, in addition to the CTB sum, eliminated cosmic ray events. This is why the lowest rapidity cut for the topology sample is 0.05 while the minbias rapidity cut is at 0. A study was done to estimate the cosmic ray contamination after all the quality cuts are applied. It was estimated that cosmic rays account for approximately 0.1% of the candidates accepted.

The purpose of selecting a clean set of ρ^0 s for both triggered datasets was to study their transverse momentum spectra, more specifically the t spectra, where t is a Mandelstam invariant, the momentum transfer to the ρ^0 . The interference effect is more pronounced as a function of t . For this study it is valid to approximate t as p_T^2 :

$$t = t_{\perp} + t_{\parallel} \simeq p_T^2 \quad (t_{\parallel} \text{ the longitudinal part of } t \text{ is negligible})$$

The data in this analysis are compared to the predictions of the STARlight Monte Carlo event generator [37]. It models the physics of photon-Pomeron [36, 37] and

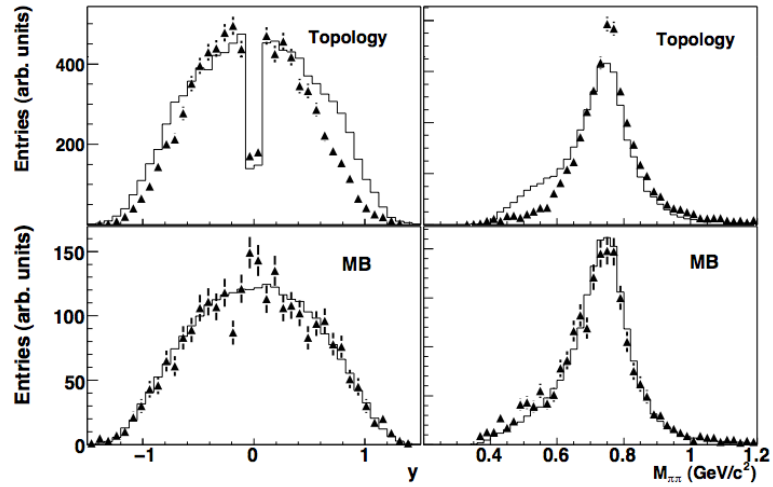


Figure 3.7. Rapidity (left) and $M_{\pi\pi}$ (right) of the $\pi^+\pi^-$ distributions for the topology (exclusive ρ^0 , **top**) and MB (Coulomb breakup, **bottom**) samples. The points with statistical error bars are the data, and the histograms are the simulations. The notch in the topology data around $y = 0$ is due to the explicit rapidity cut to remove cosmic ray backgrounds [68].

Track Variable	Cut
number of primary tracks	2
total number of tracks	2
total charge	0
p5 - occupancy of CTB (topology only)	$> 10 \ \& \neq 20$ – select between 1 and 3 mips in the CTB
zVertex	< 50 cm from center of TPC for minbias < 100 cm from center of TPC for topology
rVertex	< 8 cm from center of TPC
invariant mass (assuming the two tracks are pions)	> 0.55 GeV $\ \& \ $ < 0.92 GeV
transverse momentum (p_T)	$> 0 \ \& \ < 0.1$ GeV
rapidity (y) (UPC minbias)	(two ranges) $> 0.0 \ \& \ < 0.5 : \ > 0.5 \ \& \ < 1.0$
rapidity (y) (UPC topology)	$> 0.05 \ \& \ < 0.5 : \ > 0.5 \ \& \ < 1.0$

Table 3.2. Quality cuts for identification of ρ^0 candidates in data.

two-photon interactions [38] in peripheral collisions of heavy ions.

Some comparisons between data and Monte Carlo are shown in Figure 3.7. The topology and minbias-triggered data sets are shown on the top and bottom of Figure 3.7, respectively. The left-hand plots compare the measured ρ^0 rapidity distributions (shown as points with errors) and simulated ρ^0 's (histogram). The right-hand plots compare the measured ρ^0 invariant mass distributions (shown as points with errors) and simulated ρ^0 (histogram) production.

The comparison between the minbias data and the simulations are very good. While the data are higher than the Monte Carlo at midrapidity due to some irreducible cosmic ray contamination, the measured and simulated invariant mass distributions match very well.

The comparisons are not as good for the topology data and the Monte Carlo. In particular, for $y > 0.5$, the data fall below the Monte Carlo. The simulations overestimate the yield for $M < 0.65$ GeV. This has to do with the kinematic acceptance of the CTB. Lower mass ρ^0 's decay to pions with lower momentum. These lower p_T pions can bend in the magnetic field so much that they are no longer in opposite quadrants of the CTB. Consider Figure 3.5; lowering the momentum of the left moving pion would cause it to bend into the “Bottom quadrant”, vetoing the event.

Discrepancies between the topology data and Monte Carlo mainly have to do with the modeling of the topology trigger in the Monte Carlo. Appendix B contains plots showing various attempts to improve the simulation. The best compromise between the goodness of both the rapidity and invariant mass comparisons were kept, as shown in Figure 3.7.

Appendix C contains more plots comparing the data and the Monte Carlo for both triggered datasets for other observables. The comparisons generally look very reasonable.

3.2.3 Interference Measurement

A multi-parameter fit, as shown in Equation 3.4, is used to measure the interference effect in the data,

$$\frac{dN}{dt} = A \exp(-kt)[1 + c(R(t) - 1)], \quad (3.4)$$

where $t \sim p_T^2$, k is the exponential slope related to the nuclear radius [41], A is an arbitrary normalization factor, and c is the degree of interference where:

- $c = 1$ is the expected degree of interference,
- $c = 0$ is no interference.

Another variable in Equation 3.4 which warrants explanation is $R(t)$, the ratio of the Monte Carlo-generated dN/dt spectra with and without interference:

$$R(t) = \text{Int}(t)/\text{Noint}(t)$$

The top portion of Figure 3.9 shows the Monte Carlo predicted t -spectra with and without interference for the minbias dataset with $|y| < 0.5$. The histograms strongly deviate from each other for $t_{\perp} < 0.003 \text{ GeV}^2$. The MC spectrum without interference exhibits an exponential shape. The one with interference is a modified exponential exhibiting the effects of destructive interference at $t \sim 0$.

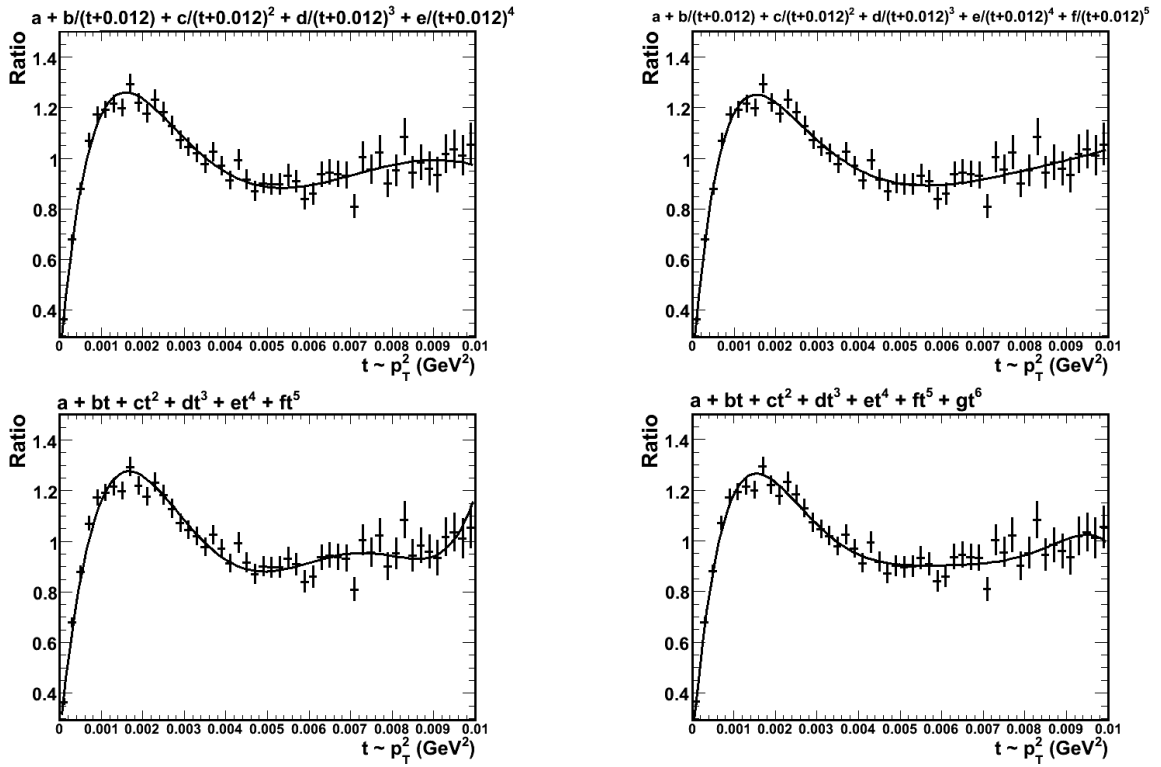
The bottom portion of Figure 3.9 shows efficiency curves for ‘interference’ (dotted histogram) and ‘no interference’ (solid histogram). The efficiency is calculated by taking the reconstructed GEANT⁵ [71] t spectrum and dividing it by the raw Monte Carlo t spectrum. The curves match well except in the first bin. One explanation for this is p_T smearing.

In order to highlight the effects of interference, we take the ratio of the MC with and without interference. The resulting ratio for the minbias data for $|y| < 0.5$ is shown in Figure 3.8. An enhancement from constructive interference is seen at ~ 0.0015 . The second destructive minimum is seen at $t \sim 0.0045$.

A fit function for this ratio, $R(t)_{\text{fit}}$, came from the comparison of multiple fit functions. Several different polynomials were tried as well as fits with different powers of $1/t$. Examples of fit functions for the minbias data with a rapidity range of $y < 0.5$ are shown in Figure 3.8. Table 3.3 gives the extracted χ^2/dof and the value of c for the overall fits, including different functions for $R(t)$. Ultimately, the function given in Equation 3.5 was chosen. It combines the fewest parameters with the best χ^2/dof . The constant in the denominator, 0.012, has no physical significance, it was chosen to optimize the fit.

$$R(t)_{\text{fit}} = a + \frac{b}{(t + 0.012)} + \frac{c}{(t + 0.012)^2} + \frac{d}{(t + 0.012)^3} + \frac{e}{(t + 0.012)^4} \quad (3.5)$$

⁵GEometry ANd Tracking

Figure 3.8. Examples of fitting functions for $R(t)$.

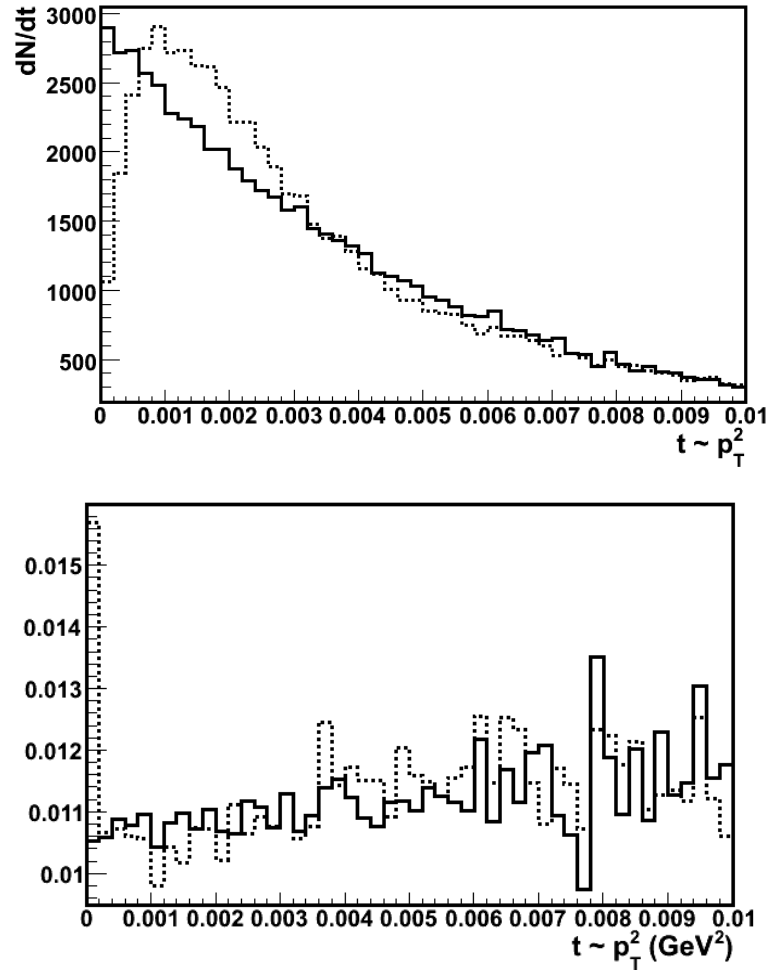


Figure 3.9. **(Top)** Monte Carlo simulated minbias $t_{\perp} \sim p_T^2$ spectra for ρ^0 sample, $|y| < 0.5$. The dotted line histogram is a simulation assuming that there is interference. The overlapping solid histogram is a simulation without interference. **(Bottom)** Efficiency histograms calculated for ‘interference’ (dotted) and ‘no interference’ (solid) cases.

Dataset/Fit	Rapidity	χ^2/dof	c
minbias / (1/t) : 5 parameters	$0 < y < 0.5$	43/47	0.92 ± 0.07
	$0.5 < y < 1.0$	75/47	0.93 ± 0.09
minbias / (1/t) : 6 parameters	$0 < y < 0.5$	45/47	0.92 ± 0.07
	$0.5 < y < 1.0$	76/47	0.92 ± 0.09
minbias / 5-degree polynomial	$0 < y < 0.5$	44/47	0.92 ± 0.07
	$0.5 < y < 1.0$	77/47	0.93 ± 0.09
minbias / 6-degree polynomial	$0 < y < 0.5$	45/47	0.91 ± 0.07
	$0.5 < y < 1.0$	75/47	0.92 ± 0.09
topology / (1/t) : 5 parameters	$0.05 < y < 0.5$	58/47	0.71 ± 0.10
	$0.5 < y < 1.0$	64/47	0.78 ± 0.18
topology / (1/t) : 6 parameters	$0.05 < y < 0.5$	53/47	0.73 ± 0.10
	$0.5 < y < 1.0$	64/47	0.77 ± 0.18
topology / 5-degree polynomial	$0.05 < y < 0.5$	57/47	0.73 ± 0.10
	$0.5 < y < 1.0$	64/47	0.79 ± 0.19
topology / 6-degree polynomial	$0.05 < y < 0.5$	55/47	0.72 ± 0.10
	$0.5 < y < 1.0$	65/47	0.75 ± 0.18

Table 3.3. Fitting Summary for different $R(t)$ fits.

3.2.4 Statistical and Systematic Errors

The results of the analysis with statistical errors are presented for both triggered data sets, UPC minbias and topology, and for two rapidity ranges, as shown in Table

3.4.

Systematics due to the fitting algorithm, instrumental effects, background, and theory were considered. As mentioned previously, plots comparing the data and Monte Carlo simulations in Appendix C show relatively good agreement in variables from transverse momentum to vertex positions with the aforementioned exceptions discussed in the cases of the topology rapidity and invariant mass distributions. To account for this, a 10% systematic error was assigned to the measured c for the topology data.

Since the main result depends on a fit to the $t \sim p_T^2$ distribution, another important consideration was the sensitivity of the analysis to the p_T resolution. (The resolution is ~ 7.5 MeV/ c and smearing is a significant effect in the first two p_T bins.) To test the effect, the fit was performed on the “raw” (without efficiency correction) t spectrum. The c parameter decreased by 18% [42]. In addition, there was not much variance in the results when the analysis was performed for the forward and backward regions of the detector. The analysis was performed separately for all four cases of: $z_{\text{Vertex}} > 0$; $z_{\text{Vertex}} < 0$; $y > 0$; and $y < 0$. Considering these studies, a 4% systematic error was assigned to reflect non-trigger detector effects.

Background pions also contributed to the systematic error. To take this into account, we studied how the inclusion of like-sign pion pairs affected the measured c . Because the value changed $\sim 0.5\%$, a 1% systematic error was assigned to c to account for the background effect.

In the rapidity region, $0.5 < y < 1.0$, the χ^2/dof of the fits for both data sets are significantly larger than 1. Since the χ^2 did not decrease substantially from variations

in the fit functions or variations in the detector simulation, the statistical errors on c were scaled by the factor of the $\sqrt{\chi^2/\text{dof}}$ to account for excess undetermined error. Including this scaling, the recalculated weighted average is: $c_{\text{avg}} = 0.87 \pm 0.05$.

3.2.5 Results and Conclusions

The final measured value of c was 87 ± 5 (stat.) ± 8 (sys.)% [68] (considering an “expected” 100% interference effect.) Decoherence, $1 - c$, is then less than 23%. Decoherence occurs because the initially-produced ρ^0 s decay prior to any possible overlap of their wave functions from their production points. Therefore, the interference must occur between the decay products of the ρ^0 s, implying that the pion wavefunctions retain all amplitudes of possible ρ decays until the wavefunctions from the two ions can overlap. Because the wavefunction must be a non-local wavefunction, this is an example of the Einstein-Podolsky-Rosen paradox involving continuous variables of momentum and position [72].

Trigger	Rapidity bin	A (GeV^{-2})	k (GeV^{-2})	c	χ^2/dof
minbias	$ y < 0.5$	$11,070 \pm 311$	299 ± 12	0.92 ± 0.07	45/47
minbias	$0.5 < y < 1.0$	$12,060 \pm 471$	303 ± 15	0.92 ± 0.09	76/47
topology	$0.005 < y < 0.5$	6471 ± 301	350 ± 8	0.73 ± 0.10	53/47
topology	$0.5 < y < 1.0$	5605 ± 330	333 ± 11	0.77 ± 0.18	64/47

Table 3.4. Fits to the two upc data sets: topology and minbias.

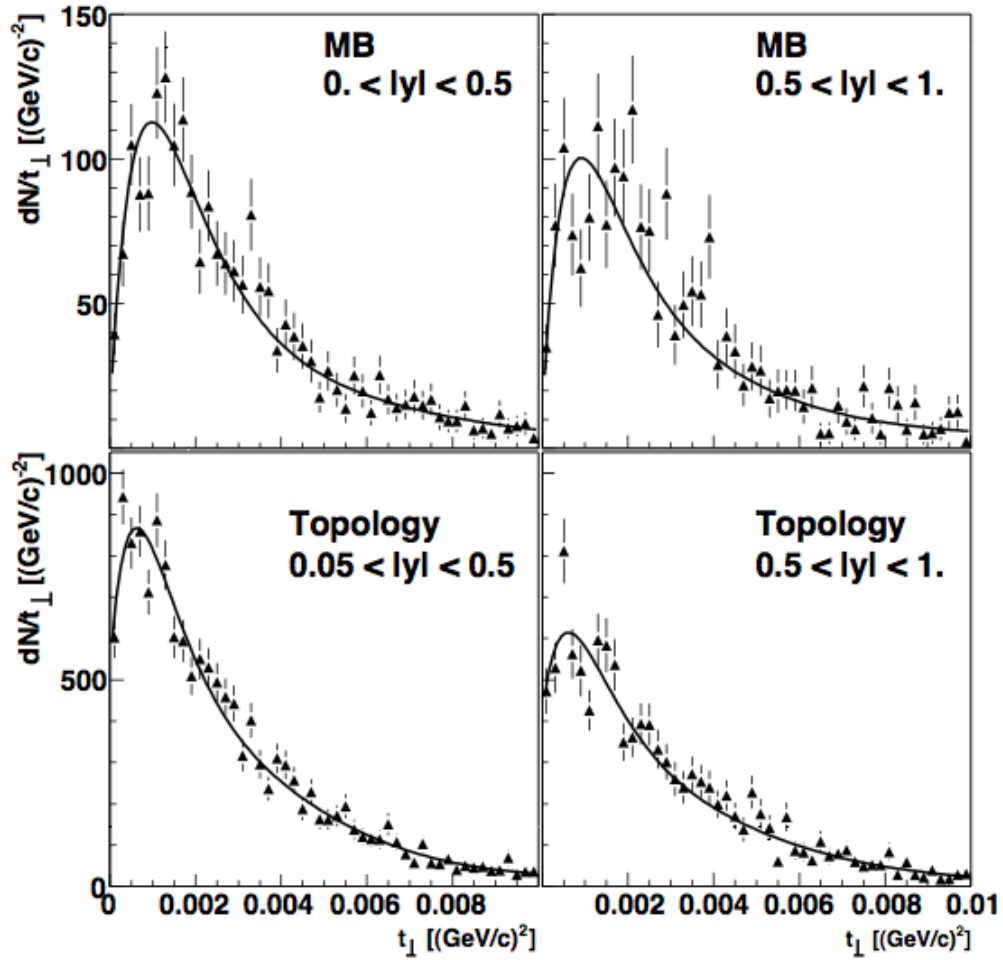


Figure 3.10. Efficiency corrected t_{\perp} spectrum for ρ^0 from (**top**) minimum bias and (**bottom**) topology data, for midrapidity (**left**) and larger rapidity (**right**) samples. The points with error bars are the data, overlaid with the multi-parameter fit (**solid line**) prescribed in Equation 3.4 [68].

Chapter 4

Multi-hadron Triggered Correlations

4.1 Introduction

When hard¹ partons scatter inelastically off each other, as in a p+p collision, they produce more partons. Because of color confinement (the attractive color force between partons increases with increasing distance between them) we do not observe the bare quarks directly. Instead they bind with other quarks to form hadrons almost as immediately after they are created, on a confinement length scale of roughly 1 fm [51]. This hadron formation is referred to as fragmentation.

Figure 4.1 illustrates the formation of a dijet event from the hard scattering of incoming partons labeled a and b . Jets, the result of parton fragmentation, are

¹Here ‘hard’ refers to the large scale of either mass or transverse momentum which makes pQCD calculations feasible.

concentrations of hadrons emitted into a narrow phase space cone. Jets have been studied for years in e^+e^- , $p+p$, and $p+\bar{p}$ collisions by particle physicists. Figure 4.2 shows a dijet invariant mass distribution in $p+\bar{p}$ collisions at 1.8 TeV measured by the CDF collaboration.

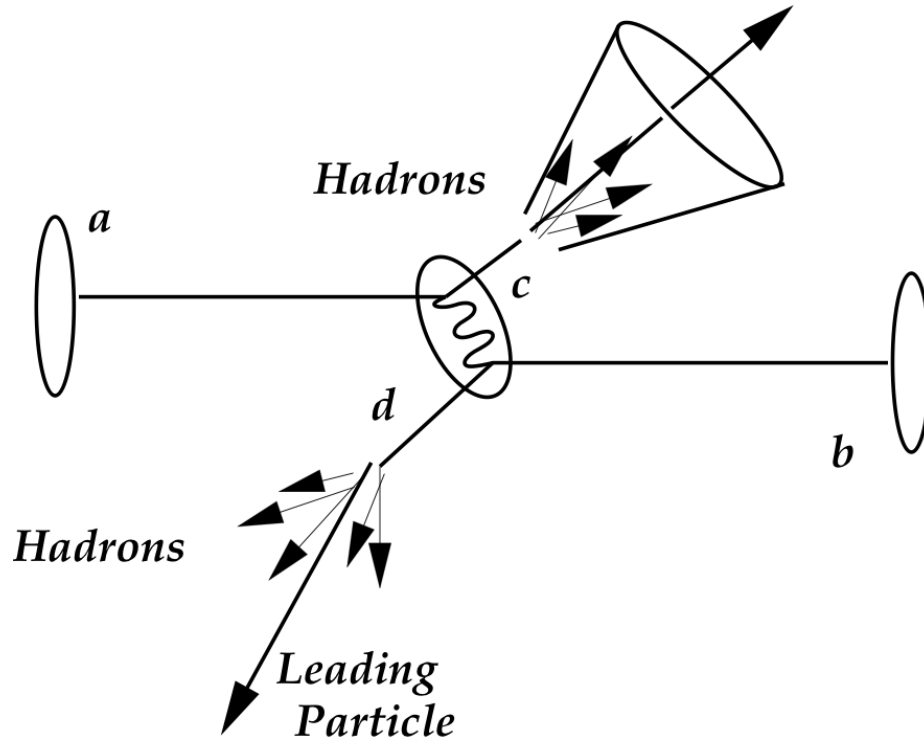


Figure 4.1. A cartoon with notation corresponding to Equation 4.2, depicting a $p+p$ collision in which hadron jets are produced.

Because the yield of a hard-scattered parton is sensitive to the original energy and direction of the parton, jets can be used as probes of parton interactions in heavy-ion collisions. Since they originate from hard scatterings before the strongly-interacting medium is created in heavy-ion collisions, they are a natural probe of the medium. In addition, since jets are well-studied in $p+p$ collisions, there is a baseline for understanding any jet modification due to the medium created in heavy-

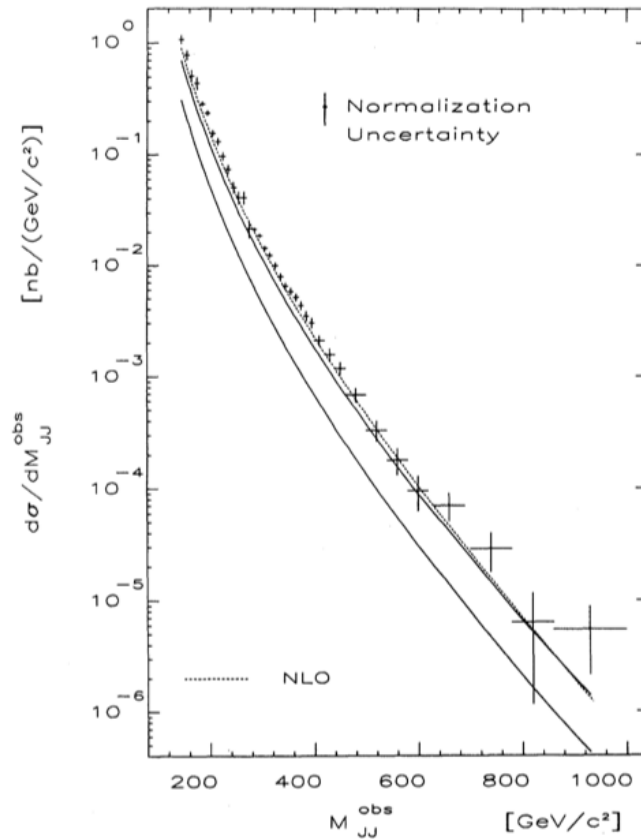


Figure 4.2. Dijet invariant mass distribution from $p+\bar{p}$ collisions at 1.8 TeV as measured by the CDF collaboration [54]. The dotted line (the very top line underlying the data) is a NLO prediction calculated with the HMRS B structure function. The two solid lines define the envelope of different LO QCD predictions which come from varying the renormalization scale.

ion collisions.

Recent experiments at RHIC have shown that in high-energy heavy-ion collisions, a strongly-coupled medium consisting of deconfined quarks and gluons has been produced [1, 55, 59, 66]. This medium has been demonstrated to exhibit an opacity to hard-scattered partons. It is postulated that the leading parton loses energy as it traverses the medium [60] and its fragmentation is subsequently modified. If the medium created is indeed a QGP, a parton moving through it should experience energy loss, both collisional and radiative via gluon bremsstrahlung [56, 57, 58]. As the degree of energy loss is predicted to depend on the density of gluons in the medium as well as the path length traversed through the medium, jets can be used to probe the medium and convey information about the properties and structure of the medium through their degree of energy loss [56].

One way of understanding jet modification due to the medium is to look at the momentum distributions of jet particles which lose energy by interacting with the medium. Measuring jet fragmentation functions is a way to study modifications to the momentum distributions. A fragmentation function is defined as:

$$D(z) = \frac{1}{N_{\text{jets}}} \frac{dN_{\text{ch}}}{dz} \quad (4.1)$$

where z is the momentum fraction $p_L/E_{T\text{jet}}$, p_L is the momentum of a particle along the jet axis and $E_{T\text{jet}}$ is the transverse energy of the jet. Comparing fragmentation functions measured in p+p collisions or peripheral heavy-ion collisions to those measured in central heavy-ion collisions can give an indication of in-medium jet modification.

The fragmentation function is an important factor included in the overall cross section for jet production in p+p collisions:

$$\frac{d\sigma_{pp}^h}{dyd^2p_T} = K \Sigma_{abcd} dx_a dx_b f_a(x_a, Q^2) f_b(x_b, Q^2) \frac{d\sigma}{dt}(ab \rightarrow cd) \frac{D_{h/c}^0}{\pi z_c} \quad (4.2)$$

The other important elements are the parton distribution functions, $f_a(x_a, Q^2)$, $f_b(x_b, Q^2)$, and the hard-scattering cross section, $\frac{d\sigma}{dt}(ab \rightarrow cd)$. Parton distribution functions are derived from experimental data and define the probability for a parton to carry a certain fraction of the total momentum of its parent hadron. The hard-scattering cross section gives the probability that partons a and b as indicated in Figure 4.2 will interact to produce a jet.

As previously stated, to characterize parton energy loss, it is necessary to measure the fragment distribution of hadrons in jets. So far, dihadron correlations [60] have been used to do this in heavy ion collisions. This technique was developed because the large background of soft particles produced in heavy ion collisions makes it difficult to directly reconstruct jets. It was assumed that the jet cone and k_T jet finding algorithms employed in particle physics experiments would be too heavily biased by underlying event background to be useful². In dihadron correlations, the transverse momentum of a trigger particle, p_T^{trig} , is used as a proxy for the jet energy, E_T^{jet} . Then

²Particle physicists have honed jet-finding algorithms over years of experiment [61, 62]. In general terms, a jet-finding algorithm clusters fragmented hadrons to recover the momentum of the parent parton. There are two major categories of jet-finding algorithms: k_T and cone algorithms. They both work by grouping particles close in phase space into a jet. While k_T -algorithms typically divvy all final-state particles into jets, cone algorithms do not. Cone algorithms are more typically used for jet reconstruction in heavy ion collisions, whereas k_T -algorithms are more typically used in lepton collisions. In a collision involving leptons, it is safe to assume that all the detected particles belong to jets, while in heavy ion collisions, there are many produced particles that are definitely not from jets.

the distributions of relative angles in ϕ between the trigger particle and associated particles in an event, including actual jet fragments and uncorrelated background particles, are extracted [60]. Figure 4.3 (a) shows azimuthal angle dihadron distributions for minimum bias and central d+Au collisions as well as p+p collisions [60]. The bottom panel (b) shows pedestal-subtracted dihadron azimuthal distributions in p+p, central d+Au and Au+Au collisions. The trigger and associated p_T ranges are: $4.0 < p_T^{\text{trig}} < 6.0$ GeV/ c and $2.0 < p_T^{\text{assoc}} < 4.0$ GeV/ c . When $\Delta\phi \sim 0$, all distributions, d+Au, p+p, and Au+Au, have similar near-side peaks indicative of jet production. On the away-side ($\Delta\phi \sim 180^\circ$) there are also peaks in the p+p and d+Au data, indicating a back-to-back jet structure. This is not seen in the central Au+Au data, suggesting a suppression of the away-side jet not seen in d+Au and p+p. If the suppression were due to cold matter nuclear effects where no medium modification is expected, then the same suppression would be observed in d+Au collisions. Instead there is no suppression and the d+Au data are comparable to the p+p data. The four experiments at RHIC have agreed on the conclusion that the suppression indicates energy loss in the medium [63, 64, 65, 66].

This study utilized a cone algorithm to group clusters of multiple high- p_T hadrons which were then used as the ‘trigger particle’. This was an original addition to the standard dihadron analysis. Using a multi-hadron cluster could provide a better measure of the jet energy than just the leading particle p_T since multiple hadrons from the jet are being included in the approximation of the jet energy as opposed to just one.

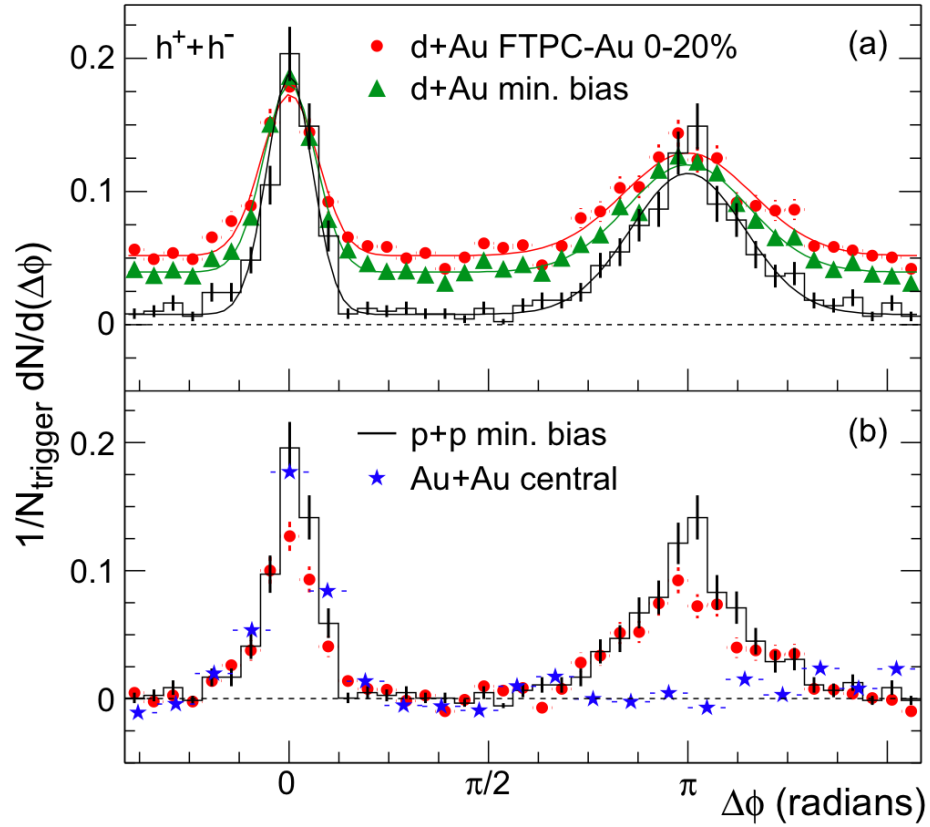


Figure 4.3. (a) Efficiency corrected two-particle azimuthal distributions for minimum bias and central d+Au collisions, and for p+p collisions [60]. Curves are fits detailed in [63]. (b) Comparison of two-particle azimuthal distributions for central d+Au collisions to those seen in p+p and central Au+Au collisions [60]. The respective pedestals have been subtracted.

4.2 Analysis Technique

In this study, approximately 24M events are used from the year 4 run at RHIC, Au+Au collisions at $\sqrt{s_{NN}} = 200$ GeV. The events are selected from the central triggered data in the 0 - 12% centrality bin as determined by the Zero Degree Calorimeters. This includes only events corresponding to the most central 12% of the total hadronic cross section. The requirements of the Au + Au Central trigger are given in Table 4.1.

Detector	Threshold
ZDC EAST & WEST	> 5
ZDC SUM	≤ 131
CTB SUM	> 3500
BBC VERTEX	$ z < 15$ cm
BLUE & YELLOW	synch

Table 4.1. Detector thresholds for the 2004 Au + Au Central trigger (Trigger Word = 15105). Values in the table are quoted in ADC counts unless otherwise specified.

The two global characteristics considered in event selection are centrality and primary vertex location. As specified for the aforementioned Central trigger, only the 12% most central events are considered. From there, twelve uniform vertex bins are defined from a minimum vertex position of 0 cm to a maximum vertex position of 30 cm. Events are grouped into these bins. If an event has a primary vertex within 30 cm of the center of the detector, tracks from the event are processed.

Tracks from selected events are then subject to quality cuts, as shown in Table 4.2. If tracks pass quality cuts, they are looped over to construct multi-hadron trigger clusters and to form angular difference distributions with associated tracks.

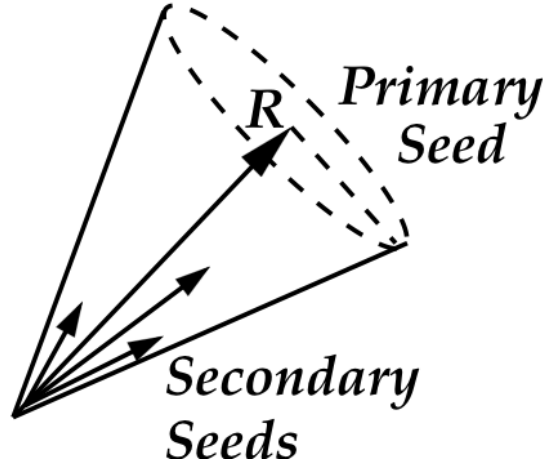


Figure 4.4. Cartoon depicting a multi-hadron trigger. A primary seed is selected and secondary seeds within a cone radius, R , are added to give the trigger p_T .

Track Variable	Cut
number of fitpoints	≥ 20
global DCA	≤ 1 cm
$ \eta $	< 1

Table 4.2. Quality cuts invoked on tracks before including them in the multi-hadron trigger algorithm.

There are three main loops performed. All tracks which pass the track quality cuts with $p_T > 5.0$ GeV/ c are collected as “primary seeds”. Then, within a cone radius ($r = \sqrt{\Delta\phi^2 + \Delta\eta^2}$) of 0.3, all “secondary seeds” which fall above a minimum p_T cut are collected. Minimum secondary seed cuts of 2, 3, and 4 GeV/ c have been

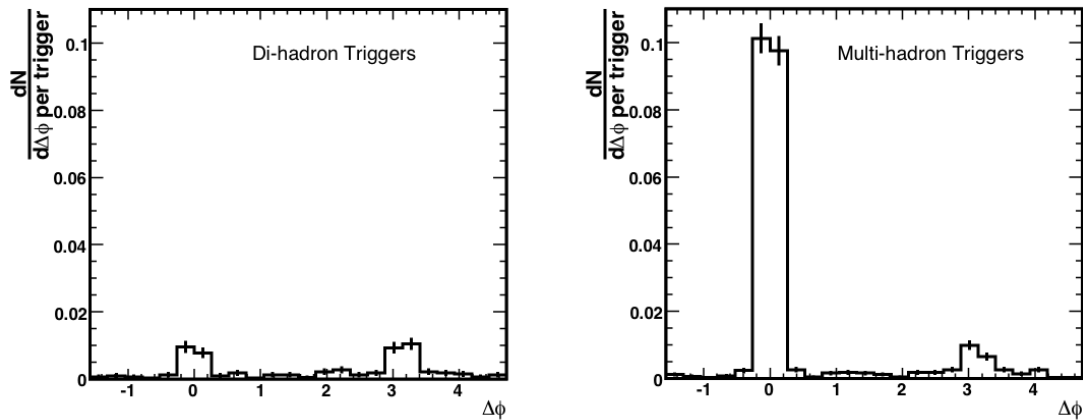


Figure 4.5. Background subtracted azimuthal distributions for dihadron triggers (left) and multi-hadron triggers (right) for $12 < p_T^{trig} < 15$ GeV/ c and 4.0 GeV/ $c < p_T^{assoc} < 5.0$ GeV/ c . A minimum secondary seed of 3.0 GeV/ c is used.

used for a systematic study. Next, the sum of the primary and secondary seeds is taken to be the trigger p_T . To illustrate, a multi-hadron trigger of 12 GeV/ c might be a combination of a 6 GeV/ c primary seed and two secondary seeds of 3 GeV/ c each while, in the standard dihadron analysis [60], the trigger would be a single hadron with $p_T = 12$ GeV/ c . In Figures 4.6 and 4.7 the number of triggers as a function of tracks in a cluster and p_T^{trig} are shown for minimum secondary seed cuts of $p_T > 3.0$ GeV/ c and $p_T > 4.0$ GeV/ c , respectively. The overwhelming majority of triggers have one, two, or three tracks with a small fraction containing four tracks and a very small fraction containing five tracks.

With the multi-hadron triggers defined, azimuthal difference distributions are calculated between the primary seed in the cone and associated tracks with p_T greater than the minimum secondary seed p_T cut. Representative distributions are shown

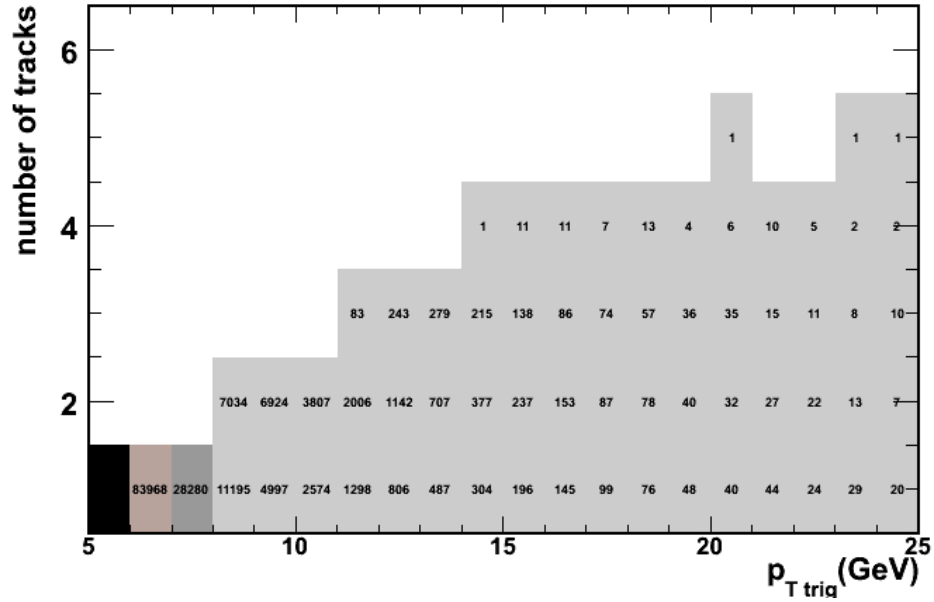


Figure 4.6. Number of multi-hadron triggers as a function of the number of tracks in a cluster and p_T^{trig} with a minimum secondary seed cut of $p_T > 3.0$ GeV/c.

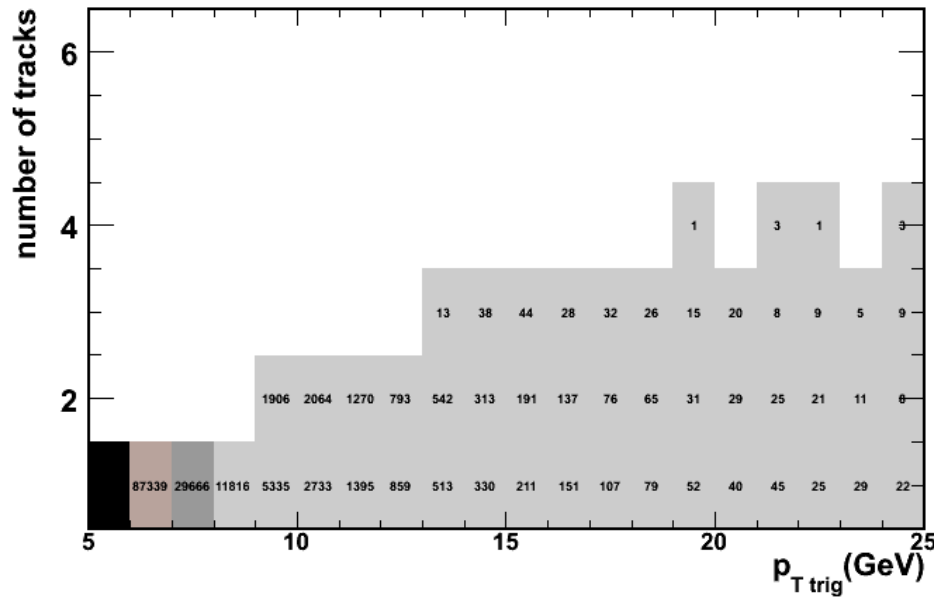


Figure 4.7. Number of multi-hadron triggers as a function of the number of tracks in a cluster and p_T^{trig} with a minimum secondary seed cut of $p_T > 4.0$ GeV/c.

in Figure 4.5. On the left are the dihadron correlations and on the right are the multi-hadron correlations. There is a bias on the near-side multi-hadron triggers due to the algorithm which artificially enhances the yield. This bias comes from the auto correlation of the trigger particle with itself. The peak at $\Delta\phi = 0$ is subsequently enhanced over the actual yield.

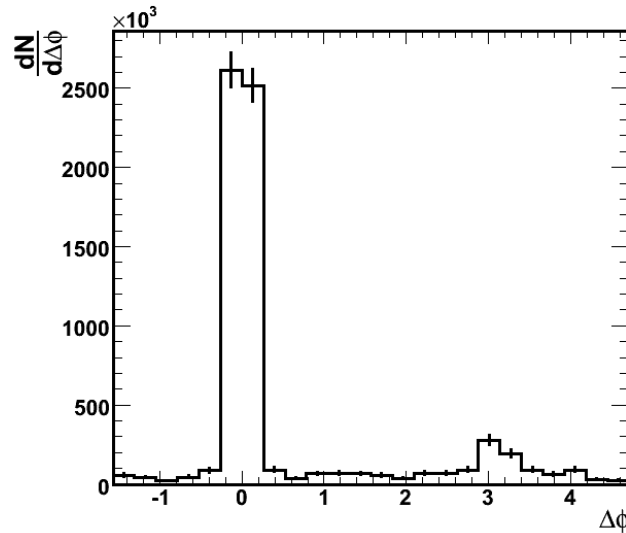


Figure 4.8. Raw azimuthal distribution for multi-hadron triggers with a minimum secondary seed of 3.0 GeV/c for $12 < p_T^{trig} < 15$ GeV/c and 4.0 GeV/c $< p_T^{assoc} < 5.0$ GeV/c.

Uncorrelated background is removed assuming zero yield at minimum [67]. As seen in Figure 4.8, which shows a representative raw azimuthal distribution for multi-hadron triggers, elliptic flow (v_2) is a less than 1% modulation of the background in the ranges selected for p_T^{trig} and p_T^{assoc} . As the signal to background is much larger than 1%, it is considered a negligible effect.

After background-subtraction distributions, recoil (away-side) yields per trigger

are extracted and studied for various p_T^{trig} bins with near and away-side yields as indicated in Figure 4.9.

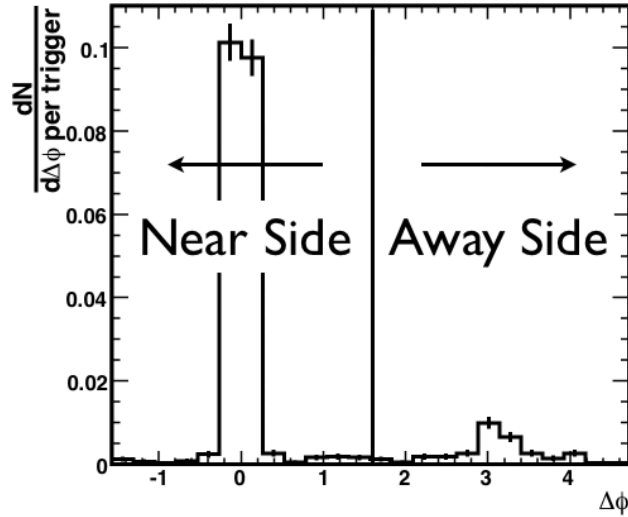


Figure 4.9. Background subtracted azimuthal distribution for multi-hadron triggers with a minimum secondary seed of 3.0 GeV/ c for $12 < p_T^{trig} < 15$ GeV/ c and 4.0 GeV/ $c < p_T^{assoc} < 5.0$ GeV/ c . The solid line in the center indicates the division of the regions integrated for near and away-side yields.

In Figures 4.10 and 4.11 recoil (away-side) yields for two p_T bins, $10 < p_T^{trig} < 12$ GeV/ c and $12 < p_T^{trig} < 15$ GeV/ c with 1 GeV/ c slices in p_T^{assoc} from 3 to 11 GeV/ c , are presented. Figure 4.10 shows a comparison of dihadron (solid triangles) and multi-hadron (open squares) triggers with a minimum secondary seed cut of 3.0 GeV/ c and the p_T^{trig} bins p_T bins: $10 < p_T^{trig} < 12$ GeV/ c and $12 < p_T^{trig} < 15$ GeV/ c for the data (left panels) and PYTHIA (right panels). Figure 4.11 shows the same comparisons but for a minimum secondary seed cut of 4.0 GeV/ c .

In Figures 4.10 and 4.11, the associated per-trigger yields with single-hadron trig-

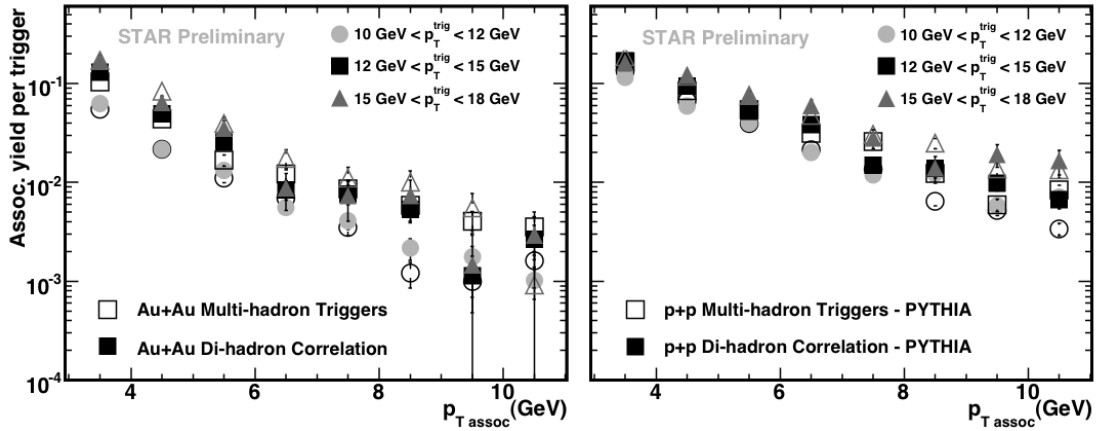


Figure 4.10. Recoil yield per trigger for three p_T bins: $10 < p_T^{trig} < 12$ GeV/ c (circles), $12 < p_T^{trig} < 15$ GeV/ c (squares), and $15 < p_T^{trig} < 18$ GeV/ c (triangles). Data is presented on the left (Au+Au), PYTHIA simulations are presented on the right (p+p). A minimum secondary seed cut of $p_T > 3.0$ GeV/ c is applied.

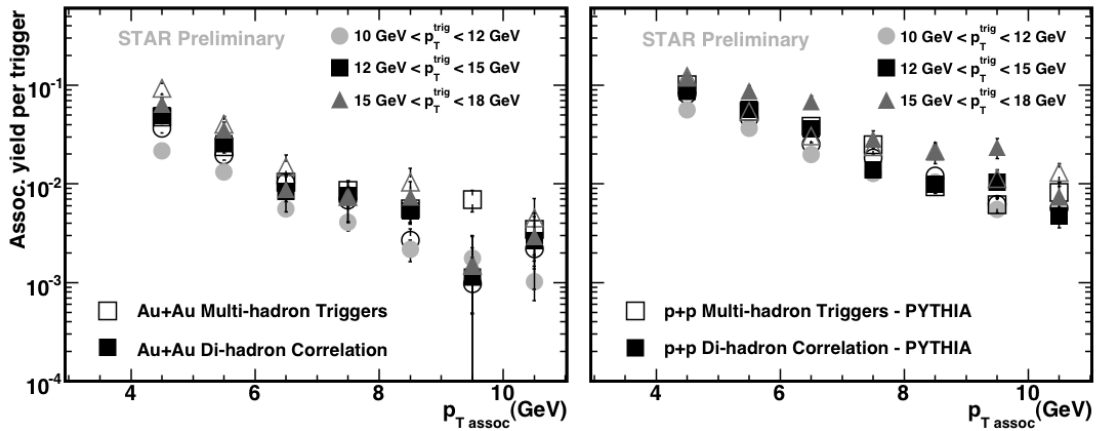


Figure 4.11. Recoil yield per trigger for three p_T bins: $10 < p_T^{trig} < 12$ GeV/ c (circles), $12 < p_T^{trig} < 15$ GeV/ c (squares), and $15 < p_T^{trig} < 18$ GeV/ c (triangles). Data is presented on the left (Au+Au), PYTHIA predictions are presented on the right (p+p). A minimum secondary seed cut of $p_T > 4.0$ GeV/ c is applied.

gers and multi-hadron triggers are similar suggesting that a similar underlying jet-energy distribution is selected by both methods. Events generated with PYTHIA also show this similarity between dihadron correlations and multi-hadron triggered correlation measurements, although the per-trigger yields are generally higher than experimental yields.

4.2.1 d+Au Yields

As a baseline reference, the multi-hadron trigger analysis was performed on d+Au data from the year 3 run at RHIC. Approximately 20M minimum bias triggered events were used. As seen in Figure 4.12, for the regions of interest $p_T^{trig} > 10$ GeV/ c , with a minimum secondary seed cut > 3 GeV/ c , statistics are insufficient for meaningful comparison to the Au+Au results. Unfortunately, a lack of statistics at the time of analysis prevented a meaningful comparison in p+p collisions as well.

4.2.2 Background-Subtracted Yields

Random combinations do occur in the multi-hadron cluster algorithm. The multi-hadron clusters contain a combinatorial background in which a seed particle from a jet is combined with one or more secondary seeds from the underlying soft event. To study this background, the radial distributions of primary seeds for two different cases are constructed: with associated tracks in the same event and with associated tracks in different events. This is accomplished with event mixing. An array of ten events is stored as events are processed. Characteristics of associated tracks: p_T , η ,

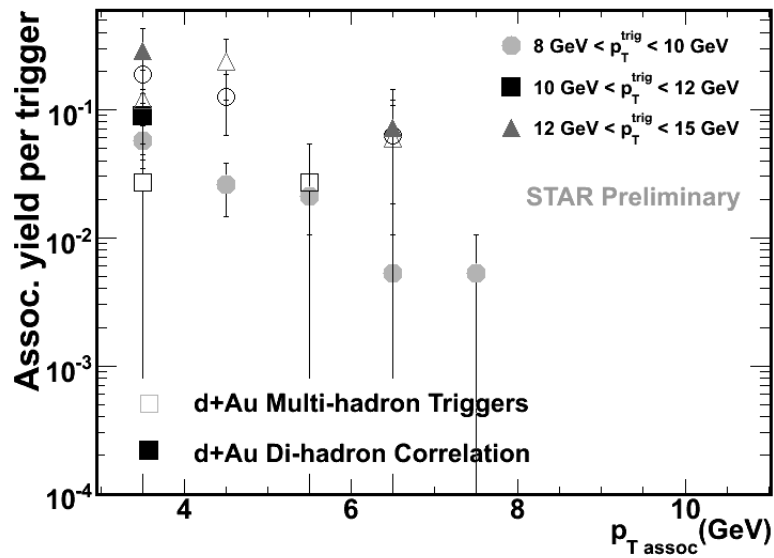


Figure 4.12. Recoil yield per trigger for three p_T bins: $8 < p_T^{\text{trig}} < 10$ GeV/ c (circles), $10 < p_T^{\text{trig}} < 12$ GeV/ c (squares), and $12 < p_T^{\text{trig}} < 15$ GeV/ c (triangles). Results are presented for dAu data. A minimum secondary seed cut of $p_T > 3.0$ GeV/ c is applied.

and ϕ are stored. As an event is analyzed, associated track variables are stored in the array to replace the oldest event in the array. Then the current event is mixed with all the other events in the array to achieve the distributions as shown in Figures 4.13 through 4.16. The ϕ value from a seed track is compared to ϕ values from associated tracks in the ten other events. The repetitive peak structure is consistent with the effect of the TPC endcap sector boundaries. As a cross-check, $\Delta\phi$ correlations were constructed for various charge combinations: $++$, $--$, and $+ -$ in Figures 4.14, 4.15, 4.16. The effect of the sector boundaries varies with respect to same sign or opposite sign combinations of tracks as expected.

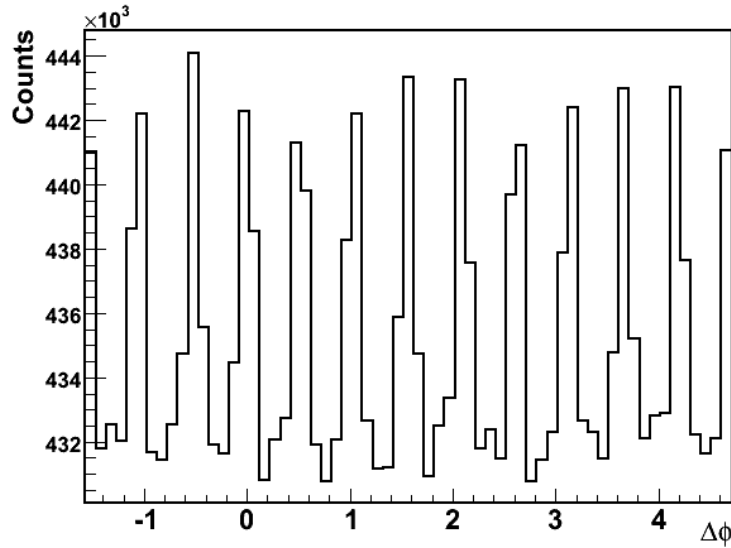


Figure 4.13. $\Delta\phi$ correlations with mixed events. All charge combinations are used between seed tracks and associated tracks. A repetitive peak structure occurs as the effect of the TPC endcap sector boundaries.

To confirm reasonable cone radius and minimum secondary-seed cuts, radial distributions of primary and secondary seeds were generated for tracks in the same event

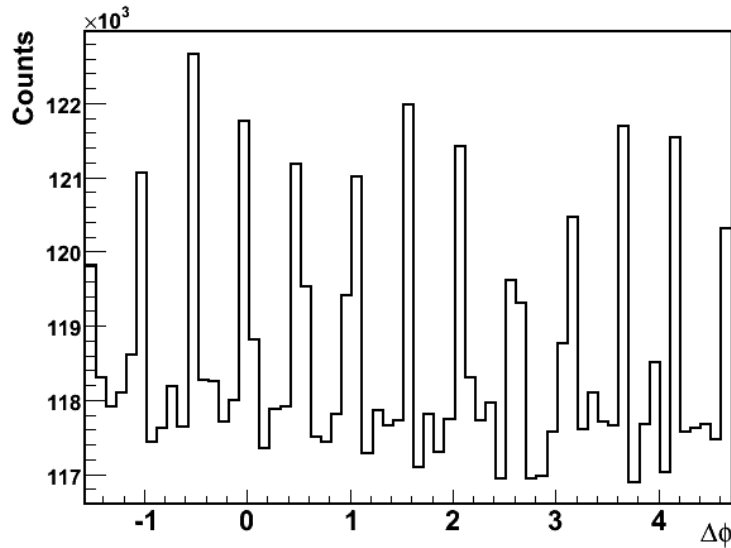


Figure 4.14. $\Delta\phi$ correlations with mixed events. Only positive tracks are used for seed and associated tracks. A repetitive peak structure occurs as the effect of the TPC endcap sector boundaries.

and in mixed events. The plots are shown in Figures 4.17, 4.18, and 4.19. These distributions are shown with the open histograms showing same event correlations and the grey filled histograms showing correlations from mixed events, taking the seed track and the secondary seeds from different events. The background histograms have been scaled to the signal histograms. The secondary seed p_T increases from $p_T > 2.0, 3.0,$ and $4.0 \text{ GeV}/c$ and the signal-to-background increases from 0.2 to 0.7 to 2.0 in Figures 4.17, 4.18, and 4.19, respectively. Subsequently, a radius of 0.3 along with a minimum secondary seed p_T cut greater than $3.0 \text{ GeV}/c$ leads to a reasonable signal to background for this study.

In order to subtract the random background from the raw signal yields, the following algorithm has been employed:

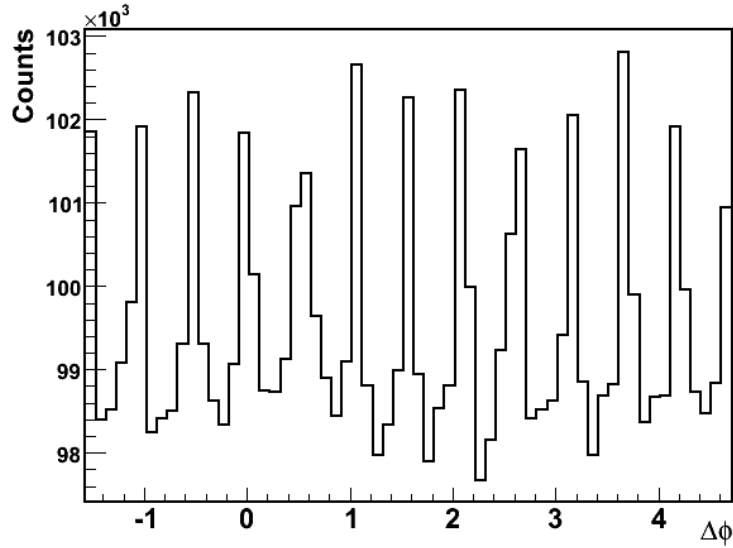


Figure 4.15. $\Delta\phi$ correlations with mixed events. Only negative tracks are used for seed and associated tracks. A repetitive peak structure occurs as the effect of the TPC endcap sector boundaries.

$$\frac{dN}{d\Delta\phi_{\text{signal}}} = \frac{1}{1 - F_{\text{bkg}}} \left(\frac{dN}{d\Delta\phi_{\text{inclusive}}} \right) - F_{\text{bkg}} \left(\frac{dN}{d\Delta\phi_{\text{random}}} \right) \quad (4.3)$$

- $dN/d\Delta\phi_{\text{inclusive}}$ is the inclusive away-side yield including actual jet triggers as well as random triggers from one event;
- F_{bkg} is the fraction of random trigger pairs to all trigger pairs;
- $1/1 - F_{\text{bkg}}$ is a scaling factor to get yields per corrected (non-random) trigger;
- $dN/d\Delta\phi_{\text{random}}$ is away-side yield with untriggered background including triggers from one event and associated tracks from other events.

Figure 4.20 shows the background subtracted multi-hadron yields for triggers with

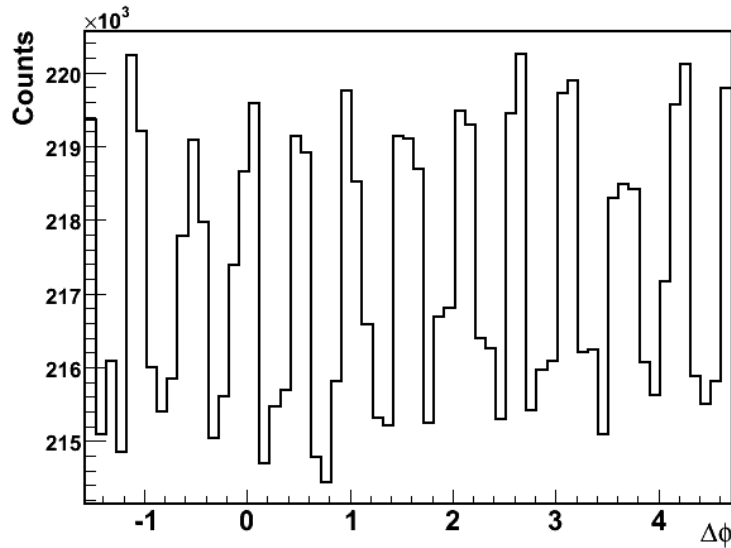


Figure 4.16. $\Delta\phi$ correlations with mixed events. Only oppositely charged tracks are used for seed and associated tracks. A repetitive peak structure occurs as the effect of the TPC endcap sector boundaries.

a secondary seed cut of 4.0 GeV/ c . As shown in Figure 4.21, there is only a small shift in the yields. Associated per-trigger yields with single-hadron triggers and multi-hadron triggers are similar suggesting that a similar underlying jet-energy distribution is selected by both methods. Events generated with PYTHIA also show this similarity between dihadron correlations and multi-hadron triggered correlation measurements, although the per-trigger yields are generally higher than experimental yields.

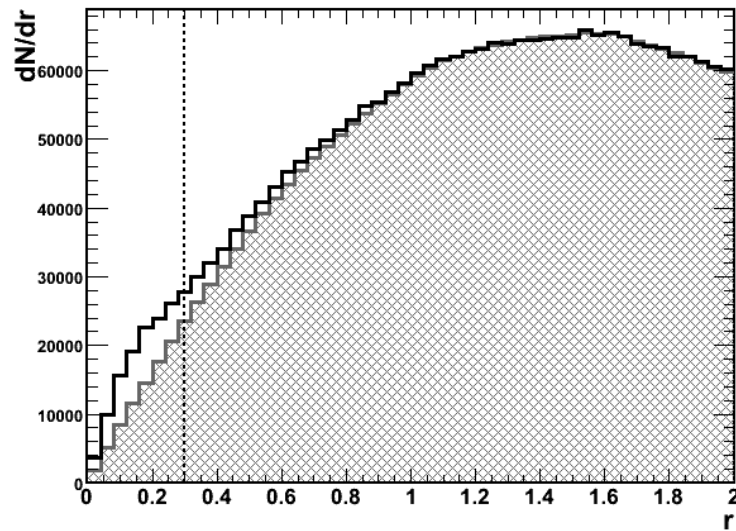


Figure 4.17. Radial distributions of triggers with associated tracks from the same event (white histogram) and from different events (hatched histogram) with a minimum secondary seed cut of $2.0 \text{ GeV}/c$. A guideline is drawn at $r = 0.3$ to show where the analysis cut falls on the data.

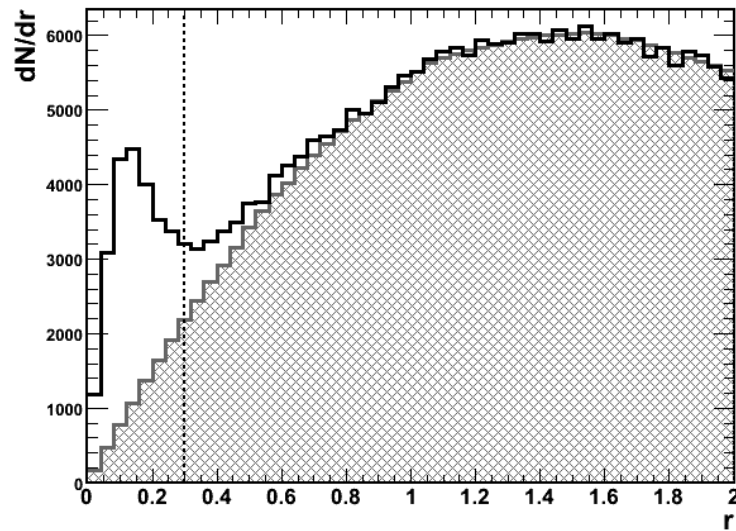


Figure 4.18. Radial distributions of triggers with associated tracks from the same event (white histogram) and from different events (hatched histogram) with a minimum secondary seed cut of $3.0 \text{ GeV}/c$. A guideline is drawn at $r = 0.3$ to show where the analysis cut falls on the data.

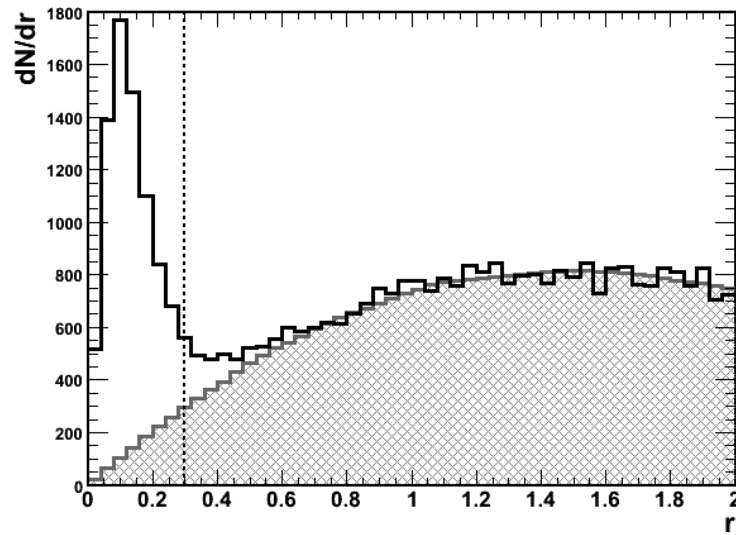


Figure 4.19. Radial distributions of triggers with associated tracks from the same event (white histogram) and from different events (hatched histogram) with a minimum secondary seed cut of $4.0 \text{ GeV}/c$. A guideline is drawn at $r = 0.3$ to show where the analysis cut falls on the data.

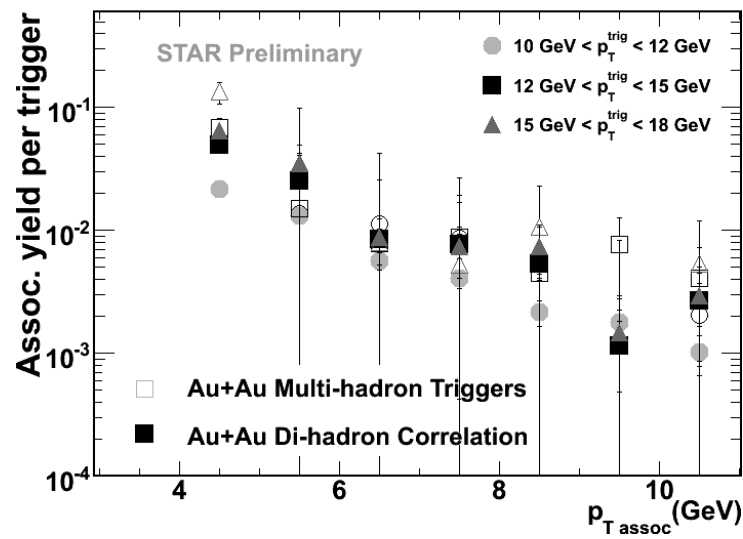


Figure 4.20. Background subtracted recoil yield per trigger for three p_T bins: $10 < p_T^{\text{trig}} < 12 \text{ GeV}/c$, $12 < p_T^{\text{trig}} < 15 \text{ GeV}/c$, and $15 < p_T^{\text{trig}} < 18 \text{ GeV}/c$. A minimum secondary seed cut of $p_T > 4.0 \text{ GeV}/c$ is applied.

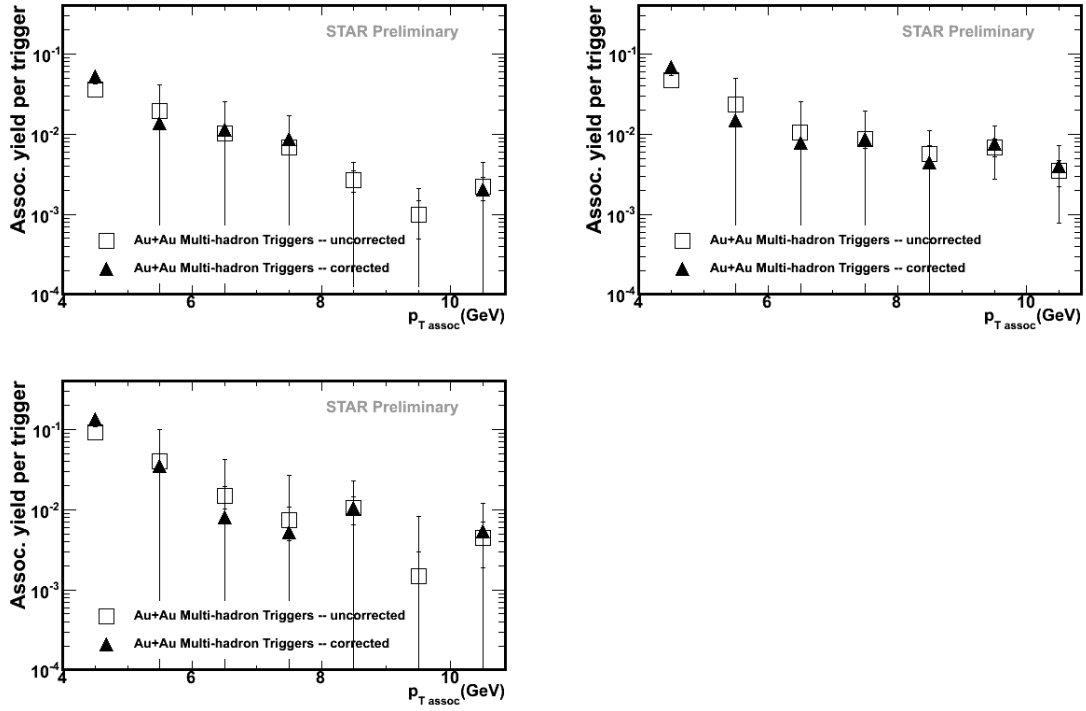


Figure 4.21. Comparison of background subtracted (solid triangles) and raw uncorrected recoil yields per trigger for three p_T bins: $10 < p_T^{\text{trig}} < 12$ GeV/ c (**upper left**), $12 < p_T^{\text{trig}} < 15$ GeV/ c (**upper right**), and $15 < p_T^{\text{trig}} < 18$ GeV/ c (**lower left**). A minimum secondary seed cut of $p_T > 4.0$ GeV/ c is applied.

Chapter 5

Conclusion

The work of this thesis has been twofold: to measure quantum mechanical interference in ρ^0 production in ultra-peripheral heavy ion collisions and to develop a multi-hadron cluster trigger algorithm and extend the di-hadron triggered azimuthal correlation analysis.

5.1 ρ^0 Photoproduction

Quantum mechanical interference has been measured in ultraperipheral Au+Au collisions at $\sqrt{s_{NN}} = 200$ GeV for two different triggered data sets in 2001: the UPC topology and the UPC minbias trigger. A suppression of the cross section in each data set has been measured. The data have been compared to predictions of the STARlight Monte Carlo event generator [37] with good results in the case of the minbias trigger and fair results in the case of the topology trigger. A fit to the ρ^0 yield as a function of t has been applied to extract the interference parameter of $87 \pm$

5 (stat.) \pm 8 (sys.)% [68] (with 100% “expected” interference). This result provides a novel way of observing the Einstein-Podolsky-Rosen paradox as it implies that the interference necessarily occurs between the pions from ρ^0 decays.

5.2 Multi-Hadron Triggered Study

This thesis has presented first results on the use of multi-hadron triggers as a next step toward full jet reconstruction in heavy-ion collisions. Away side per-trigger yields have been extracted in Au+Au collisions at $\sqrt{s_{NN}} = 200$ GeV for three p_T^{trig} bins: $10 < p_T^{trig} < 12$ GeV/ c , $12 < p_T^{trig} < 15$ GeV/ c , and $15 < p_T^{trig} < 18$ GeV/ c . Analysis cuts were optimized to reveal that a trigger cone radius of 0.3 and a minimum secondary seed p_T cut greater than 3 GeV/ c greatly eliminates softer non-jet background from the triggers. Comparisons of the multi-hadron away side yields to the standard di-hadron yields have been made in data and Pythia simulations. The yields are consistent with each other. Background-subtracted yields have been obtained for all three trigger bins and a minimum secondary seed cut of 4.0 GeV/ c . Even after background subtraction, multi-hadron yields are still mainly consistent with di-hadron yields. This observation implies that both methods select a similar underlying jet energy. Furthermore, the multi-hadron correlations extend the di-hadron correlation measurements to a lower z_T range, where z_T is the momentum fraction carried by the leading hadron.

Appendix A

Glauber Model

Because each heavy ion event has a unique impact parameter, understanding experimental observables as a function of centrality is important. The Glauber model [74] can be used to calculate two relevant centrality variables: the number of participants, N_{part} , and the number of binary collisions, N_{coll} , based on the impact parameter of a given collision. To calculate the collisions between participant nucleons in a heavy ion collision, it is necessary to find the probability that a pair of nucleons, one from each nucleus, will overlap. Envisioning a two-dimensional projection of the nuclei individually labeled A and B as two colliding circles with some region of overlap between, an impact parameter dependent nuclear overlap function defined:

$$T_{AB}(\vec{b}) = d^2\vec{s} T_A(\vec{s}) T_B(\vec{b} - \vec{s}) \quad (\text{A.1})$$

The nuclear thickness functions, $T_{A(B)}$, for each nucleus are:

$$T_{A(B)}(\vec{s}) = \int dz \rho_{A(B)}(z, \vec{s}) \quad (\text{A.2})$$

where z is defined perpendicular to the beam axis along the beam direction, \vec{s} is defined so that $r = \sqrt{z^2 + s^2}$, and ρ is the nuclear density profile. Typically a Woods-Saxon distribution [51] is used:

$$\rho(r) = \frac{\rho_0}{1 + \exp\left(\frac{r-r_0}{c}\right)} \quad (\text{A.3})$$

Here ρ_0 is nuclear density, r_0 is the mean radius parameter and c is the skin thickness. The skin thickness defines the point at which the density of the nucleus dramatically decreases toward the edge of the nucleus, dropping from 90% of its nominal value to 10%. The normalization ρ_0 is determined from is

$$\int d^3r \rho(r) = A \quad (\text{A.4})$$

where A is the mass number of the nucleus. Typical values in the Woods-Saxon parameterization are $r_0 \sim 1.07A^{\frac{1}{3}}$, $\rho_0 = 0.169$ nucleons/fm³ (for Au) and $c \sim 0.545$ fm [51].

Considering a binomial probability, the inclusive inelastic cross section can be calculated from the overlap function,

$$\sigma_{AB}(\vec{b}) = \int d\vec{b} [1 - e^{-\sigma_{NN}T_{AB}(\vec{b})}] \quad (\text{A.5})$$

where σ_{NN} is the NN cross section, taken from p+p collisions with ~ 40 mb at RHIC with $\sqrt{s_{NN}} = 200$ GeV.

Now, the number of binary collisions is [51]

$$N_{\text{coll}} = \sigma_{NN} \int d\tilde{s} dz' dz'' \rho_A(z', \tilde{s}) \rho_B(z'', \tilde{b} - \tilde{s}) = \sigma_{NN} T_{AB}(\tilde{b}) \quad (\text{A.6})$$

The number of nucleon participants is [51]

$$N_{\text{part}} = \int d^2s [T_A(s)(1 - e^{-\sigma_{NN}T_B(|\vec{b}-\vec{s}|)}) + T_B(|\vec{b}-\vec{s}|)(1 - e^{-\sigma_{NN}T_A(s)})] \quad (\text{A.7})$$

Appendix B

Topology Trigger MC Simulations

Multiple attempts were made in refining a topology trigger algorithm for the Monte Carlo to improve its comparison to the data. Figures B.1 through B.6 show the outcome of various attempts.

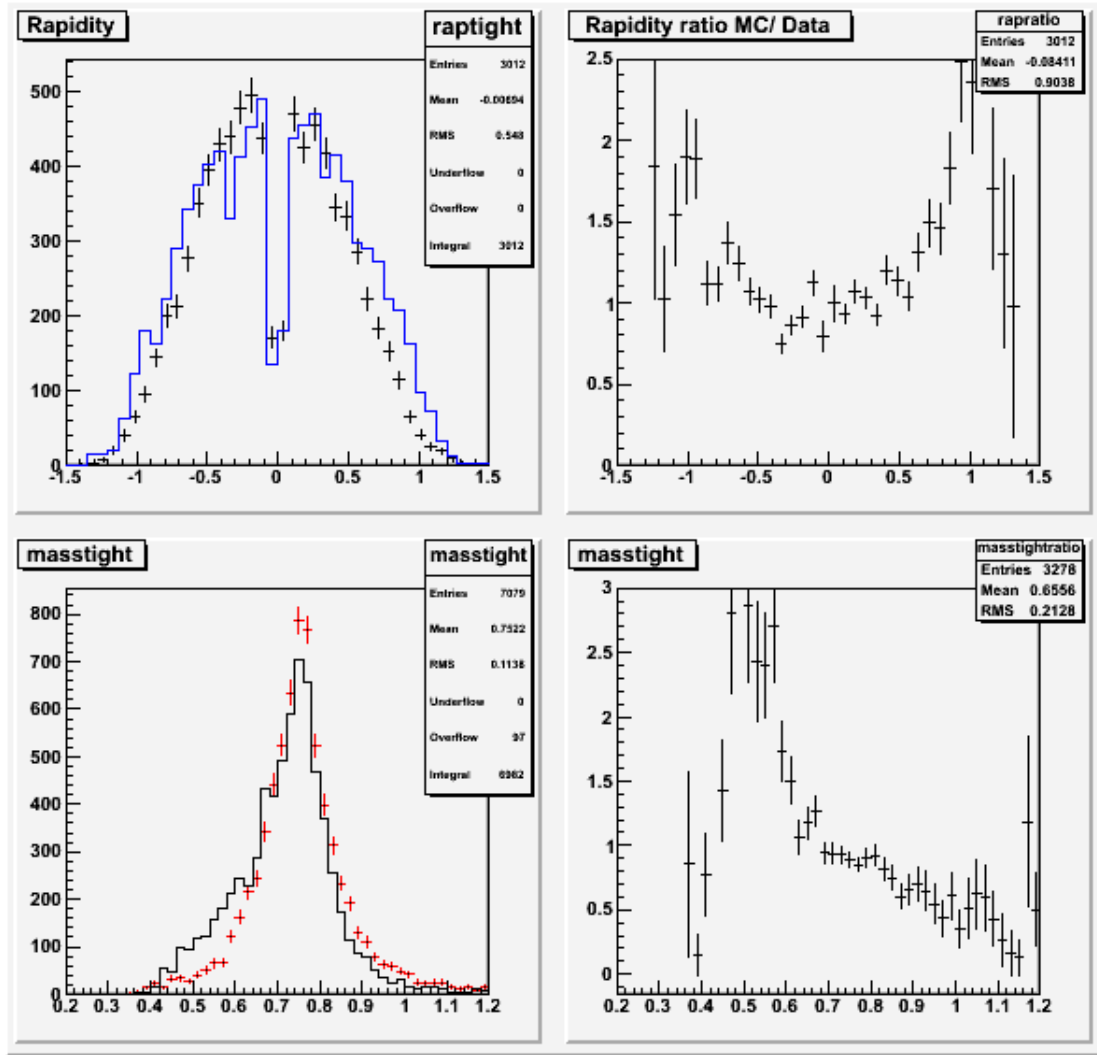


Figure B.1. The top left plot shows a comparison of the rapidity distributions from the data (points) and MC simulation (histogram). The bottom left plot shows a comparison of the invariant mass distributions from the data (points) and MC simulation (histogram). The top right plot gives the ratio of the rapidity distributions, MC to data. The bottom right plot gives the ratio of the invariant mass distributions, MC to data. The distributions are generated subject to the following trigger requirements: If there are multiple hits per CTB tray, only the last one is stored. No cut is made on the ADC value of the hit. The standard trigger simulation from PeCMake is employed.

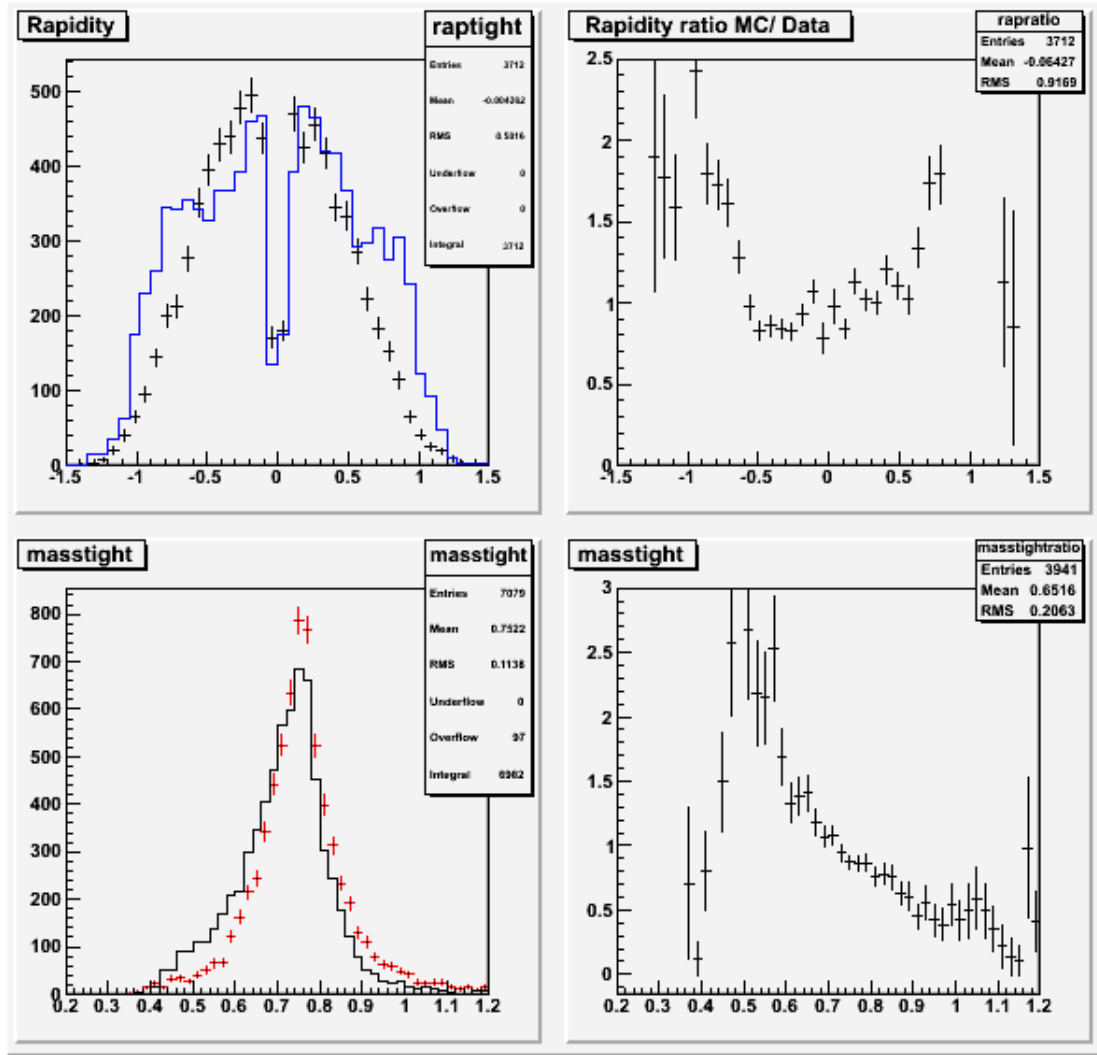


Figure B.2. The top left plot shows a comparison of the rapidity distributions from the data (points) and MC simulation (histogram). The bottom left plot shows a comparison of the invariant mass distributions from the data (points) and MC simulation (histogram). The top right plot gives the ratio of the rapidity distributions, MC to data. The bottom right plot gives the ratio of the invariant mass distributions, MC to data. The distributions are generated subject to the following trigger requirements: If there are multiple hits per CTB tray, the sum of the hits are tabulated as the ADC count of the tray. No cut is made on the ADC value of the hit. The standard trigger simulation from PeCMaker is employed.

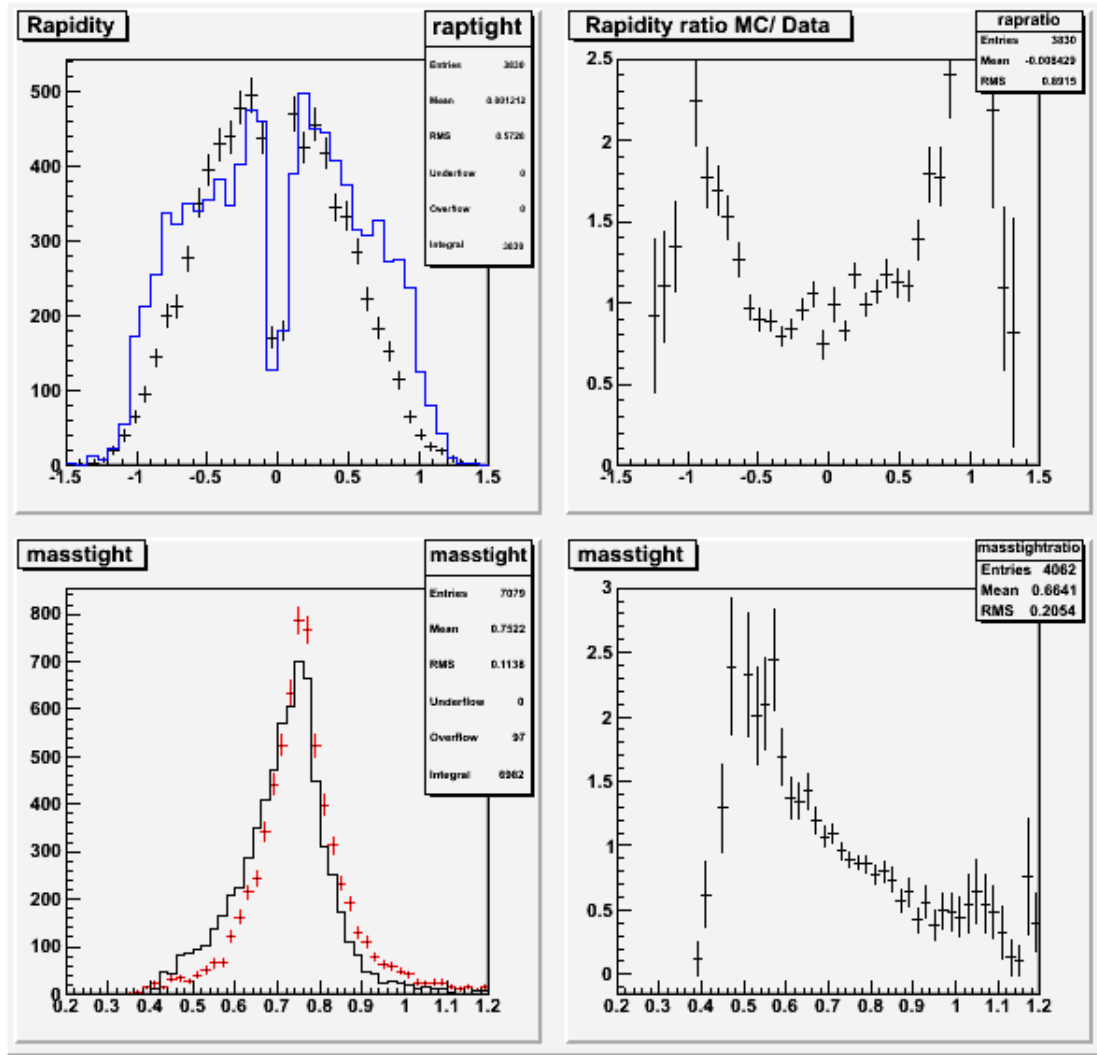


Figure B.3. The top left plot shows a comparison of the rapidity distributions from the data (points) and MC simulation (histogram). The bottom left plot shows a comparison of the invariant mass distributions from the data (points) and MC simulation (histogram). The top right plot gives the ratio of the rapidity distributions, MC to data. The bottom right plot gives the ratio of the invariant mass distributions, MC to data. The distributions are generated subject to the following trigger requirements: If there are multiple hits per CTB tray, the sum of the hits are tabulated as the ADC count of the tray. A cut of > 3 ADC counts is required. The standard trigger simulation from PeCMaker is employed.

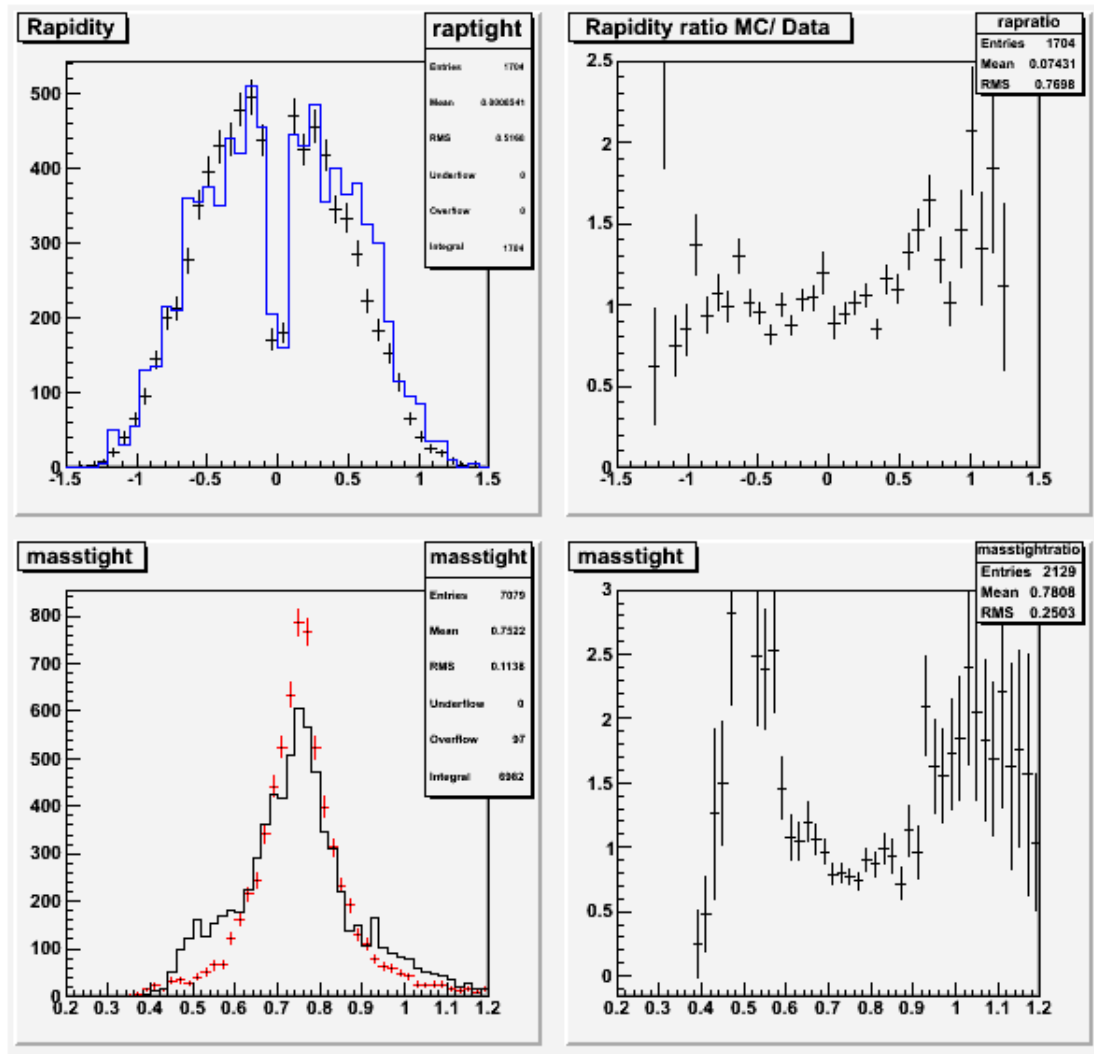


Figure B.4. The top left plot shows a comparison of the rapidity distributions from the data (points) and MC simulation (histogram). The bottom left plot shows a comparison of the invariant mass distributions from the data (points) and MC simulation (histogram). The top right plot gives the ratio of the rapidity distributions, MC to data. The bottom right plot gives the ratio of the invariant mass distributions, MC to data. The distributions are generated subject to the following trigger requirements: If there are multiple hits per CTB tray, only the last one is stored as the ADC count of the tray. No cut is made on the ADC value of the hit. No lookup tables are used for the trigger simulation.

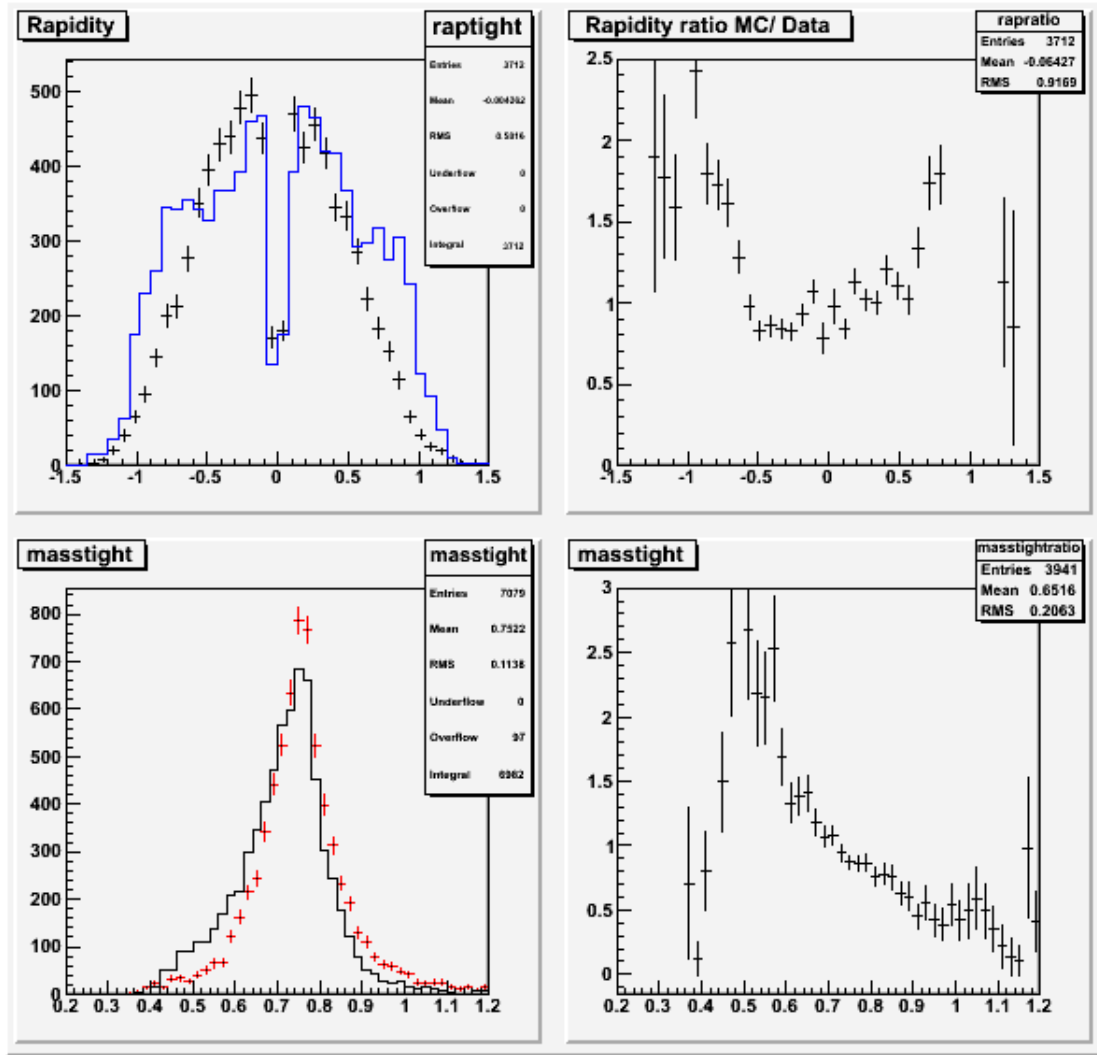


Figure B.5. The top left plot shows a comparison of the rapidity distributions from the data (points) and MC simulation (histogram). The bottom left plot shows a comparison of the invariant mass distributions from the data (points) and MC simulation (histogram). The top right plot gives the ratio of the rapidity distributions, MC to data. The bottom right plot gives the ratio of the invariant mass distributions, MC to data. The distributions are generated subject to the following trigger requirements: If there are multiple hits per CTB tray, the sum of the hits are tabulated as the ADC count of the tray. No cut is made on the ADC value of the hit. No lookup tables are used for the trigger simulation.

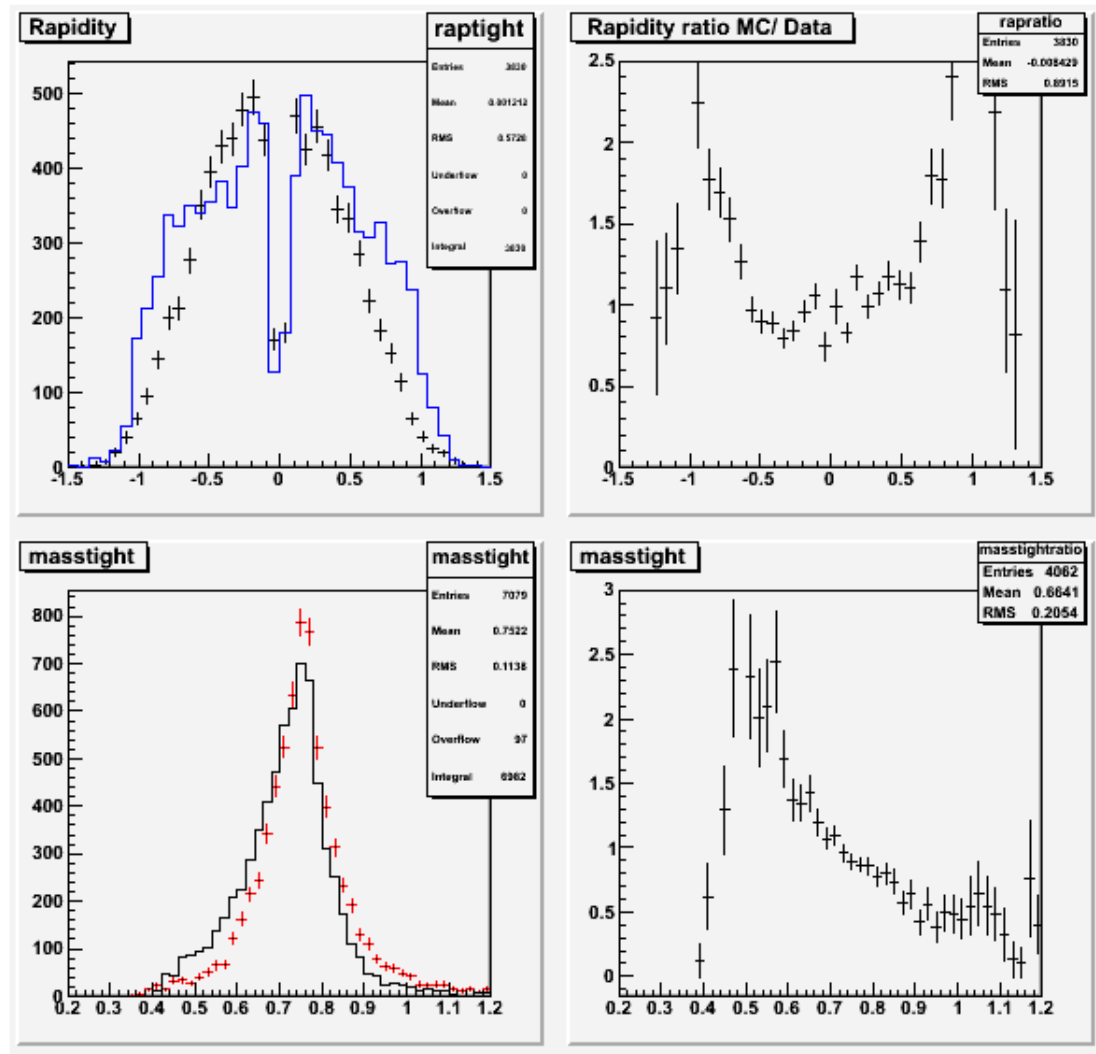


Figure B.6. The top left plot shows a comparison of the rapidity distributions from the data (points) and MC simulation (histogram). The bottom left plot shows a comparison of the invariant mass distributions from the data (points) and MC simulation (histogram). The top right plot gives the ratio of the rapidity distributions, MC to data. The bottom right plot gives the ratio of the invariant mass distributions, MC to data. The distributions are generated subject to the following trigger requirements: If there are multiple hits per CTB tray, the sum of the hits are tabulated as the ADC count of the tray. A cut of > 3 ADC counts is required. No lookup tables are used for the trigger simulation.

Appendix C

Monte Carlo / Data comparisons

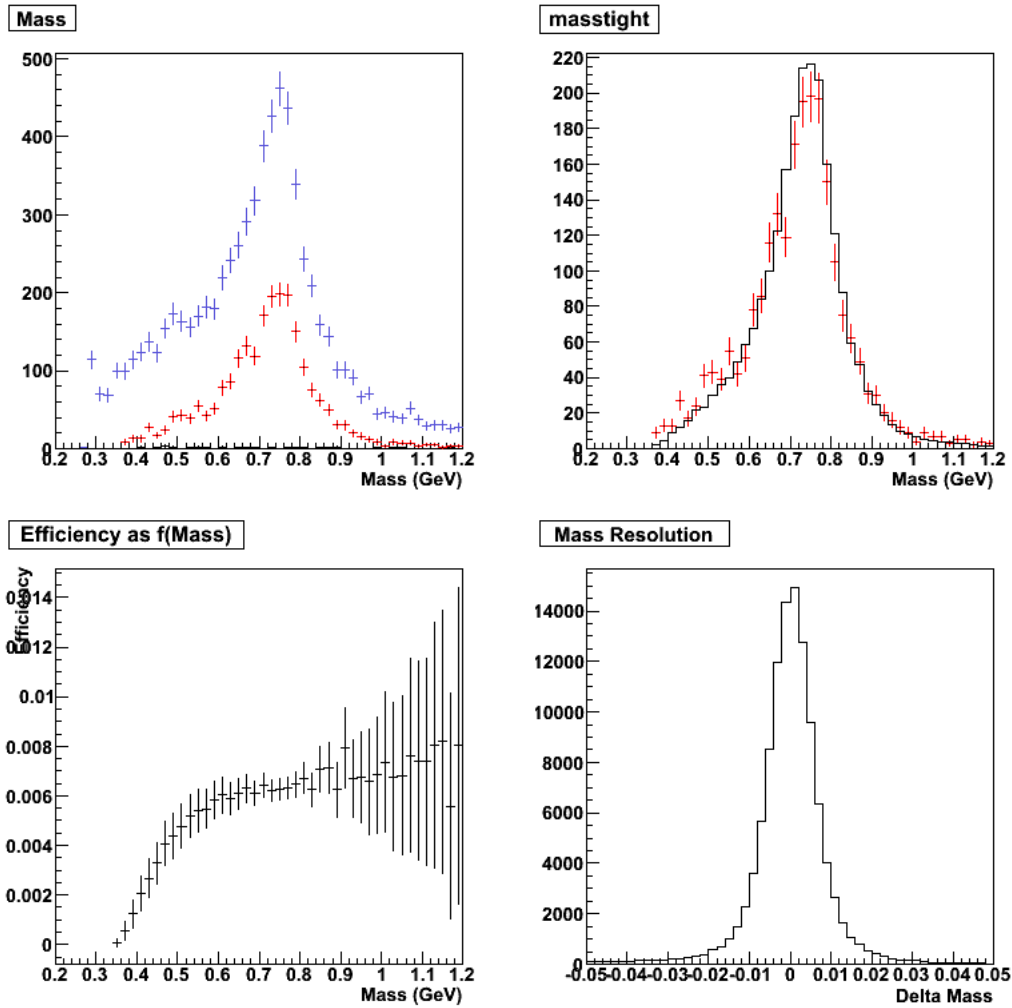


Figure C.1. The upper left histogram compares the data with loose cuts (top, blue), tight cuts (middle, red) and background (bottom black histogram at the zero level). A peak is visible at $M_{\pi\pi} = M(K_s)$. This may be due to photoproduction of the ϕ , followed by $\phi \rightarrow K_s K_L$. Because the Q value of the ϕ decay is so low, most of the K_s still make the p_T cut; the K_L usually vanishes without decaying. The upper right plot compares the data and the Monte Carlo; except for the K_s , the agreement is excellent. The lower left plot shows the efficiency; for $M_{\pi\pi} > 550$ MeV/ c , the efficiency is flat. The last plot shows the $M_{\pi\pi}$ resolution of about 8.3 MeV [73].

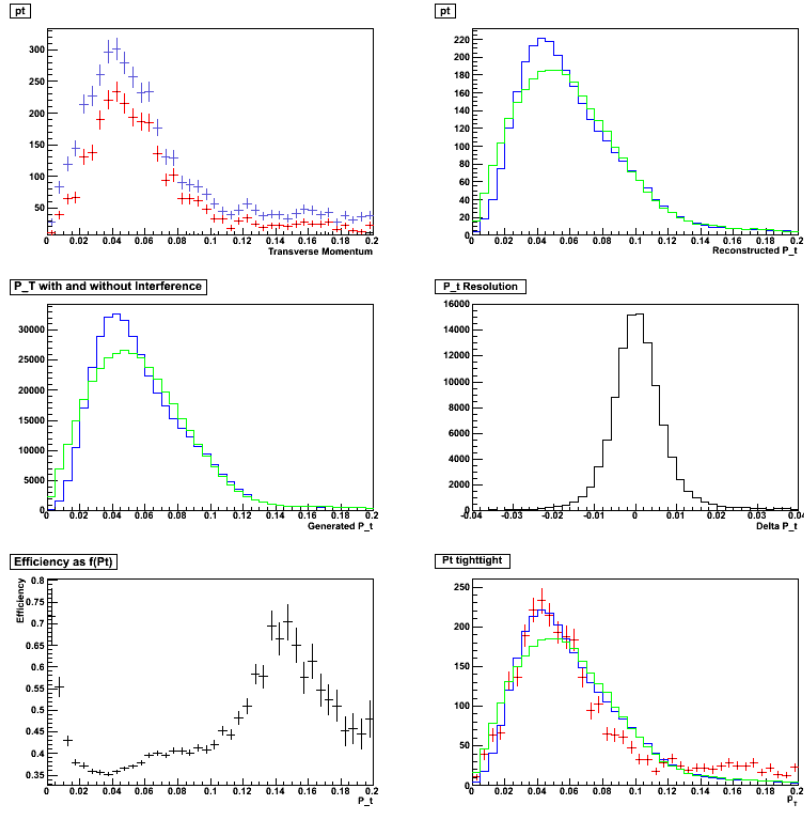


Figure C.2. The upper left histogram compares the p_T spectra with loose (blue) and tight (red) cuts. Events with $p_T > 120$ MeV/ c appear consistent with incoherent ρ^0 production, $\gamma p \rightarrow \rho^0 p$. The upper right plot compares the 'Int' (blue) and 'Noint' (green) p_T spectra, after simulation and reconstruction. The middle left histogram compares the 'Int' (blue) and 'Noint' (green) p_T spectra directly from STARlight, with no detector effects. The middle right histogram shows the p_T resolution is centered at 0, with $\sigma=7.5$ MeV. The lower left histogram shows that the reconstruction efficiency is independent of p_T , except for the lowest bin, which is somewhat higher. This is probably due to p_T smearing. With the 'Int' spectrum (used here, since it matches the data better), the first bin has many fewer events than the next bin, so that there is smearing from bin 2 \rightarrow bin 1, but very little in the other direction. The lower right plot compares the p_T spectra of data (red), 'Int' (blue) and 'Noint' (green). [73]

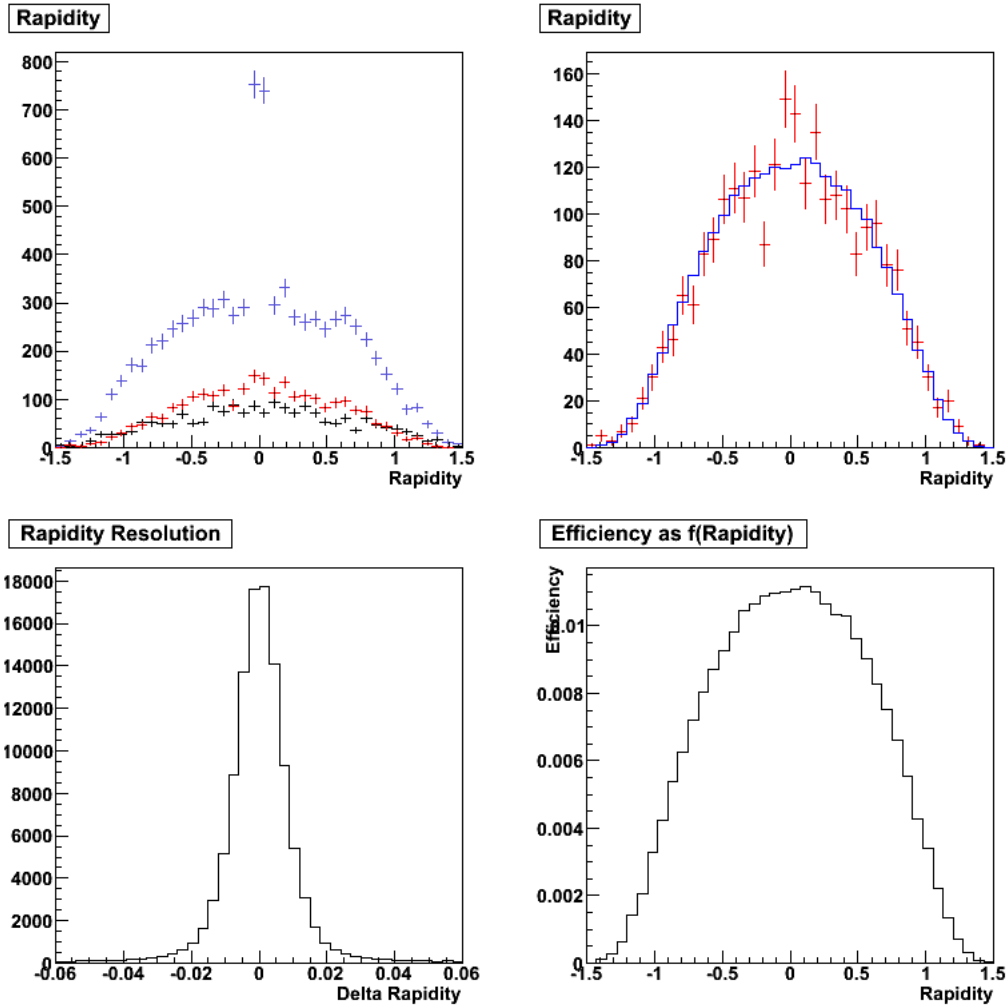


Figure C.3. The upper left histogram compares the data with loose cuts (blue), tight cuts (red), and background (with loose cuts). The loose cut plot shows an enhancement for $|y| < 0.1$. This is likely due to cosmic rays, which are reconstructed as pairs with $y = 0$, $p_T=0$. The upper right histogram compares the data (red) and Monte Carlo (blue), while the lower left histogram shows the rapidity resolution, 0.01. This is very adequate for the analysis. The lower right histogram shows the efficiency as a function of rapidity. It is not flat, since the probability of a daughter pion being outside the TPC acceptance rises as rapidity rises, but since the data and MC agree well, this is no cause for concern. [73]

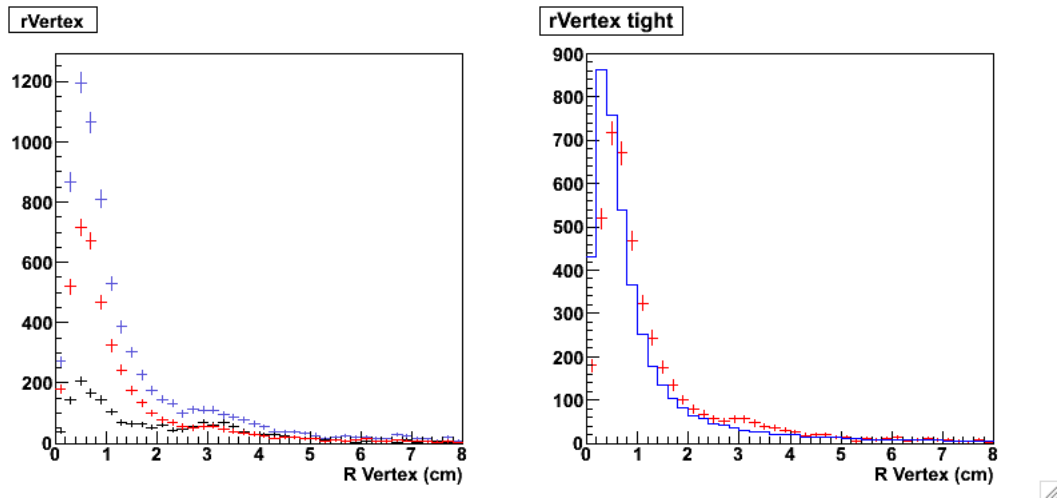


Figure C.4. The left plot shows the data with loose cuts (blue), tight cuts (red), and the background (black). With the loose cuts, a small rise is visible at $r \sim 3$ cm. This disappears once tighter cuts are imposed. The background rate is so high here because there is no cut on z . The plot on the right compares the data (red) and the Monte Carlo (blue). The agreement is good. [73]

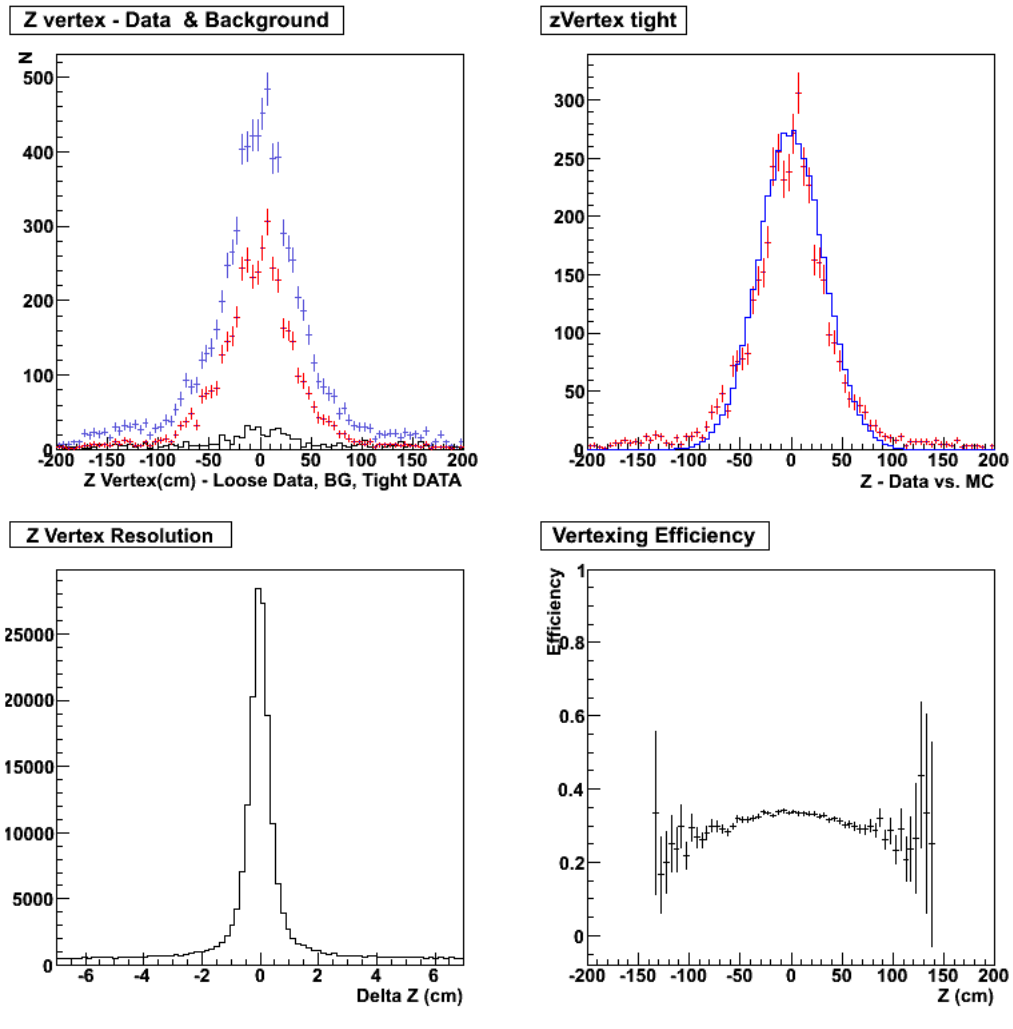


Figure C.5. The upper left histogram compares the data with loose cuts (blue) and tight cuts (red), and the background (black). The upper right histogram compares the (red) data and Monte Carlo (blue). The lower right is the resolution estimated with the Monte Carlo ($zVertex - zMC$); the resolution is 2 cm. The lower left shows the efficiency as a function of $zVertex$. It is approximately flat within the ± 50 cm cut range. [73]

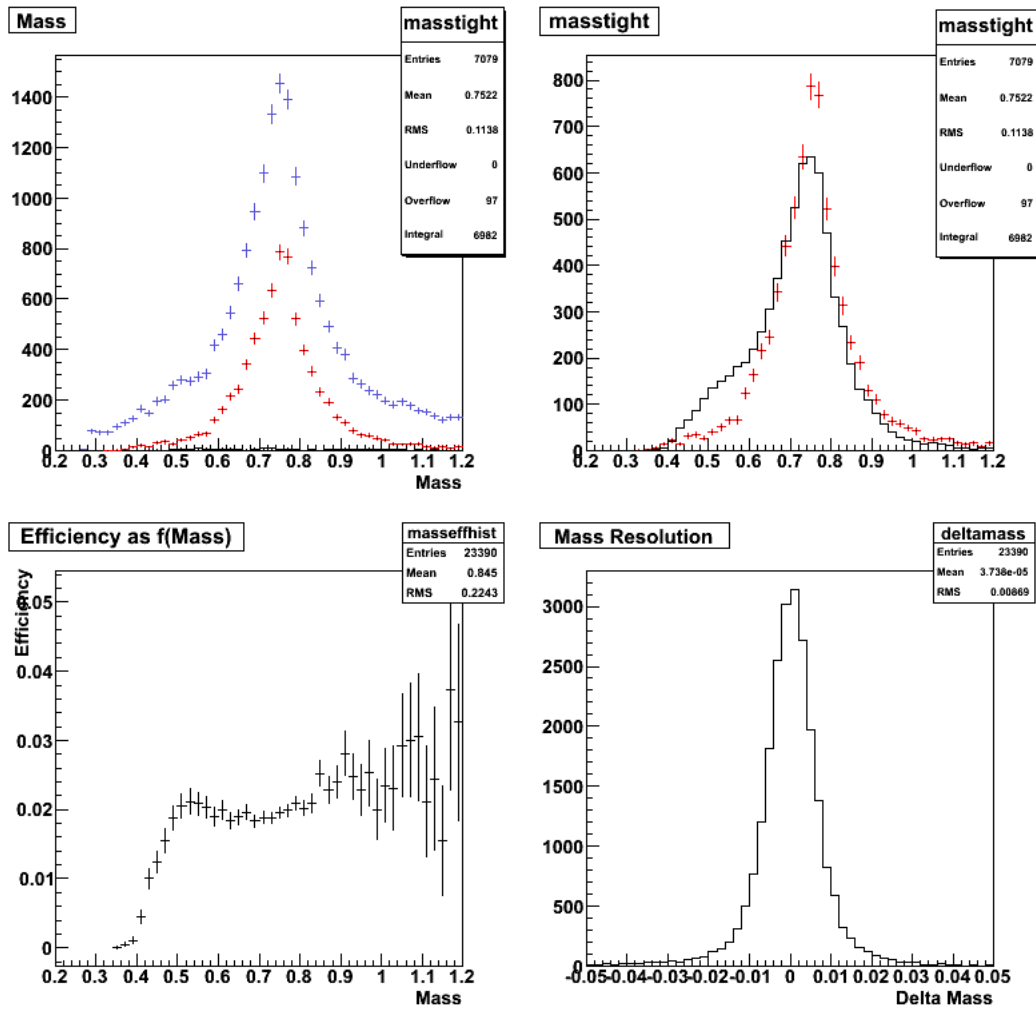


Figure C.6. The upper left histogram compares the data with loose cuts (top, blue), tight cuts (middle, red) and background (bottom black histogram at the zero level). A peak is visible at $M_{\pi\pi} = M(K_s)$. This may be due to photoproduction of the ϕ , followed by $\phi \rightarrow K_s K_L$. Because the Q value of the ϕ decay is so low, most of the K_s still make the p_T cut; the K_L usually vanishes without decaying. The upper right plot compares the data and the Monte Carlo; except for the K_s , the agreement is excellent. The lower left plot shows the efficiency; for $M_{\pi\pi} > 550$ MeV/ c , the efficiency is flat. The last plot shows the $M_{\pi\pi}$ resolution of about 8.3 MeV. [73]

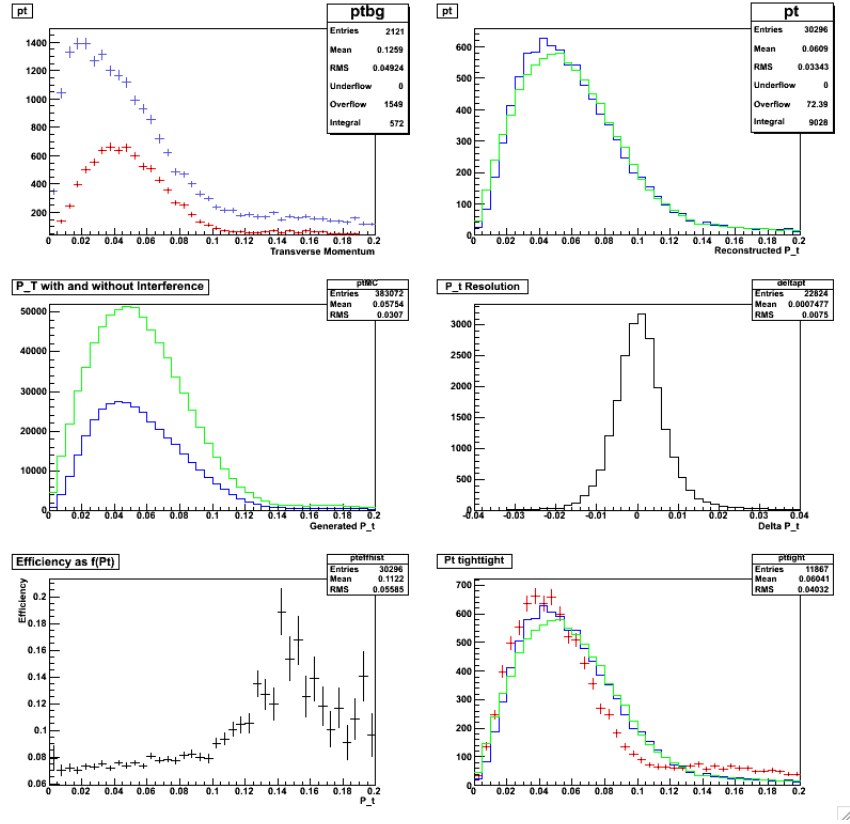


Figure C.7. The upper left histogram compares the p_T spectra with loose (blue) and tight (red) cuts. Events with $p_T > 120$ MeV/c appear consistent with incoherent ρ^0 production, $\gamma p \rightarrow \rho p$. The upper right plot compares the 'Int' (blue) and 'Noint' (green) p_T spectra, after simulation and reconstruction. The middle left histogram compares the 'Int' (blue) and 'Noint' (green) p_T spectra directly from STARlight, with no detector effects. The middle right histogram shows the p_T resolution is centered at 0, with $\sigma = 7.5$ MeV. The lower left histogram shows that the reconstruction efficiency is independent of p_T , except for the lowest bin, which is somewhat higher. This is probably due to p_T smearing. With the 'Int' spectrum (used here, since it matches the data better), the first bin has many fewer events than the next bin, so that there is smearing from bin 2 \rightarrow bin 1, but very little in the other direction. The lower right plot compares the p_T spectra of data (red), 'Int' (blue) and 'Noint' (green). [73]

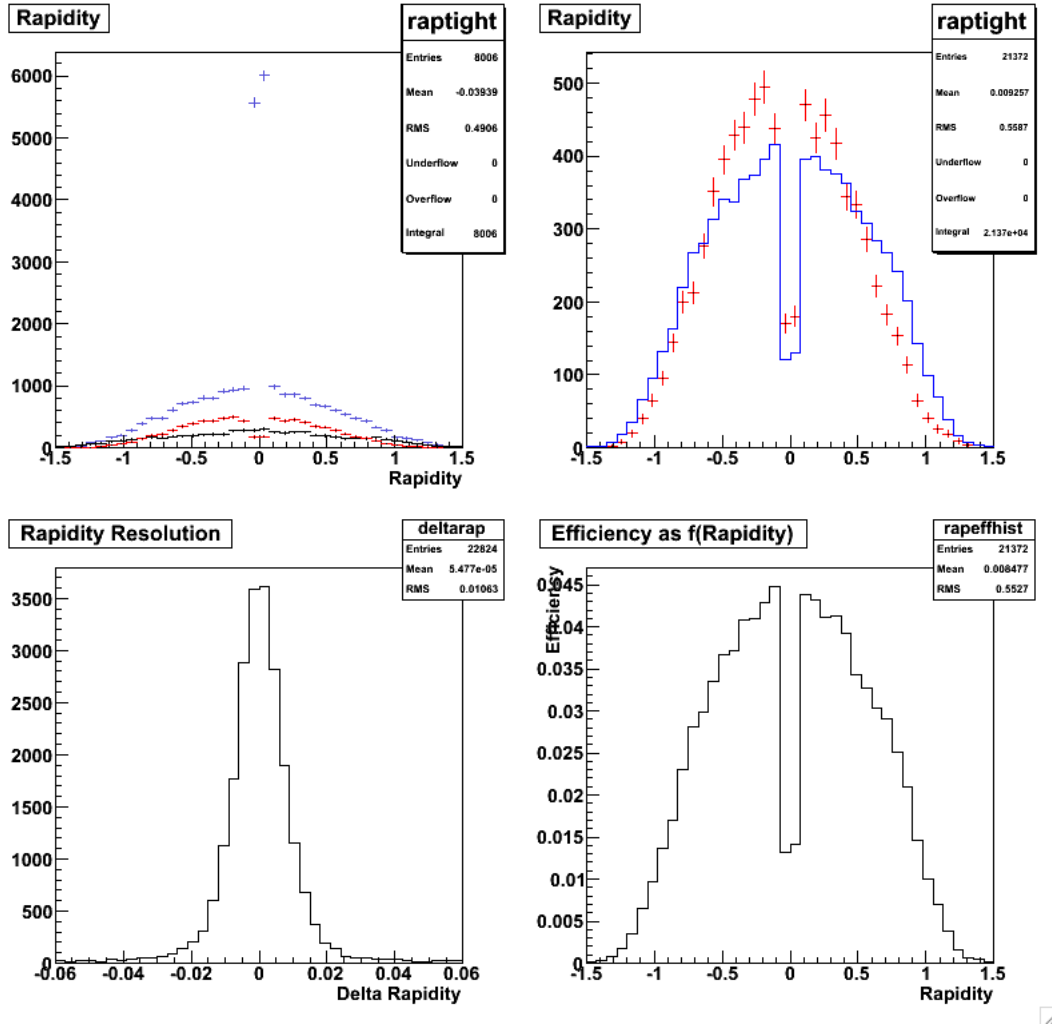


Figure C.8. The upper left histogram compares the data with loose cuts (blue), tight cuts (red), and background (with loose cuts). The loose cut plot shows an enhancement for $|y| < 0.1$. This is likely due to cosmic rays, which are reconstructed as pairs with $y = 0$, $p_T = 0$. The upper right histogram compares the data (red) and Monte Carlo (blue), while the lower left histogram shows the rapidity resolution, 0.01. This is very adequate for the analysis. The lower right histogram shows the efficiency as a function of rapidity. It is not flat, since the probability of a daughter pion being outside the TPC acceptance rises as rapidity rises, but since the data and MC agree well, this is no cause for concern. [73]

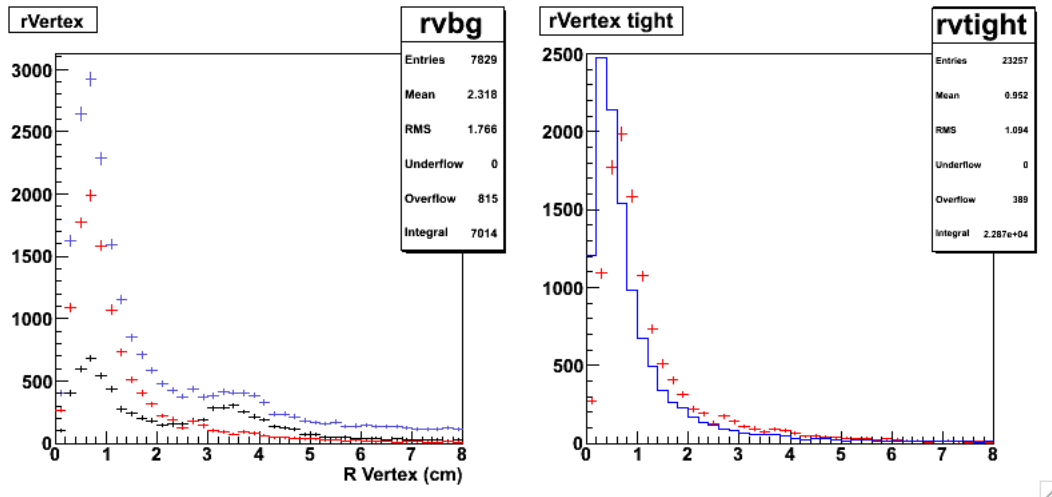


Figure C.9. The left plot shows the data with loose cuts (blue), tight cuts (red), and the background (black). With the loose cuts, a small rise is visible at $R \sim 3\text{cm}$. This disappears once tighter cuts are imposed. The background rate is so high here because there is no cut on z . The plot on the right compares the data (red) and the Monte Carlo (blue). The agreement is good. [73]

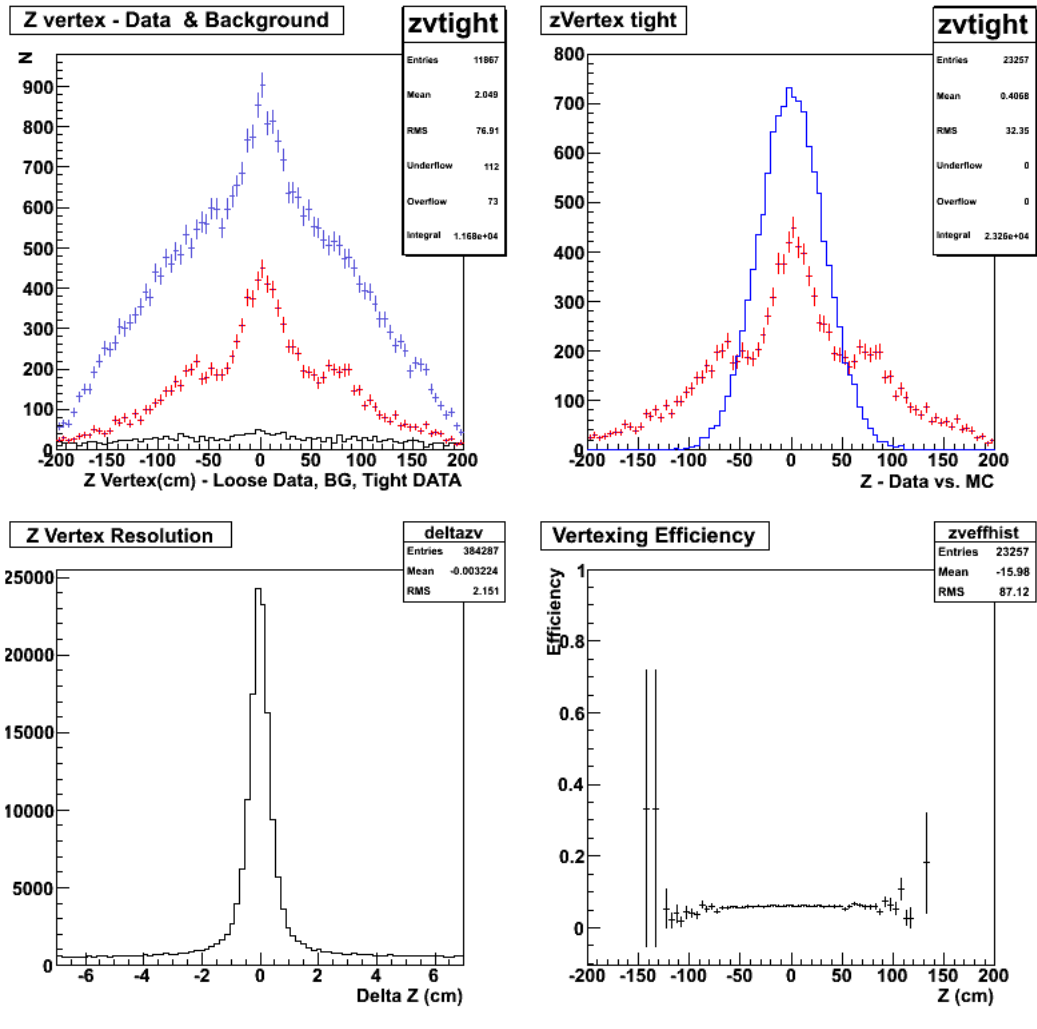


Figure C.10. The upper left histogram compares the data with loose cuts (blue) and tight cuts (red), and the background (black). The upper right histogram compares the (red) data and Monte Carlo (blue). The lower right is the resolution estimated with the Monte Carlo ($zVertex - zMC$); the resolution is 2 cm. The lower left shows the efficiency as a function of $zVertex$. It is approximately flat within the ± 50 cm cut range. [73]

Appendix D

Multi-Hadron $\Delta\phi$ Distributions

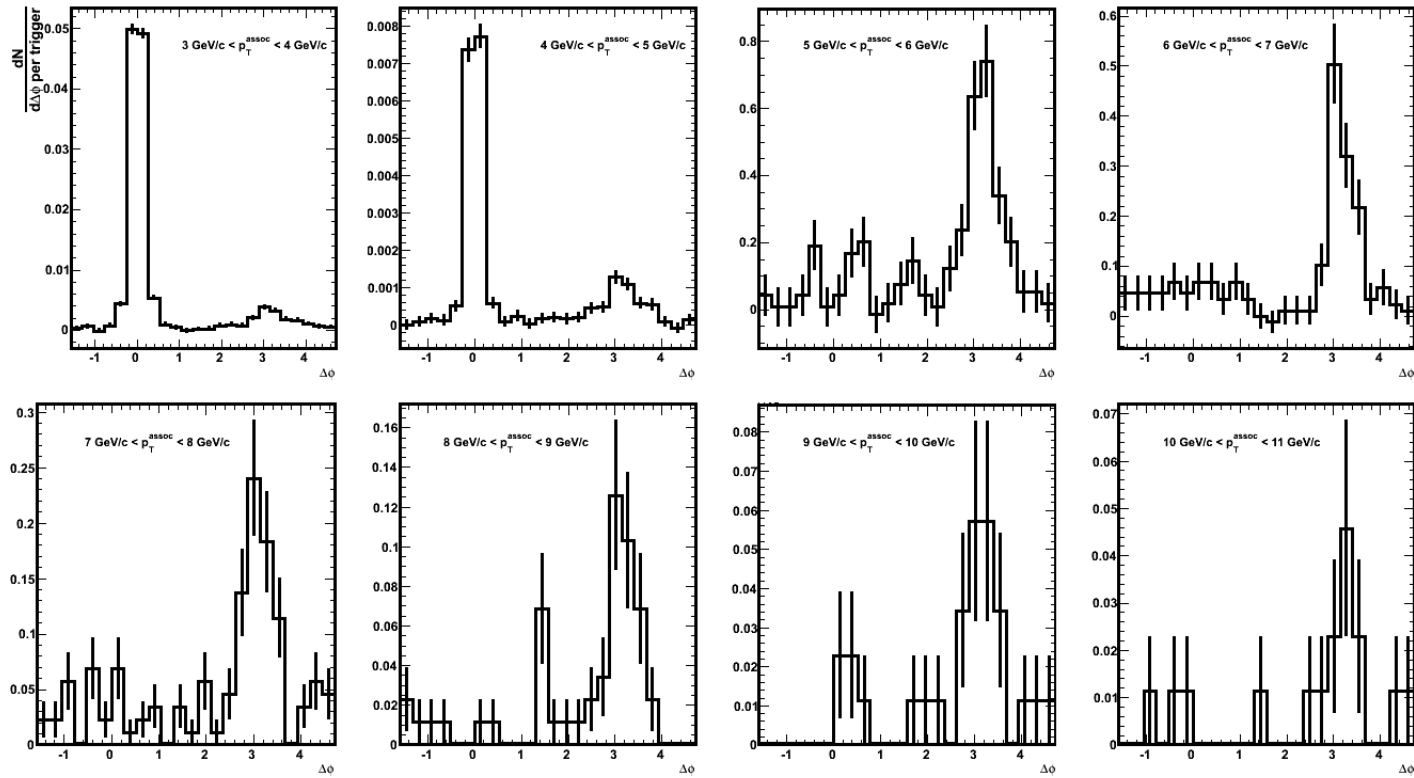


Figure D.1. Background subtracted azimuthal distributions per trigger for multi-hadron triggers with a minimum secondary seed of $2.0 \text{ GeV}/c$ for $8 < p_T^{trig} < 10 \text{ GeV}/c$ and successive slices of p_T^{assoc} as indicated on the plots.

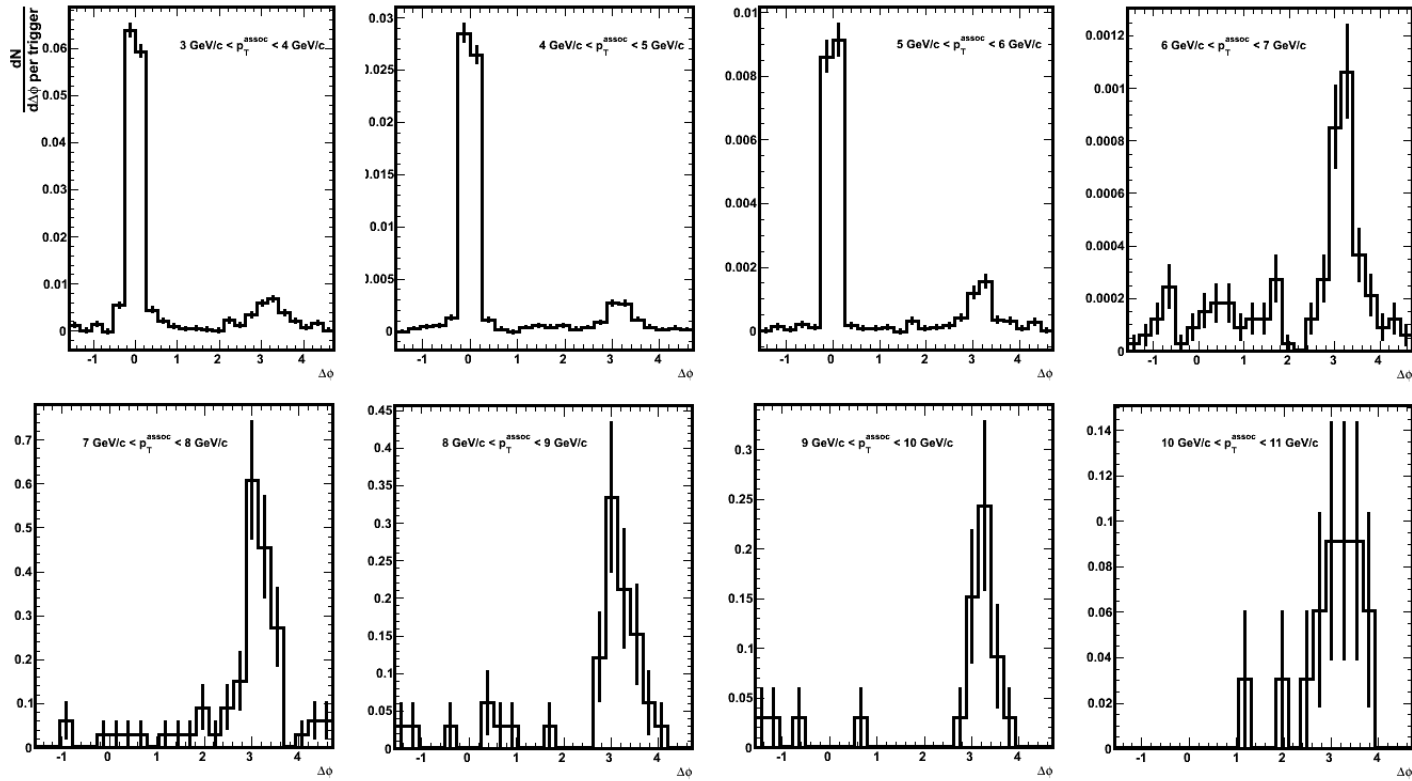


Figure D.2. Background subtracted azimuthal distributions per trigger for multi-hadron triggers with a minimum secondary seed of $2.0 \text{ GeV}/c$ for $10 < p_T^{trig} < 12 \text{ GeV}/c$ and successive slices of p_T^{assoc} as indicated on the plots.

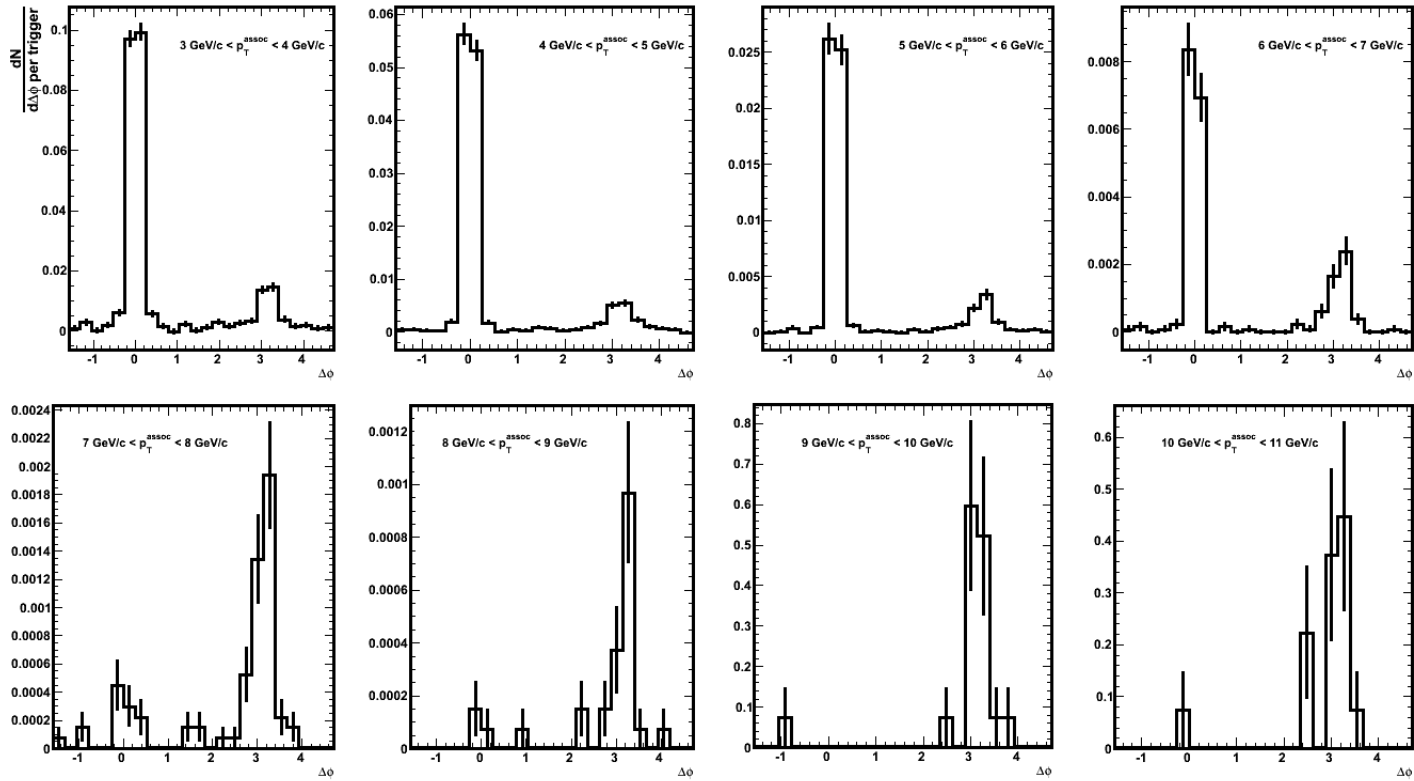


Figure D.3. Background subtracted azimuthal distributions per trigger for multi-hadron triggers with a minimum secondary seed of $2.0 \text{ GeV}/c$ for $12 < p_T^{trig} < 15 \text{ GeV}/c$ and successive slices of p_T^{assoc} as indicated on the plots.

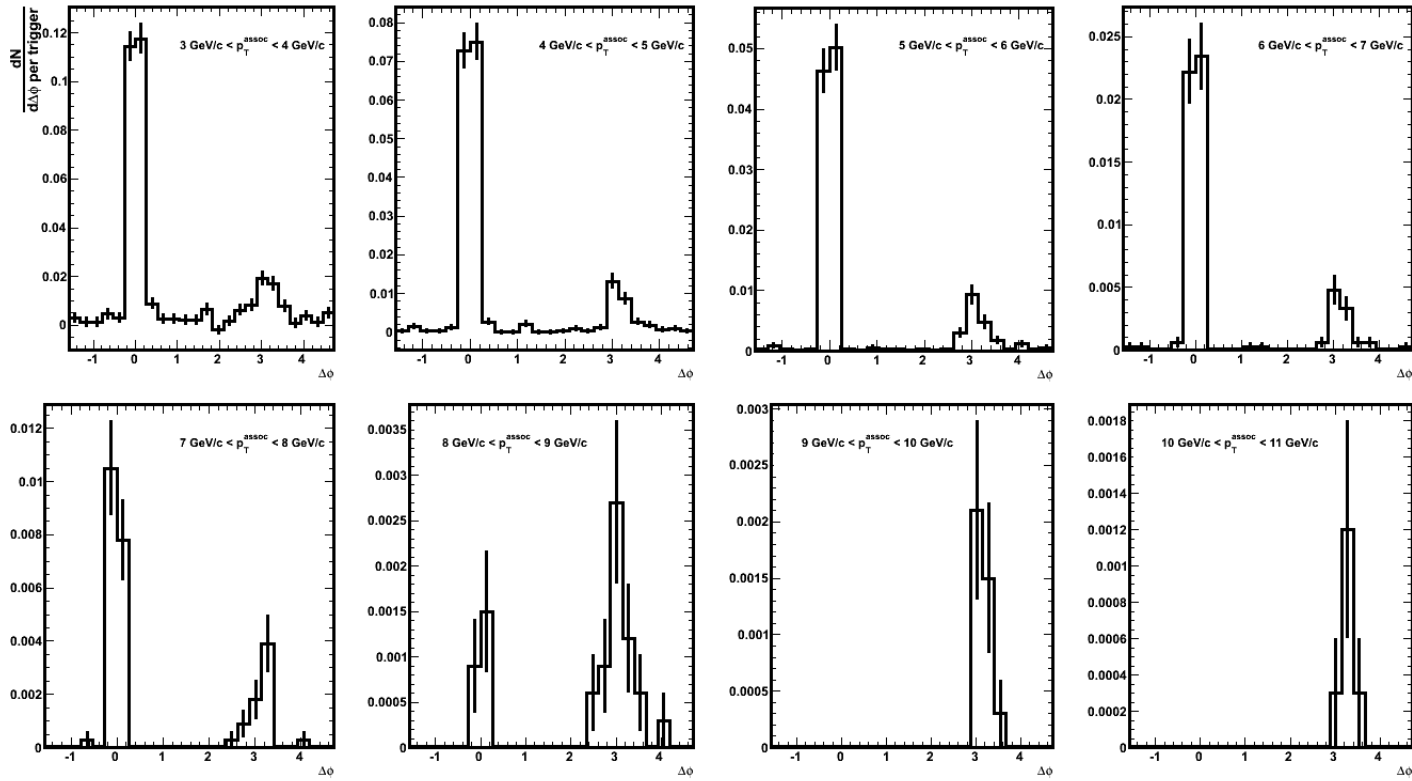


Figure D.4. Background subtracted azimuthal distributions per trigger for multi-hadron triggers with a minimum secondary seed of $2.0 \text{ GeV}/c$ for $15 < p_T^{trig} < 18 \text{ GeV}/c$ and successive slices of p_T^{assoc} as indicated on the plots.

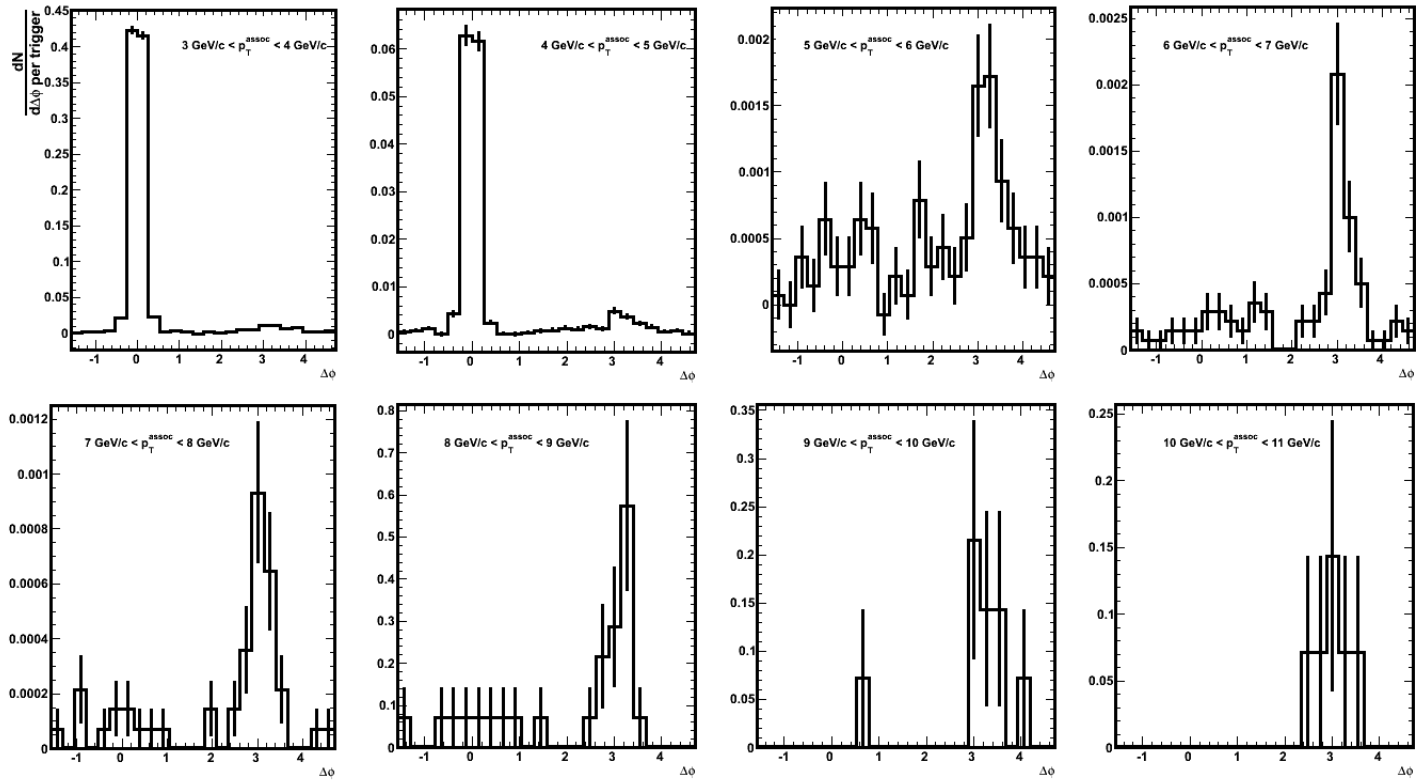


Figure D.5. Background subtracted azimuthal distributions per trigger for multi-hadron triggers with a minimum secondary seed of 3.0 GeV/c for $8 < p_T^{trig} < 10$ GeV/c and successive slices of p_T^{assoc} as indicated on the plots.

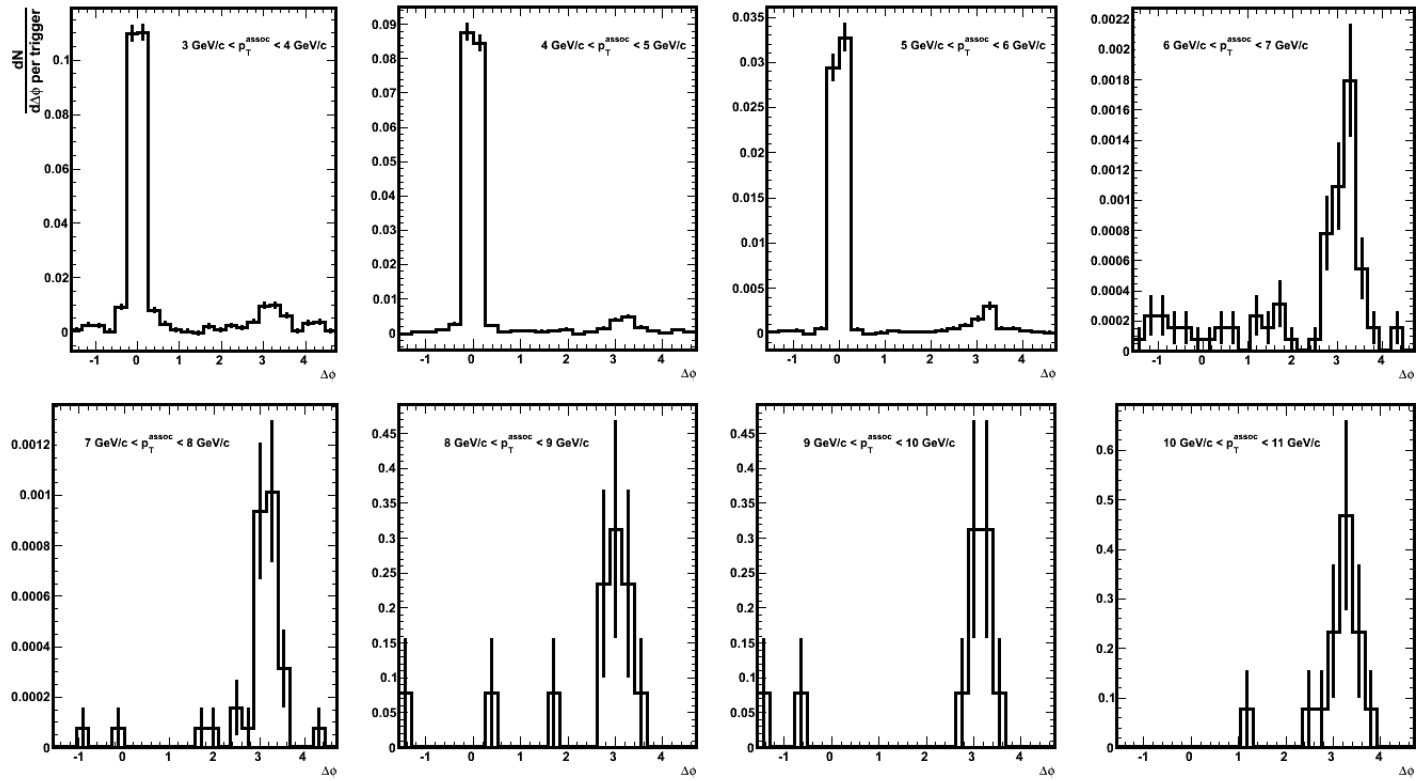


Figure D.6. Background subtracted azimuthal distributions per trigger for multi-hadron triggers with a minimum secondary seed of $3.0 \text{ GeV}/c$ for $10 < p_T^{trig} < 12 \text{ GeV}/c$ and successive slices of p_T^{assoc} as indicated on the plots.

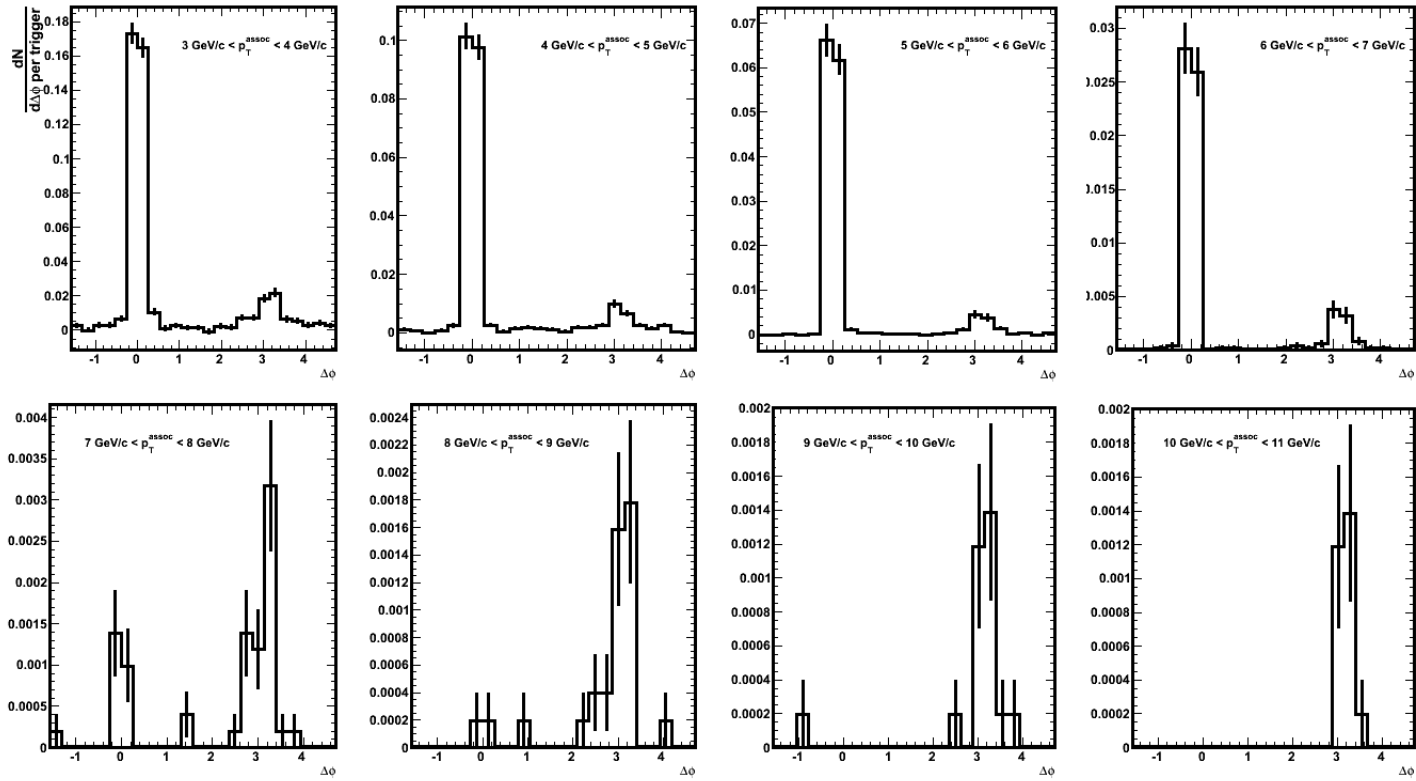


Figure D.7. Background subtracted azimuthal distributions per trigger for multi-hadron triggers with a minimum secondary seed of $3.0 \text{ GeV}/c$ for $12 < p_T^{trig} < 15 \text{ GeV}/c$ and successive slices of p_T^{assoc} as indicated on the plots.

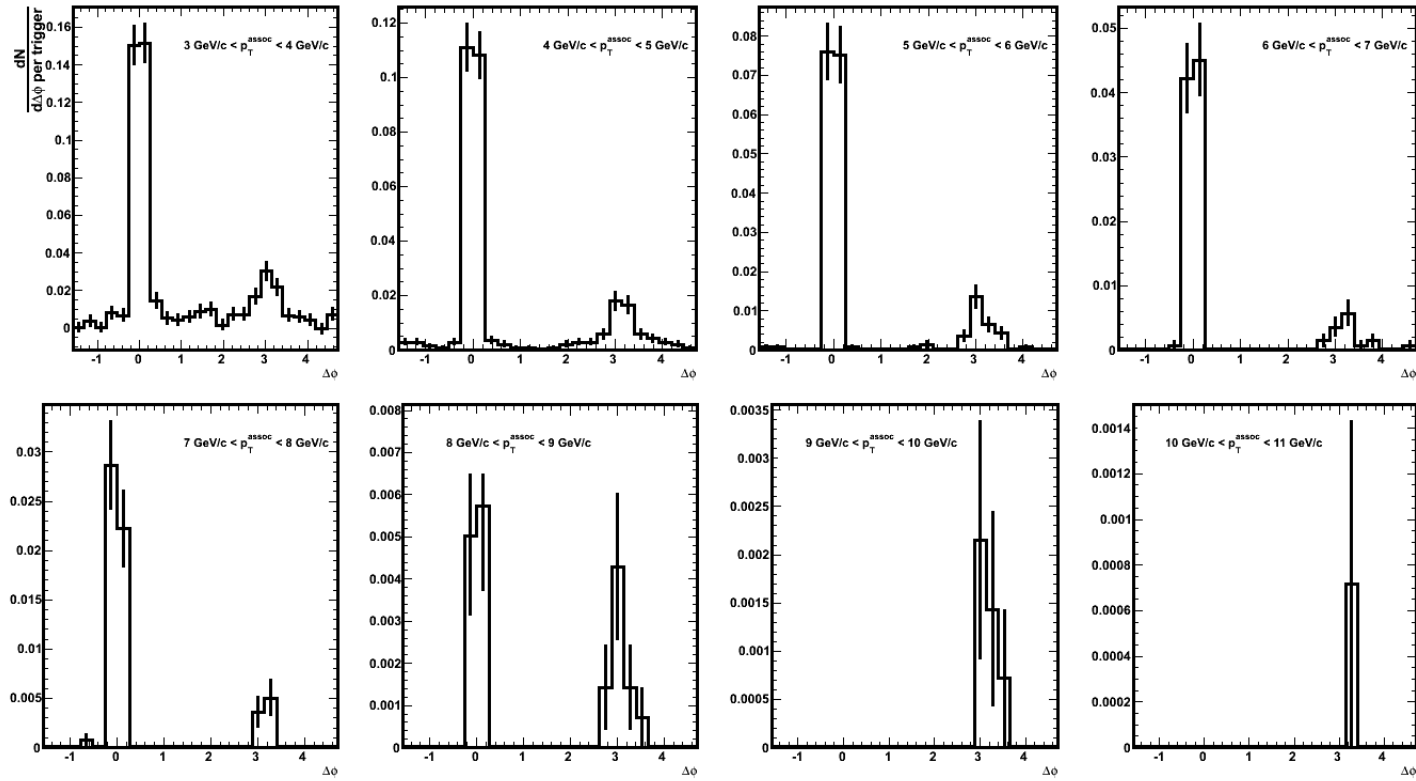


Figure D.8. Background subtracted azimuthal distributions per trigger for multi-hadron triggers with a minimum secondary seed of 3.0 GeV/c for $15 < p_T^{trig} < 18$ GeV/c and successive slices of p_T^{assoc} as indicated on the plots.

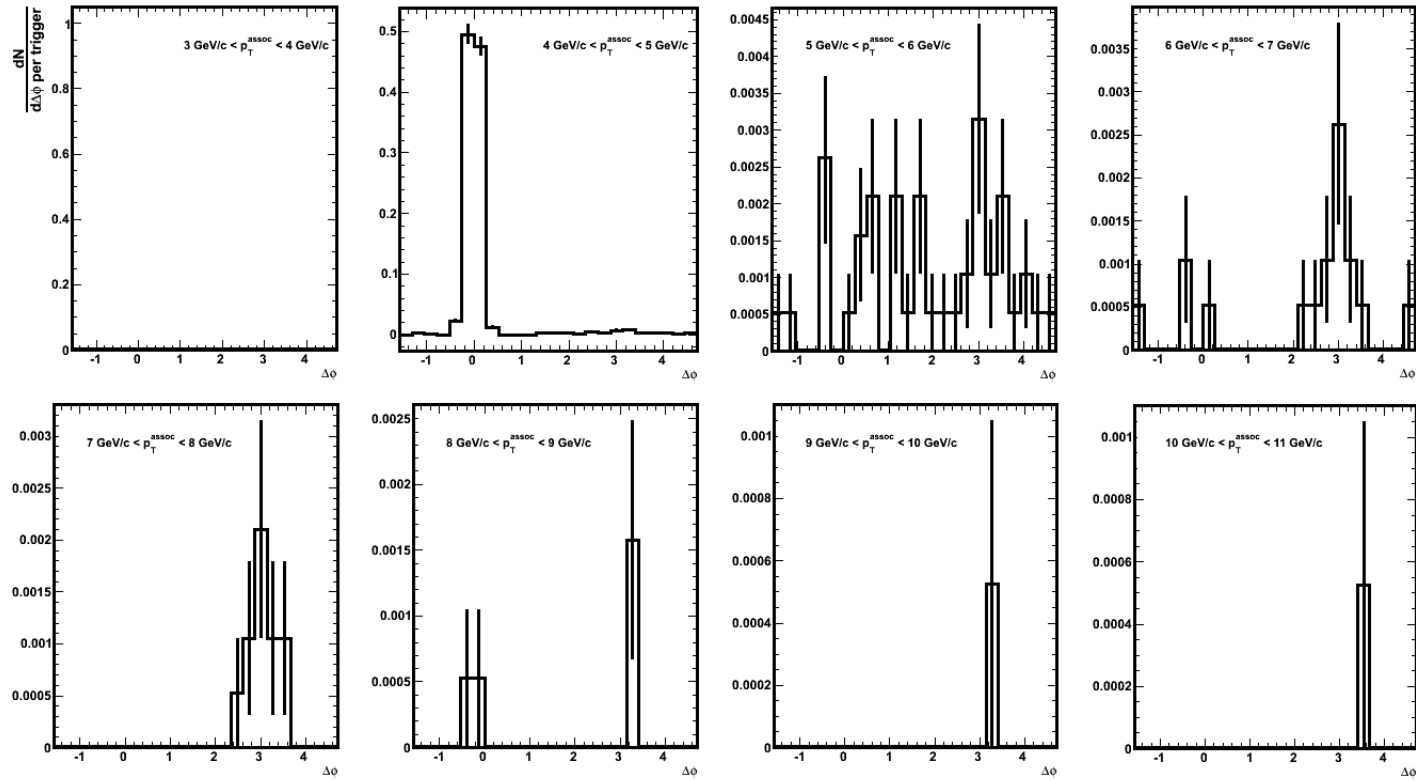


Figure D.9. Background subtracted azimuthal distributions per trigger for multi-hadron triggers with a minimum secondary seed of $4.0 \text{ GeV}/c$ for $8 < p_T^{trig} < 10 \text{ GeV}/c$ and successive slices of p_T^{assoc} as indicated on the plots.

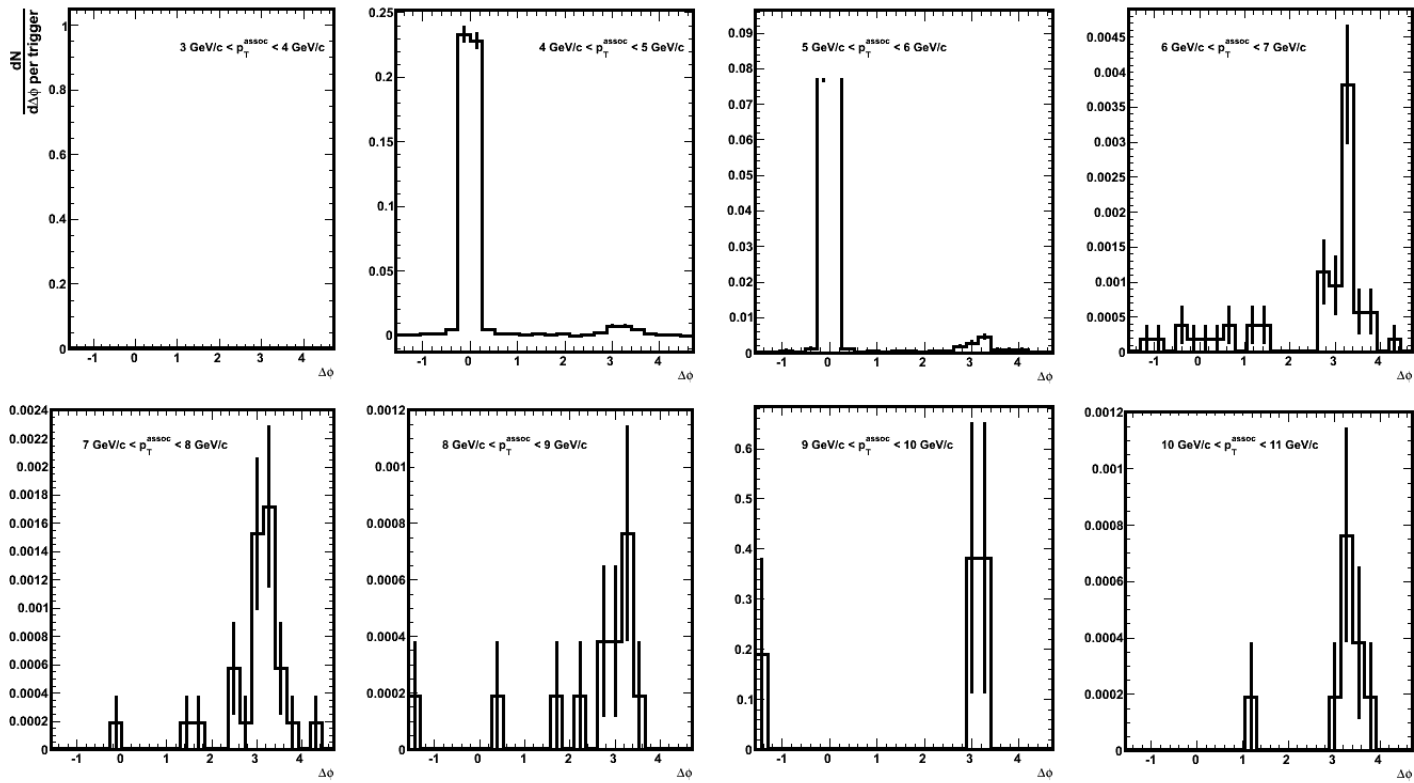


Figure D.10. Background subtracted azimuthal distributions per trigger for multi-hadron triggers with a minimum secondary seed of $4.0 \text{ GeV}/c$ for $10 < p_T^{trig} < 12 \text{ GeV}/c$ and successive slices of p_T^{assoc} as indicated on the plots.

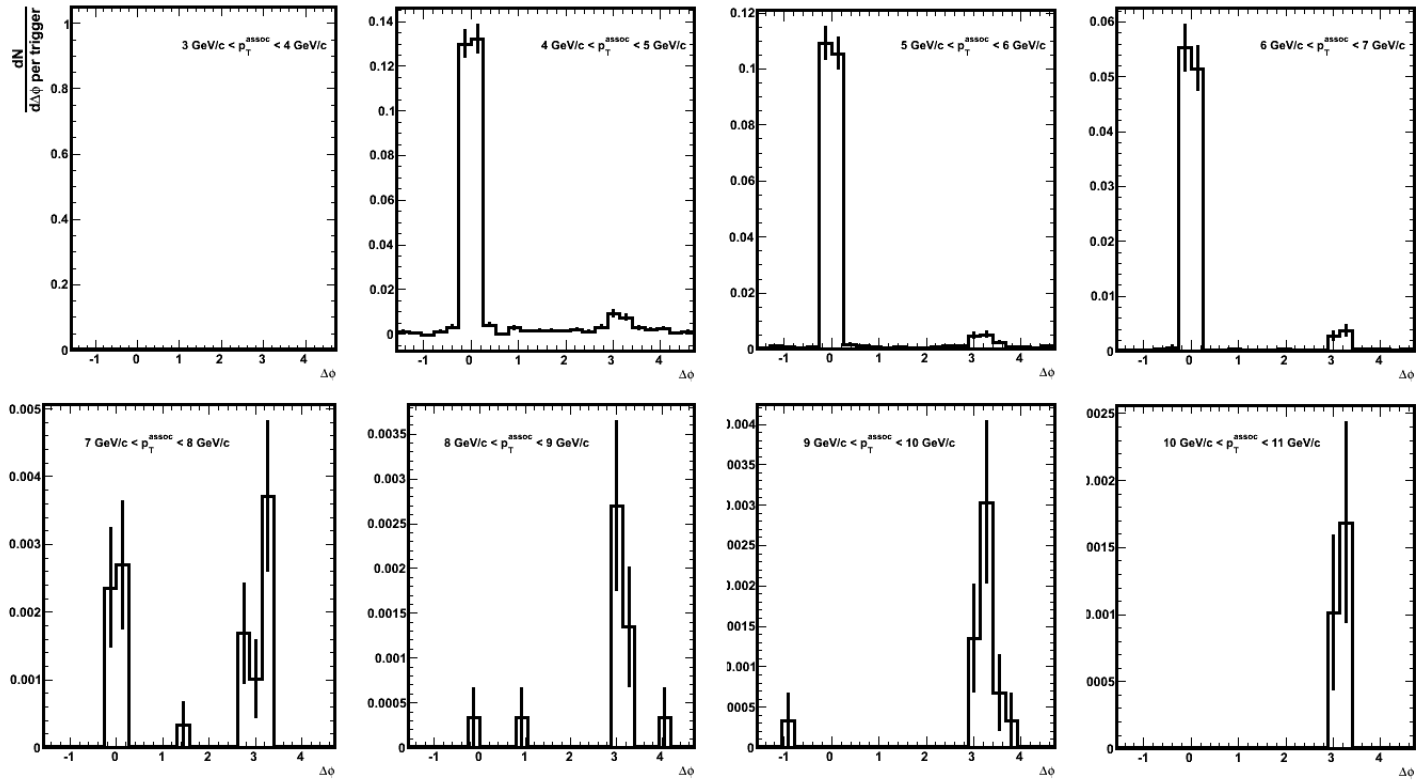


Figure D.11. Background subtracted azimuthal distributions per trigger for multi-hadron triggers with a minimum secondary seed of 4.0 GeV/ c for $12 < p_T^{trig} < 15$ GeV/ c and successive slices of p_T^{assoc} as indicated on the plots.

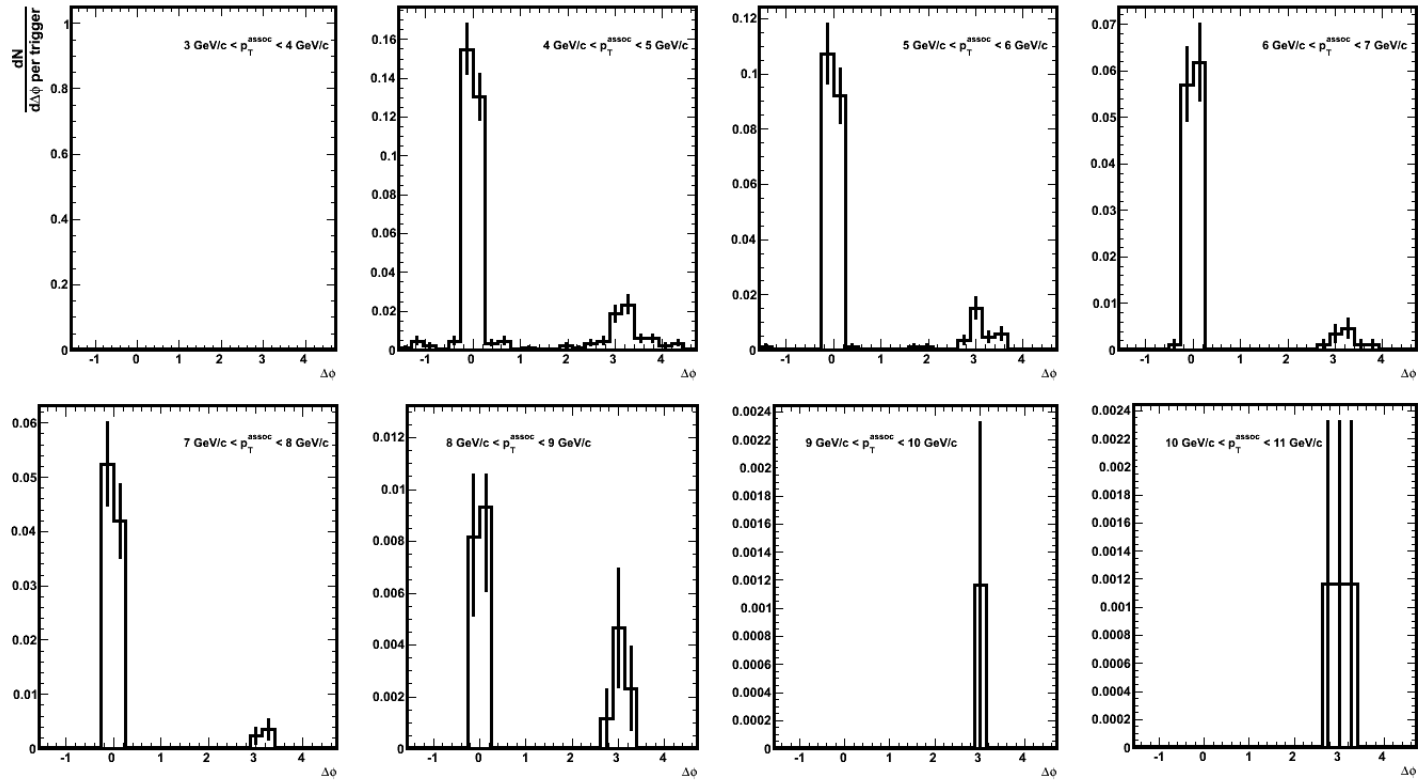


Figure D.12. Background subtracted azimuthal distributions per trigger for multi-hadron triggers with a minimum secondary seed of 4.0 GeV/c for $15 < p_T^{trig} < 18$ GeV/c and successive slices of p_T^{assoc} as indicated on the plots.

Bibliography

- [1] J. Adams *et al.* [STAR Collaboration], Nucl. Phys. A **757**, 102 (2005) [arXiv:nucl-ex/0501009].
- [2] R. Stock, J. Phys. G **30**, S633 (2004) [arXiv:nucl-ex/0405007].
- [3] M. A. Stephanov, PoS **LAT2006**, 024 (2006) [arXiv:hep-lat/0701002].
- [4] S. L. Blyth, *Using the ϕ -meson to probe the medium created in Au+Au collisions at RHIC*. PhD thesis, University of Cape Town, 2005.
- [5] K. J. Eskola and H. Honkanen, Nucl. Phys. A **713**, 167 (2003) [arXiv:hep-ph/0205048].
- [6] R. Picha, *Charged hadron distributions in 19.6-GeV Au+Au collisions*. PhD thesis, University of California, Davis, 2005.
- [7] M. J. Horner, *Systematic Studies of Low- and Intermediate- p_T Correlated Angular Distributions in Au+Au collisions at $\sqrt{s_{NN}} = 200$ GeV from the STAR Experiment*. PhD thesis, University of Capetown, 2005.
- [8] J. D. Bjorken, Phys. Rev. D **27**, 140 (1983).
- [9] B. B. Back *et al.*, Phys. Rev. Lett. **91**, 052303 (2003) [arXiv:nucl-ex/0210015].
- [10] S. S. Adler *et al.* [PHENIX Collaboration], Phys. Rev. C **71**, 034908 (2005) [Erratum-ibid. C **71**, 049901 (2005)] [arXiv:nucl-ex/0409015].
- [11] B. B. Back *et al.*, Nucl. Phys. A **757**, 28 (2005) [arXiv:nucl-ex/0410022].
- [12] O. Y. Barannikova [STAR Collaboration], arXiv:nucl-ex/0403014.
- [13] E. Schnedermann, J. Sollfrank and U. W. Heinz, Phys. Rev. C **48**, 2462 (1993) [arXiv:nucl-th/9307020].
- [14] X. N. Wang and M. Gyulassy, Phys. Rev. Lett. **68**, 1480 (1992).
- [15] M. Gyulassy and M. Plumer, Phys. Lett. B **243**, 432 (1990).
- [16] R. Baier, D. Schiff and B. G. Zakharov, Ann. Rev. Nucl. Part. Sci. **50**, 37 (2000) [arXiv:hep-ph/0002198].

- [17] A. Accardi, arXiv:hep-ph/0212148.
- [18] J. Adams *et al.* [STAR Collaboration], Phys. Rev. Lett. **91**, 172302 (2003) [arXiv:nucl-ex/0305015].
- [19] A. Accardi and M. Gyulassy, J. Phys. G **30**, S969 (2004) [arXiv:nucl-th/0402101].
- [20] S. S. Adler *et al.* [PHENIX Collaboration], Phys. Rev. C **69**, 034909 (2004) [arXiv:nucl-ex/0307022].
- [21] E. Yamamoto [STAR Collaboration], Nucl. Phys. A **715**, 466 (2003).
- [22] K. Schweda [STAR collaboration], J. Phys. G **30**, S693 (2004) [arXiv:nucl-ex/0403032].
- [23] J. Adams *et al.* [STAR Collaboration], Phys. Lett. B **612**, 181 (2005) [arXiv:nucl-ex/0406003].
- [24] P. Braun-Munzinger, I. Heppe and J. Stachel, Phys. Lett. B **465**, 15 (1999) [arXiv:nucl-th/9903010].
- [25] J. Sollfrank, J. Phys. G **23**, 1903 (1997) [arXiv:nucl-th/9707020].
- [26] J. Cleymans, B. Kampfer, M. Kaneta, S. Wheaton and N. Xu, Phys. Rev. C **71**, 054901 (2005) [arXiv:hep-ph/0409071].
- [27] B. Tomasik and U. A. Wiedemann, Phys. Rev. C **68**, 034905 (2003) [arXiv:nucl-th/0207074].
- [28] P. Braun-Munzinger, K. Redlich and J. Stachel, arXiv:nucl-th/0304013.
- [29] V. V. Ezhela, S. B. Lugovsky and O. V. Zenin, hep-ph/0312114.
- [30] F. Bergsma *et al.* [STAR Collaboration], Nucl. Instrum. Meth. **A499**, 633 (2003).
- [31] H. Wieman *et al.* [STAR Collaboration], IEEE Trans. Nucl. Sci. **44**, 671 (1997).
- [32] T. Zhao and L. He, IEEE Trans. Nucl. Sci. **43**, 1188 (1996).
- [33] M. Anderson *et al.*, Nucl. Instrum. Meth. A **499**, 659 (2003), [arXiv:nucl-ex/0301015].
- [34] M. Anderson *et al.*, Nucl. Instrum. Meth. A **499**, 679 (2003) [arXiv:nucl-ex/0205014].
- [35] D. Liko, STAR Note **00087** (1992) 1-15.
- [36] S. R. Klein and J. Nystrand, Phys. Rev. Lett. **84**, 2330 (2000) [arXiv:hep-ph/9909237].

- [37] S. Klein and J. Nystrand, Phys. Rev. C **60**, 014903 (1999) [arXiv:hep-ph/9902259].
- [38] S. Klein and E. Scannapieco, "Two-Photon Physics with STAR," *Star Note* **00243** (1996) 1-28.
- [39] H. Alvensleben *et al.*, Phys. Rev. Lett. **24**, 786 (1970).
- [40] W. M. Yao *et al.* (Particle Data Group) J. Phys. G. **33**, 1 (2006)
- [41] H. Alvensleben *et al.*, Phys. Rev. Lett. **24**, 792 (1970).
- [42] S. R. Klein [STAR Collaboration], arXiv:nucl-ex/0402007.
- [43] G. McClellan, N. B. Mistry, P. Mostek, H. Ogren, A. Silverman, J. Swartz and R. Talman, Phys. Rev. D **4**, 2683 (1971).
- [44] F. Bulos *et al.*, Phys. Rev. Lett. **22**, 490 (1969).
- [45] B. I. Abelev *et al.* [STAR Collaboration], Phys. Rev. C **77**, 34910 (2008) [arXiv:0712.3320 [nucl-ex]].
- [46] C. Adler *et al.* [STAR Collaboration], Phys. Rev. Lett. **89**, 272302 (2002) [arXiv:nucl-ex/0206004].
- [47] D. G. d'Enterria, arXiv:nucl-ex/0601001.
- [48] <https://www.racf.bnl.gov/about/>. RACF Computing Facility.
- [49] F. S. Bieser *et al.*, Nucl. Instrum. Meth. A **499**, 766 (2003).
- [50] E. Witten, Nucl. Phys. B **120**, 189 (1977).
- [51] R. Vogt, *Amsterdam, Netherlands: Elsevier (2007) 477 p.*
- [52] J. R. Forshaw and D. A. Ross, Cambridge Lect. Notes Phys. **9**, 1 (1997).
- [53] C. Y. Wong, *Singapore, Singapore: World Scientific (1994) 516 p.*
- [54] F. Abe *et al.* [CDF Collaboration], Phys. Rev. D **48**, 998 (1993).
- [55] I. Arsene *et al.* [BRAHMS Collaboration], Nucl. Phys. A **757**, 1 (2005) [arXiv:nucl-ex/0410020].
- [56] X. N. Wang, Phys. Rept. **280**, 287 (1997) [arXiv:hep-ph/9605214].
- [57] X. N. Wang and M. Gyulassy, Phys. Rev. Lett. **68**, 1480 (1992).
- [58] X. N. Wang, Z. Huang and I. Sarcevic, Phys. Rev. Lett. **77**, 231 (1996) [arXiv:hep-ph/9605213].

- [59] K. Adcox *et al.* [PHENIX Collaboration], Nucl. Phys. A **757**, 184 (2005) [arXiv:nucl-ex/0410003].
- [60] C. Adler *et al.* [STAR Collaboration], Phys. Rev. Lett. **90**, 082302 (2003) [arXiv:nucl-ex/0210033].
- [61] S. D. Ellis, J. Huston and M. Tonnesmann, in *Proc. of the APS/DPF/DPB Summer Study on the Future of Particle Physics (Snowmass 2001)* ed. N. Graf, *In the Proceedings of APS / DPF / DPB Summer Study on the Future of Particle Physics (Snowmass 2001), Snowmass, Colorado, 30 Jun - 21 Jul 2001, pp P513* [arXiv:hep-ph/0111434].
- [62] S. D. Ellis and D. E. Soper, Phys. Rev. D **48**, 3160 (1993) [arXiv:hep-ph/9305266].
- [63] J. Adams *et al.* [STAR Collaboration], Phys. Rev. Lett. **91**, 072304 (2003) [arXiv:nucl-ex/0306024].
- [64] S. S. Adler *et al.* [PHENIX Collaboration], Phys. Rev. Lett. **91**, 072303 (2003) [arXiv:nucl-ex/0306021].
- [65] I. Arsene *et al.* [BRAHMS Collaboration], Phys. Rev. Lett. **91**, 072305 (2003) [arXiv:nucl-ex/0307003].
- [66] B. B. Back *et al.* [PHOBOS Collaboration], Phys. Rev. Lett. **91**, 072302 (2003) [arXiv:nucl-ex/0306025].
- [67] N. N. Ajitanand *et al.*, Phys. Rev. C **72**, 011902 (2005) [arXiv:nucl-ex/0501025].
- [68] B. I. Abelev, arXiv:0812.1063 [nucl-ex].
- [69] L. Frankfurt, M. Strikman and M. Zhalov, Phys. Rev. C **67**, 034901 (2003) [arXiv:hep-ph/0210303].
- [70] L. Frankfurt, M. Strikman and M. Zhalov, Phys. Lett. B **537**, 51 (2002) [arXiv:hep-ph/0204175].
- [71] R. Brun, R. Hagelberg, M. Hansroul and J. C. Lassalle,
- [72] A. Einstein, B. Podolsky and N. Rosen, Phys. Rev. **47**, 777 (1935).
- [73] S. R. Klein, “Interference in rho production”, <http://www.star.bnl.gov/protected/pcoll/spencer/interfere/backup/backup.html>, 2001, (4 Mar 2008).
- [74] R. J. Glauber, *Lectures on Theoretical Physics* (Inter-Science, New York, 1959) Vol. I.

Acknowledgements

To Dr. Jesse Cude, who first guided me into realizing that I was a physicist at heart. Thank you for the inspiration. You have left me some tremendous shoes to fill.

Much gratitude goes to Daniel Cebra for the opportunity to join the UC Davis nuclear group and work on the STAR experiment. You have shown me what it is to really be a good physics professor and a scholar of life.

To Mike, many thanks for introducing me to the nuclear group and for dragging me kicking and screaming through my first year of graduate school. This thesis would not have happened without you.

Many thanks also to the nuclear group, for the support and camaraderie that only people who work shifts at Brookhaven understand.

Many thanks to the UPC group for all the valuable input and support, especially Yury Gorbunov for all his patience and valuable help.

To the RNC group at LBNL for welcoming me on all of my field trips out of Davis. I feel privileged to have had the opportunity to work with such world class scientists. Thanks especially to Marco and Joern for the multi-hadron study and the tremendous amount I learned in all our coffee break conversations. Thanks also to Mark and Sarah – I would not be finishing this thesis had it not been for you.

To Kelly, my second sister, you've been a tremendous support and source of understanding and empathy throughout this whole process. I look forward to all of our future adventures together.

Eric, you've seen me through the end of this whole thing. Thank you for the love, support, terrific meals, and unconditional understanding of all the late working nights.

Finally to my family, your support from the very first day I declared I was going to be a physics major is what got me through all the years of grueling study. Thanks to my father for always inspiring me to believe I could achieve great things. Thanks to my sister for your truly unconditional support, love, and confidence in me. Thanks to my mother for making me who I am.